Estimation of the Evaporation Rate of an Isolated Water Microdroplet Subjected to Infrared Radiative Heating

by

Luis Augusto Ferraz Albani

A thesis submitted in partial fulfillment of the requirements for the degree of

Master of Science

Department of Mechanical Engineering
University of Alberta

Abstract

A combined numerical-experimental investigation was performed to study the influence of infrared radiation on the evaporation of a single-component droplet in the range between 10 and 50 micrometers, under different environmental conditions of relative humidity and temperature of air. A numerical model that predicts the evolution of the droplet size with respect to time was developed under the assumptions of steady state evaporation, spherical symmetry, no relative velocity between the droplet and the surroundings, constant material properties, and no temperature gradient inside the droplet. Numerical simulations were generated to obtain plots of droplet diameter with respect to time for droplets with an initial diameter of 50 micrometers under four different conditions of relative humidity (*i.e.*, 0%, 30%, 60%, and 90%), two different air temperatures (*i.e.*, 20 °C and 60 °C), and various radiation intensities (*i.e.*, 0 $\frac{\mathrm{mW}}{\mathrm{mm}^2}$ to 10000 $\frac{\mathrm{mW}}{\mathrm{mm}^2}$). Experiments were performed using an opto-mechanical rig capable of generating a monodispersed vertical chain of droplets inside a glass flow tube with various conditions of relative humidity and air temperature, in which the size of the droplets was measured using shadowgraphy. The droplet images were collected and processed using a 12X microscopic optical system and commercial software, respectively. An infrared laser beam with a wavelength of 2.8 micrometers was generated and aligned with the vertical droplet chain in order to provide the system with high amounts of infrared radiation at a wavelength in which the liquid water has a high absorptivity. The experimental and numerical results showed good agreement in all cases. It was determined that at elevated magnitudes of incident infrared radiation the evaporation rate of water droplets increases substantially and high amount of vapor content in the surrounding air becomes inconsequential.

To Venezuela, my beloved homeland

Acknowledgements

I would like to express my sincerest gratitude to all the people that supported me through this fulfilling and exciting experience, especially to God, my beloved wife Jessica, and my dear parents, Luis and Gabriela. Thank you for all your love and patience during this challenging stage of my life.

I would also like to thank my supervisors, Dr. Jason Olfert and Dr. David Nobes for their endless support and valuable advice. Thank you for believing in me and giving me the opportunity to work under your guidance during my program, even in the most difficult times.

Special thanks to Dr. Larry Kostiuk, whose support and advice were essential for the completion of this work. I would also like to especially thank Dr. Reinhard Vehring for letting me work in his research facilities, and Dr. Wolfgang Jaeger and Chrissy Knapp for letting me use their specialized equipment for my research.

Finally, I would like to thank my friends and colleagues, Johana Gomez, David Barona, Martha Ramirez, Oskar Michalski, Alberto Baldelli (thank you for all the time and support in the laboratory), Hale Oguzlu, Ricardo Flores, Juan C. Rosas, Pierre Rosado, Miguel Balzan, Mohammed Boraey, Juliana Valencia, Hui Wang, Shichao Yue, Diana Martinez, Sara and Sebastian Barrera, and everybody else that were there. Thank you for being there and making these years more enjoyable.

Table of Contents

3 Experimental Set up 67

4 Results – Numerical 98

List of Tables

List of Figures

List of Symbols

a	Thermal diffusivity $\left[\frac{\mathrm{m}^2}{\mathrm{s}}\right]$
A	Area $[\mathrm{m}^2]$
A'	Advective coefficient of the ordinary differential equation system [m]
B	Coefficient of the ordinary differential equation system [K]
Bi	Biot Number
B_x	Bias error
c	Separation distance between droplets [m]
c_0	Speed of light in a vacuum $\left[\frac{\mathrm{m}}{s}\right]$
C	Cross-sectional area of the sphere $[\mathrm{m}^2]$
c_p	Specific heat capacity $\left[\frac{\mathrm{J}}{\mathrm{kg\ K}}\right]$
d	Droplet diameter $[\mathrm{m}]$
D	Mass diffusion coefficient $\left[\frac{\mathrm{m}^2}{\mathrm{s}}\right]$
D_H	Hydraulic diameter $[\mathrm{m}]$
$\dot{E}$	Total energy per unit time [W]
F	View factor

g	Acceleration of gravity $\left[\frac{\mathrm{m}}{\mathrm{s}^2}\right]$
h	Specific enthalpy $\left[\frac{\mathrm{J}}{\mathrm{kg}}\right]$
h_p	Planck's constant $\left[\frac{\mathrm{m}^2\mathrm{kg}}{\mathrm{s}}\right]$
h_{fg}	Latent heat of vaporization $\left[\frac{\mathrm{J}}{\mathrm{kg}}\right]$
$\dot{H}$	Total enthalpy per unit time [W]
I	Transmitted power [W]
I_o	Incident power [W]
j	Mass flux per unit area $\left[\frac{\mathrm{kg}}{\mathrm{m}^2\ \mathrm{s}}\right]$
k_{im}	Imaginary part of the refractive index
k_{B}	Boltzmann constant $\left[\frac{\mathrm{m}^2\mathrm{kg}}{\mathrm{s}^2\mathrm{K}}\right]$
L	Latent heat of vaporization $\left[\frac{\mathrm{J}}{\mathrm{kg}}\right]$
Le	Lewis Number
m	Complex index of refraction
$\dot{m}$	Mass flux $\left[\frac{\mathrm{kg}}{\mathrm{s}}\right]$
n_{re}	Real part of the refractive index
n_s	Number of samples
n	Number of data points
N	Normal distribution function

p	Fresnel relations constant
P	Pressure $[\mathrm{Pa}]$
P_x	Precision error
Pe_{M}	Mass Peclet number
Pe_{T}	Thermal Peclet number
Pr	Prandtl number
q	Fresnel relations constant
Q	Efficiency factor
$\dot{Q}$	Heat per unit time $[\mathrm{W}]$
$\dot{Q}''$	Heat per unit time per unit area $\left[\frac{\mathrm{W}}{\mathrm{m}^2}\right]$
r	Droplet radius $[\mathrm{m}]$
$\hat{r}$	Radial spherical coordinate
Re	Reynolds number
R_{mix}	Specific gas constant for a mixture $\left[\frac{\mathrm{J}}{\mathrm{kg\ K}}\right]$
R	Universal gas constant $\left[\frac{\mathrm{J}}{\mathrm{kmol\ K}}\right]$
s	Penetration distance [cm]
S	Travelling distance [m]
S_{xy}	Standard error of estimate
Sc	Schmidt number
Sh	Sherwood number

t	Time [s]
T	Temperature [K, °C]
U_x	Total uncertainty
v	Velocity $\left[\frac{\mathrm{m}}{\mathrm{s}}\right]$
W	Molecular mass $\left[\frac{\mathrm{kg}}{\mathrm{kmol}}\right]$
$\bar{W}$	Molecular mass of the gas-vapor mixture $\left[\frac{\mathrm{kg}}{\mathrm{kmol}}\right]$
$\dot{W}$	Work per unit time [W]
$\dot{W}''$	Power per unit area $\left[\frac{\mathrm{W}}{\mathrm{m}^2}\right]$
x	Particle size parameter
Y	Mass fraction $\left[\frac{\mathrm{kg\ of\ k{-}species}}{\mathrm{kg\ of\ mixture}}\right]$
$z_{c/2}$	Z-factor for a confidence interval of *c*%

Greek Letters

α	Absorptivity
β	Extinction coefficient
δ	Reflectivity
ε	Emissivity
η	Wavelength [m]

μ	Viscosity $\left[\frac{\mathrm{kg}}{\mathrm{m\ s}}\right]$
θ	Incidence angle [rad]
$\hat{\theta}$	Azimuthal spherical coordinate
κ	Absorption coefficient $\left[\frac{1}{\mathrm{cm}}\right]$
λ	Thermal conductivity $\left[\frac{\mathrm{W}}{\mathrm{m\ K}}\right]$
ρ	Density $\left[\frac{\mathrm{kg}}{\mathrm{m}^3}\right]$
γ	Surface tension $\left[\frac{\mathrm{N}}{\mathrm{m}}\right]$
σ	Scattering coefficient
σ_d	Standard deviation
σ_{SB}	Stefan-Boltzmann constant $\left[\frac{\mathrm{W}}{\mathrm{m}^2\ \mathrm{K}^4}\right]$
τ	Transmissivity
ϕ	Concentration $\left[\frac{\mathrm{kg}}{\mathrm{m}^3}\right]$
$\hat{\varphi}$	Polar spherical coordinate

Subscripts

air	Air
abs	Absorption
b	Blackbody

cond	Conduction
d	Droplet
e	External
ext	Extinction
f	Fluid
g	Gas
heat	Heat
i	Internal
in	Inwards
out	Outwards
k	Species k
liq	Liquid
mass	Mass
mix	Mixture
rad	Radiative, Radiation
r	Radial
s	Surface
sat	Saturation
sca	Scattering
ter	Terminal

tot	Total
vap	Vapor
0	Initial
θ	Azimuthal
φ	Polar
η	Spectral
∞	Infinity

Abbreviations

RH	Relative humidity
FOV	Field of view
IR	Infrared
ID	Inner diameter
OD	Outer diameter
CV	Control volume
ODE	Ordinary differential equation
FWHM	Full width half maximum
OPO	Optical parametric oscillator
PPLN	Periodically-poled Lithium Niobate

CW	Continuous wave
EDB	Electro-dynamic balance
CCD	Charge-coupled device
LED	Light-emitting diode

Chapter 1

Introduction

1.1 Background and Motivation

The evaporation of small liquid droplets is a process of wide interest in modern society. This phenomenon plays a fundamental role in multiple applications, including: pharmaceutical engineering, combustion of atomized fuels, fire suppression mechanisms, industrial evaporative cooling processes, food conservation, and atmospheric sciences. Although the use of the word "small" in the present work may appear vague, it refers to droplets with diameters in the order of 1 µm to 100 µm. This size range is present in a large number of pharmaceutical, spray drying, combustion and environmental applications.

In the pharmaceutical area, one of the applications where the evaporation of droplets is present is the formation of powders that are initially a liquid solution (aqueous and non-aqueous) via spray drying. This process can also be found in the food industry, for example, in the production of powdered milk. Knowing the rate of evaporation is important in these applications since it will affect the quantity and the morphology of the produced particles. A complete review of the recent technical developments and the theoretical framework in particle formation via spray drying was shown by Vehring (2007).

Evaporation is also present in other applications such as the combustion of atomized fuel droplets in internal combustion engines, furnaces and turbines' combustion chambers. In these processes, the fuel droplets are supplied into the system in liquid form but need to change to vapor phase in order to burn. The evaporation rate of fuel droplets is important in this application since it affects the rate of combustion, hence, the power or amount of heat produced. For this case, several models have been developed to describe the dynamics of droplet heating and evaporation to account for different physical considerations. An exhaustive review of these models was made by Sirignano (1999), and more recently by Sazhin (2006).

The evaporation of liquid droplets is considered a coupled heat and mass transfer phenomenon (Vehring *et al*., 2007), in which the driving force is the difference of the vapor concentration of the droplet between its surface and the surroundings. In the case of water droplets in air, the variation of the environmental relative humidity affects the evaporation rate since it varies the water vapor concentration of the surrounding air. Under normal circumstances, droplets evaporating in spray drying and combustion applications are subjected to conductive and convective heat transfer due to the high temperatures of the surrounding gases. The effects of infrared (IR) radiation coming into the liquid phase of the droplet as an external energy source are usually neglected in spray drying applications due to its relative high complexity and the expected small energy contribution when compared with conduction and convection. Moreover, in some combustion processes, the radiation originated from the high temperatures of the flame surrounding the liquid droplet is often neglected when it is compared with the high rates of heat transport due to conduction from the hot gases if they are in very close proximity to the droplet. This assumption appears common in fuel spray combustion, but its validity is untested for the situation of an aqueous droplet being part of a gaseous fuel stream that is feeding a diffusion flame that is not in close proximity to droplets, *e.g.,* gas flaring devices.

Gas flaring is an industrial process present in petroleum and gas production sites (*e.g*., onshore and offshore rigs, as well as in refineries and chemical plants) that consists in burning large amounts of flammable gases that are associated with the extraction of crude oil. In the majority of cases, this process is done since the costs of transporting the associated gases are much higher than their market value, although there are other cases where the gases are vented and burned into the atmosphere to prevent excessive pressures on storage tanks that might represent a hazard to the environment and the workers of a production plant.

In gas flaring stacks, the presence of water and hydrocarbon droplets in the gas stream is possible due to two reasons: (a) the condensation of saturated water or hydrocarbon vapors, and, (b) the carry-over of water or other hydrocarbon droplets already formed in a previous process (Kostiuk *et al*., 2004). It was determined that the presence of these droplets in the gas stream affects the overall efficiency of the flame, which depends on three factors: the composition, quantity and individual size of the droplets (Kostiuk *et al*., 2004). An experimental investigation was done by these investigators in order to study the effects of these parameters on the efficiency of flames under different crosswind conditions. Distilled water, iso-octane and diesel droplets were used in the investigation. In the case of water droplets, it was observed that the combustion efficiency decreased proportionally to the amount of water added to the gas stream. Additionally, it was determined that the size of the droplets that fully evaporated before reaching the top of the stack depends on the size and luminosity of the flame (*e.g*., the intensity of the radiation), the travel time and the composition, however, no results were obtained with regards to the effect of the initial size of the droplets on the combustion efficiency since in all the cases the droplets evaporated before reaching the flame.

The investigation described above was successful in developing a model to study the effect of fuel and non-hydrocarbon droplets on overall flame efficiency, but little or nothing is known about the evolution of these droplets in the period between the entrance and the exit of the stack, specially under different conditions of gas temperature, relative humidity (often caused by the injection of steam in order to reduce the formation of black smoke) and radiation intensity.

The interest of the present investigation is to study the effects of infrared radiation as an independent means of increasing the rate of evaporation of single water droplets under various conditions of relative humidity and surrounding gas temperature. The effects of infrared radiation in the evaporation of sprays are not considered since: (a) it is easier to quantify the changes of individual droplets, and (b) it is necessary to understand well the simplest case prior to investigate a complex situation. Moreover, water will be considered only as a prototypical fluid on which the understanding of the phenomenon is performed, but the general concepts are applicable to a broad range of substances.

1.2 Droplet evaporation models and experimental studies including the effects of incident infrared radiation

A large number of theoretical models on droplet evaporation in different gas flow conditions have been developed in the last three decades and some examples can be found in the investigations carried by Dukowicz (1980), Kincaid & Longley (1989), Miller *et al*. (1998), and Sazhin (2005). Experimental studies, like the ones carried by Rosell-Llompart & Fernandez de La Mora (1994), Shekunov (2007), Vehring *et al*. (2007), and Maqua (2008); and theoretical studies, including the works by Mulholland *et al*. (1988), Vesala *et al*. (1989), and Frackowiak (2010) involve the use of monodisperse droplet chains of aqueous solutions and pure liquids in aerosols, spray drying, and combustion applications, and can also be found in the literature. These studies, however, do not include the effects of infrared radiation on the evaporation rate.

The use of monodisperse droplet chains to study the dynamics of droplet evaporation offers a good alternative to other known techniques (*e.g.*, levitating droplets, filament-suspended droplets). The monodisperse droplet chain technique consists in producing free falling droplets with a constant initial size inside a flow tube. This allows for several droplets to be generated and studied, whereas this can only be done once for a single droplet with the other techniques. It is believed that a free falling droplet technique can be safely used without accounting for significant errors (introduced by the difference between the gas and droplet velocities) for low sphere Reynolds numbers (*i.e.,* laminar flow).

The investigation of the influence of radiation into the evaporation of liquid droplets is not new. Several researchers, including Romanov & Pustovalov (1973), Strelkov (1974), Vdovin *et al*. (1975), Ermachenko & Rubezhnyi (1976), Pustovalov & Romanov (1977), and Yalamov *et al*. (1977), have theoretically studied the effects of radiation on droplet evaporation for a wide range of cases, including quasi-stationary, transient, convective and diffusional evaporation cases; however, given the difficulty of producing and studying isolated micron sized particles, these studies lacked of the experimental data needed for its validation.

Harpole (1980) developed a novel method to compute the evaporation time of water droplets with an initial diameter of 3 mm, and subjected to black body surroundings with a temperature range between 450 K and 1450 K in nuclear reactor cooling applications. In this model, the total absorption of the radiation by the spherical droplet was calculated numerically in the complete spectrum by considering the effects of polarization, refraction, reflection and multiple internal reflections. However, the author assumed that the temperature of the droplets remained constant at the boiling point of water (*i.e.*, 373 K). By doing this, the flux of vapor across the droplet surface was assumed to occur exclusively by the energy contributions of conductive and radiative heat into the droplet. The author also did not considered the diffusive evaporation due to the mass fraction difference between the surface of the droplet and the surrounding gas; hence, making the model inapplicable in the current area of interest of the present investigation.

Another example of the development of a numerical model that investigates the effect of infrared radiation on the evaporation of water micro droplets can be observed in the work of Young and Tomlinson (1993). A theoretical model was developed to simulate the evolution in size and temperature of a large volume of fog, composed of water droplets with radii in the range from 0.3 µm - 30 µm, and illuminated by a CO_2 laser (wavelength of 10.6 µm) with a hypothetical beam diameter of 1 m for the purpose of improving the visibility in commercial and military airports. Predicted results showed the influence of the initial fog temperature, the particle concentration (*i.e.*, amount of water droplets in the fog volume), the initial droplet size, the ambient pressure, and the laser power density on the total time of evaporation of the fog. It is of particular interest the fact that the evaporation time was reported to be virtually independent of the particle concentration. Although the results were not validated rigorously, some insight can be gained from the study, for example, the use of high power laser beams to illuminate water droplets as a means to increase their evaporation rate.

Some experimental studies were performed in the Soviet Union during the early seventies, for which the amount of information available in the modern literature is very limited, including the investigations performed by Bukatyi and Pogodaev (1970), Zuev *et al*. (1972), Rudash *et al*. (1973), and Kolosov *et al*. (1974). The utilization of a continuous CO_2 laser to illuminate water droplets suspended from thin filaments with radiation intensities below $10^3 \ \frac{\mathrm{W}}{\mathrm{cm}^2}$, and initial droplet diameters above 50 micrometers was common to all these investigations. A more recent experimental study on the effects of thermal radiation in water droplets (for which information is available) was conducted by Ivanov & Korovin (1978). The experimental setup consisted of free falling droplets being illuminated by a continuous CO_2 laser with a wavelength of 10.6 µm, in which the water is highly absorptive. The images of the droplets were captured with a high speed camera. The authors reported to have complemented the existing experimental data with a larger range of droplet diameters and radiative intensities (*i.e.*, d < 70 µm and $\dot{Q}''_{\mathrm{rad}} > 10^3 \frac{\mathrm{W}}{\mathrm{cm}^2}$) and also reported to have eliminated the temperature field distortions inside the liquid by the filaments used to hold the droplets due to the use of free falling droplets. A comparison between these experimental results and a more complete analytical model (*i.e.*, including the non-steady heating and evaporation), was summarized by Pustovalov & Romanov (1983), showing good agreement.

The investigation carried by Tseng *et al.* (2006) offers the most complete and up to date description of the effects of radiation on the evaporation rate of water droplets in a range of sizes between 5 and 1000 micrometers. This work developed a numerical model that studied the unsteady evaporation of single, pure water droplets surrounded by a blackbody environment with various temperatures (*i.e.*, 200 K – 2000 K). The internal circulation of the liquid phase was considered through the application of an *effective thermal conductivity* model, introduced by Abramzon and Sirignano (1989), in which the calculation of the rate of evaporation was done using a correlation that includes the knowledge of the Sherwood, Schmidt, and Reynolds numbers of the system and the Spalding mass transfer number. A geometrical optics model was applied to calculate the absorption properties of the water across the spectrum after assuming perfectly spherical droplets. The numerical predictions obtained in the investigation performed by Tseng *et al*. (2006) were compared with numerical predictions obtained by Miliauskas *et al*. (2006) for the case of droplets with an initial diameter and surface temperature of 200 μm and 280 K, respectively, and blackbody surrounding temperatures of 1500 K, showing some discrepancies between both results since the latter did not considered the thermophysical properties of water to be dependent on temperature.

The numerical predictions obtained by Tseng *et al*. (2006) were also compared to experimental data cited by Miliauskas *et al*. (2006) for the case of droplets (in the diameter range between 500 μm and 1500 μm) evaporating in dry air conditions with various environmental temperatures (*i.e*., 818 K, 981 K, and 1133 K) showing good agreement. However, the experimental studies cited lacked of a proper uncertainty analysis of the data, limiting their validity.

Although a large number of models to predict the evaporation rate of water droplets under the influence of infrared radiation are available in the literature for different size ranges and different physical considerations (*e.g*., unsteady heating and mass transfer, advective evaporation, internal circulation, temperature gradients inside the liquid phase), little amounts of experimental data can be found in order to validate them. Moreover, the computational complexity of these models makes their application difficult in scenarios where liquid droplets are carried in a gas stream enclosed by a flow tube with a radiative source located in one end of the tube (*e.g*., gas flaring devices) since virtually all of them assume the radiation coming from all directions. Additionally, neither numerical models nor experimental studies accounting for the combined effect of the relative humidity of the surrounding gases with the addition of infrared radiation on droplet evaporation was found in the literature. Therefore, the development of a computationally inexpensive model to predict the evaporation rate of water droplets subjected to infrared radiation and different relative humidities along with a simple set of experiments to test the validity of the predicted results is proposed.

1.3 Objectives of the Thesis

The main objective of the present work is to investigate the effects of the addition of constant infrared radiation flux on the evaporation rate of a single, spherical, quiescent pure water droplet in a size range of 50 µm – 10 µm under different environmental conditions of relative humidity (RH) and air temperature. The approach to investigate this phenomenon is presented in two different steps. First, a numerical model will be developed and different case scenarios will be simulated and compared to other models. Subsequently, the results predicted by the model will be validated experimentally. The experiments will be performed using a monodisperse droplet chain technique to generate the droplets and the shadowgraphy technique for their visualization and size measuring.

Specific objectives are introduced to aid in the accomplishment of the main objective:

- Develop a numerical model that estimates the evaporation rate of a single, pure liquid droplet in the micrometer range subject to constant radiation heat flux under different environmental conditions of relative humidity and air temperature.
- Design and build an experimental rig in order to generate water micro droplets of the desired size range, visualize them properly, and measure the change in droplet diameter with respect to time.
- Perform simulations using the numerical model, by varying the different conditions of relative humidity, temperature and infrared heat, in order to obtain the evolution of droplet size with respect to time for the various cases.
- Perform experiments varying relative humidity, temperature and infrared heat, in order to obtain the evolution of droplet size with respect to time for the various cases.
- Compare the experimental results with the predicted results to validate the numerical approach and the initial assumptions.

1.4 Thesis structure

In the present work, a simplified numerical model that estimates the evaporation rate of pure liquid substances immersed in a constant radiation field will be developed and validated experimentally using a monodisperse droplet chain technique to generate microscopic water droplets and an infrared laser at a wavelength of 2.8 μm as the heat source. The evolution of the droplet diameter will be measured using a shadowgraphy technique. The geometry of the rig, as well as the environmental and flow conditions tested, were selected in order to recreate the conditions found in common industrial and everyday applications.

In Chapter 2, the fundamental definitions of the diffusion-based evaporation process of liquids, along with some simplification assumptions and equations to determine the material properties are introduced. An energy balance is done in the liquid phase control volume of a spherical, isolated, quiescent pure liquid droplet subjected to a constant radiation source under the assumption of steady-state evaporation. Subsequently, the conservation of mass, energy and species equations are applied to the gas-vapor phase control volume of the droplet and rearranged to form a system of two ordinary differential equations that can be solved numerically. Finally, fundamental radiation definitions, assumptions and equations are introduced in order to determine an expression to estimate the total amount of infrared heat hitting the surface of the droplet.

In Chapter 3, a detailed description of the experimental rig and the instruments used is given. A special section is dedicated to the size measuring technique and the image calibration procedure used. The procedure to perform the experiments is carefully described in a series of steps. An analysis of the uncertainties and error propagation is also included in this chapter.

Chapter 4 presents a solution algorithm in which the system of ordinary differential equations (obtained in Chapter 2 from the application of the conservation of mass, energy and species equations) are equated with the initial energy balance and solved iteratively to determine a unique solution to the mass flux of water vapor under the steady state and other assumptions. The predicted results from the numerical model for the evaporation of water droplets with an initial diameter of 50 μm and subjected to different values of environmental RH and IR radiation density are also presented in this chapter.

A discussion of the experimental results and a comparison with numerical results are conducted in Chapter 5.

Finally, Chapter 6 summarizes the conclusions of the research and suggests future work.

Chapter 2

Model development for the evaporation of a quiescent, isolated, spherical micro droplet subjected to radiative heat

2.1 Fundamental definitions, theory, and classical model

At equilibrium, a single-component liquid-vapor system at a specified temperature (without the influence of electric fields) with a flat interface between the two phases establishes a unique state such that the pressure of the vapor is referred to as the saturation pressure. This vapor can co-exist with other gas-phase components such that its partial pressure remains equal to the saturation pressure if all the components act as ideal gases (*i.e.*, no interactions between particles).

Mass transfer between the two phases can be induced in an isothermal system by either reducing or increasing the vapor pressure of this component in the surrounding environment. For example, if the vapor pressure in the surroundings was reduced below the saturation pressure, liquid would evaporate in an attempt to re-establish equilibrium. Alternately, if the vapor pressure in the surroundings was increased above the saturation pressure then vapor would condense to become part of the liquid phase, again to try to re-establish the saturation pressure in the surroundings. The transport mechanism normally associated with isothermal evaporation and condensation is that the vapor immediately adjacent to the liquid layer is always at the saturation pressure. Subsequently, if the surroundings are at a different vapor pressure for that component (*i.e.*, at a different concentration) then Fickian diffusion will cause the net transport of mass. This transport, either to or from the vapor layer next to the liquid, would disrupt the quasi-equilibrium state that is believed to exist next to the liquid so that evaporation or condensation would occur, respectively. The energy considerations associated with this phase change are discussed later.

In the case of single-component curved liquid-gas interfaces, such as droplets, the surface tension and lower radius of curvature of the surface results in a higher vapor pressure next to the liquid, thus, increasing the evaporation rate for a given environmental condition. This effect of higher vapor pressure is called the Kelvin effect (named after Lord Kelvin) and can be considerable in the case of liquid droplets smaller than 1 µm.

Initially, when a liquid droplet with a uniform bulk temperature T_{s} is immersed in a quiescent gas of the same temperature, but with a vapor pressure below the saturation pressure, the process of evaporation will begin. This phase change from liquid to vapor has energy considerations, with the energy difference per unit mass between these phases while at the same temperature being the latent energy of evaporation. Seen from the perspective of the liquid, the large amount of energy that leaves with the relatively small amount of mass causes a reduction in the liquid temperature. Once the droplet temperature changes from the surroundings, then heat transfer will occur, which can further lead to temperature variations inside the droplet. Assuming a high thermal conductivity model, in which there is no temperature gradient inside the liquid phase (*i.e.*, $Bi \ll 1$, where Bi is the Biot number), thermally transient evaporation will occur until the temperature of the liquid bulk reaches a constant value of T_{e}. After this state is reached, the temperature is then considered constant for the remaining of the evaporation process. It can be demonstrated that the contribution of the transient evaporation period diminishes substantially with increasing time and decreasing droplet radius, and it represents less than 5 percent of the contribution to the total evaporation rate after 20 milliseconds of evaporation time for the case of droplets in standard conditions of pressure and temperature (Fuchs, 1959). In the current investigation, this thermal transient effect of evaporation will be assumed to be negligible. The fall in temperature of the droplets can also be considered instantaneous for the same time scale that the droplet takes to reach the steady state evaporation rate.

Maxwell (1877) developed the basic theory to describe the quasi-steady evaporation and condensation of spherical liquid droplets, motionless with respect to an infinite and steady environment. Maxwell's model was derived directly from Fick's first law of diffusion under the steady state assumption and by integrating the spatial rate of change of vapor concentration, ϕ (in units of mass of vapor per unit volume), with respect to the radius between the surface and an arbitrary position far away from the droplet in spherical coordinates.

Fick's first law of diffusion is:

$$j = -D \frac{\mathrm{d}\phi}{\mathrm{d}r} \tag{2.1}$$

where j is the mass flux of vapor, D is the diffusion coefficient, and r is the radial coordinate in a spherical coordinate system that represents the droplet and it surroundings. After rewriting Equation 2.1 in terms of the total mass flow rate of vapor, $\dot{m}$, and the surface area of the spherical droplet, A_{d}, it yields:

$$\dot{m} = -D\, A_{\mathrm{d}} \frac{\mathrm{d}\phi}{\mathrm{d}r} \tag{2.2}$$

The integration of Equation 2.2 between the surface of the droplet ($r = r_{\mathrm{s}}$) and an infinite position ($r = \infty$) far from the droplet's surface gives:

$$\dot{m} = 4\, \pi\, r_{\mathrm{s}}\, D\, (\phi_{\mathrm{s}} - \phi_{\infty}) \tag{2.3}$$

where ϕ_s and ϕ_∞ are the vapor concentrations at the surface of the droplet and infinity, respectively. The vapor concentration, ϕ, can be expressed by the following equation:

$$\phi = \frac{P_\mathrm{vap}\, W}{\mathrm{R}\, T} \tag{2.4}$$

where W is the molar mass of the evaporating liquid, R is the universal gas constant, T is the temperature of the vapor, in Kelvin; and P_vap is the partial pressure of the vapor. After substituting Equation 2.4 into Equation 2.3, Maxwell stated that the rate of diffusion of vapor across the surface of a liquid droplet of radius r_s under the steady state assumption can be expressed as:

$$\dot{m} = \frac{4\,\pi\, r_\mathrm{s}\, D\, W\, (P_\mathrm{vap,s} - P_\mathrm{vap,\infty})}{\mathrm{R}\, T} \tag{2.5}$$

where $\dot{m}$ is the mass flow rate of vapor expressed in dimensions of mass per unit time. $P_\mathrm{vap,s}$ and $P_\mathrm{vap,\infty}$ are the partial pressures of the vapor in the surface and at an infinite distance from the droplet, respectively. After examining Equation 2.5, it can be observed that the mass flow rate of vapor is dependent on the radius of the droplet, r_s. In a steady-state approach, and assuming that the temperature of the droplet is known, the initial droplet radius will be used to calculate the mass flow rate of vapor, $\dot{m}$, that has diffused away from the surface. However, as the droplet evaporates and becomes smaller, the radius will decrease and thus the mass flow rate initially calculated will no longer be correct. This creates the necessity of transforming the expression shown in Equation 2.5 into an expression that relates the evolution of the droplet radius with respect to the time variable in a quasi-steady approximation.

Although the steady state assumption is incorrect, the evaporation can be assumed to be quasi-stationary due to the fact that $\dot{m}$ can be treated as the instantaneous evaporation rate of a droplet of radius r_{s} at an instant t, thus:

$$\dot{m} = -\frac{\mathrm{d}m}{\mathrm{d}t} \tag{2.6}$$

where m is the mass of the liquid droplet and t is the time. By taking the mass and expressing it in terms of the droplet radius and its density, ρ_{liq}, the following expression can be obtained:

$$\dot{m} = -\frac{\mathrm{d}(\rho_{\mathrm{liq}}\,\frac{4}{3}\,\pi\, {r_{\mathrm{s}}}^{3}\,)}{\mathrm{d}t} \tag{2.7}$$

Since ρ_{liq} can be considered independent of time, it can be taken out of the time derivative and Equation 2.7 can be expressed as:

$$\dot{m} = -\,\frac{4}{3}\pi\,\rho_{\mathrm{liq}}\frac{\mathrm{d}\,{r_{\mathrm{s}}}^{3}}{\mathrm{d}t} \tag{2.8}$$

The expression obtained in Equation 2.8 for the mass flow rate of vapor can be inserted into Equation 2.5 to substitute $\dot{m}$. After doing this and applying the chain rule to the term $\frac{\mathrm{d}\,{r_{\mathrm{s}}}^{3}}{\mathrm{d}t}$, Maxwell's equation can be expressed as:

$$-\frac{\mathrm{d}\, {r_\mathrm{s}}^2}{\mathrm{d}t} = \frac{2\,D}{\rho_\mathrm{liq}} \frac{W\,(P_\mathrm{vap,s} - P_\mathrm{vap,\infty})}{\mathrm{R}\,T} \tag{2.9}$$

By integrating Equation 2.9 between the initial state $r_\mathrm{s,0}$ and t_0 to an arbitrary state r_s and t, the following expression can be obtained:

$${r_\mathrm{s}}^2 = {r_\mathrm{s,0}}^2 - \frac{2\,D}{\rho_\mathrm{liq}} \frac{W\,(P_\mathrm{vap,s} - P_\mathrm{vap,\infty})}{\mathrm{R}\,T} t \tag{2.10}$$

Equation 2.10 can be used to calculate the droplet radius at a time t based in the assumption that the initial droplet size and the substance properties D, ρ_liq, $P_{\mathrm{vap},s}$, $P_\mathrm{vap,\infty}$ and T are known. Additionally, these properties are functions of temperature; therefore T must be known in order to obtain a good estimate of how the droplet radius changes. Fuchs (1959) summarized the basic theory developed by Maxwell, but also included newer models in his review: The effects of Stefan flow (the transport of vapor due to the motion of the liquid droplet), non-spherical droplets, relative motion with respect to the surrounding gas and non-stationary evaporation. An equivalent expression for Equation 2.10 that includes the effects of Stefan flow was derived by Fuchs (1959) and later used by Vehring *et al.* (2007) for the analytical determination of the evaporation rate of pure liquid droplets. This expression is:

$${r_\mathrm{s}}^2 = {r_\mathrm{s,0}}^2 - \frac{2\,D\,\rho_\mathrm{g}}{\rho_\mathrm{liq}} \ln\left(\frac{1 - Y_\infty}{1 - Y_\mathrm{s}}\right) t \tag{2.11}$$

Where Y_s and Y_∞ are the mass ratios (in units of mass of vapor per unit mass of dry air) of water vapor at the surface and infinite radial positions, respectively. The introduction of Y simplifies the understanding of the evaporation phenomenon because the concepts of pressure, molecular weight and temperature disappear from the expression and is replaced by a mass concentration difference; however, a known T is still needed to determine the mass ratio of vapor at the surface because it is assumed to be at saturation. Stefan flow effects are significant only when the ratio of vapor pressure to total atmospheric pressure is not small (Fuchs, 1959). It was reported that for droplets at room temperature and 1 atm the error introduced by not taking into account Stefan flow was close to 1 percent (Fuchs, 1959). An equivalent expression for Equation 2.10 without the effects of Stefan flow can be expressed in terms of the mass fraction of water vapor as follows:

$$r_{\mathrm{s}}{}^2 = r_{\mathrm{s},0}{}^2 - \frac{2\,D\,\rho_{\mathrm{g}}}{\rho_{\mathrm{liq}}}(Y_{\mathrm{s}} - Y_{\infty})t \tag{2.12}$$

Equations 2.11 and 2.12 are equivalent to the expression commonly used in the literature to describe the evaporation of droplets under a constant evaporation rate assumption:

$$d(t)^2 = d_0{}^2 - \kappa\, t \tag{2.13}$$

Where d_0 is the initial droplet diameter, $d(t)$ the diameter after a time t, and κ the evaporation rate, in meters squared per unit time. It can be observed that under these assumptions, evaporation is a surface phenomenon rather than a volumetric phenomenon. After inserting this expression into Equations 2.11 and 2.12, a definition of the constant evaporation rate with and without the effects of Stefan flow can be obtained, respectively:

$$\kappa = 8\,D\,\frac{\rho_{\mathrm{g}}}{\rho_{\mathrm{l}}}\ln\left[\frac{1 - Y_{\infty}}{1 - Y_{\mathrm{s}}}\right] \tag{2.14}$$

$$\kappa = 8\,D\,\frac{\rho_\mathrm{g}}{\rho_\mathrm{l}}\,(Y_\mathrm{s} - Y_\infty) \tag{2.15}$$

The temperature of the droplet surface under the steady-state assumption can be obtained analytically by doing an energy balance in the gas and liquid phases of the evaporating droplet. In the gas phase, if radiation is ignored, the net heat transfer provided by the gas phase, $\dot{Q}_\mathrm{g}$, is equal to the enthalpy change of the vapor minus the heat that is conducted towards the droplet surface:

$$\dot{Q}_\mathrm{g} = \dot{m}\,c_p(T - T_\mathrm{s}) - 4\,\pi\,r^2\,\lambda_\mathrm{g}\frac{\mathrm{d}T}{\mathrm{d}r} \tag{2.16}$$

Where c_p is the specific heat capacity of the gas mixture at constant pressure, λ_g is the thermal conductivity of the gas, and T is the temperature of the gas at an arbitrary radial distance between the droplet surface and infinity. Integration of Equation 2.16 between boundary conditions at $r = r_\mathrm{s}$ and $r = r_\infty$ yields:

$$\dot{m}\,c_p = 4\,\pi\,\lambda_\mathrm{g}\,r_\mathrm{s}\,\ln\left[1 - \frac{\left(\dot{m}\,c_p(T_\infty - T_\mathrm{s})\right)}{\dot{Q}_\mathrm{g}}\right] \tag{2.17}$$

Maxwell's equation (Equation 2.3) can be re-written in terms of the vapor mass fraction Y and equated with Equation 2.17 to form:

$$Y_\mathrm{s} - Y_\infty = \frac{\lambda_\mathrm{g}}{c_p D\, \rho_\mathrm{g}} \ln\left[1 - \frac{\left(\dot{m}\, c_p (T_\infty - T_\mathrm{s})\right)}{\dot{Q}_\mathrm{g}}\right] \tag{2.18}$$

After exponentiation of both sides of Equation 2.18:

$$\mathrm{e}^{(Y_\mathrm{s} - Y_\infty)} = \left[1 - \frac{\left(\dot{m}\, c_p (T_\infty - T_\mathrm{s})\right)}{\dot{Q}_\mathrm{g}}\right]^{\left(\frac{\lambda_\mathrm{g}}{c_p D\, \rho_\mathrm{g}}\right)} \tag{2.19}$$

In the absence of heat radiation, the energy provided by the gas phase, $\dot{Q}_\mathrm{g}$ is equal to the energy required by the liquid phase for the enthalpy change of vaporization:

$$\dot{Q}_\mathrm{g} = \dot{m}\, h_{fg} \tag{2.20}$$

Thus, Equation 2.20 can be substituted into Equation 2.19 and the unknown variables $\dot{m}$ and $\dot{Q}_\mathrm{g}$ will disappear, as shown in Equation 2.21. The remaining expression can be used to calculate iteratively the value of T_s, which is equal to the equilibrium temperature of the droplet surface under the steady-state assumption. The mass ratios of water vapor at the surface, Y_s, can be calculated through the Clausius-Clapeyron relations using the temperature T_s. And Y_∞ and T_∞ are far-field boundary conditions.

$$Y_{\mathrm{s}} - Y_{\infty} = \left(\frac{\lambda_{\mathrm{g}}}{c_p D\, \rho_{\mathrm{g}}}\right) \mathrm{Ln}\left[1 - \frac{\left(c_p (T_{\infty} - T_{\mathrm{s}})\right)}{h_{fg}}\right] \tag{2.21}$$

After the temperature is determined, the diffusion rate, mass ratios, and densities can be obtained. Then, the evaporation rate can be calculated using Equations 2.14 and 2.15. On the other hand, by introducing an external energy source, such as thermal radiation, and neglecting its interaction with the gaseous phase, the energy needed for the enthalpy change of vaporization will be the sum of the heat provided by the gas phase through conduction, plus the radiation absorbed by the liquid phase:

$$\dot{Q}_{\mathrm{g}} + \dot{Q}_{\mathrm{rad}} = \dot{m}\, h_{fg} \tag{2.22}$$

By inserting Equation 2.22 into Equation 2.19 it can be noticed that the mass flux parameter $\dot{m}$ can no longer be simplified and therefore the obtained expression cannot be used to determine the equilibrium surface temperature of the droplet. Hence, evaporation rate cannot be determined easily and is not just the superposition of evaporation without radiation and the some additional amount associated with the extra flow of energy due to radiation.

2.2 Model development to include the effects of radiation

In earlier works (Vehring *et al.*, 2007) it was common to identify *a priori* whether the rate limiting processes on the evaporation rate was the transport of heat into the droplet to provide the energy for the phase change or the mass diffusion away from the surface set by the gradient in vapor concentration. Knowing which process limits the rate of evaporation allows for simplified models to be developed, but when neither process dominates, such as the case when heating by radiation of an arbitrary quantity, then the evaporation of water droplets is a complex coupling of energy and mass transfer phenomenon. Following is the development of a model that includes these coupled effects.

Initial Assumptions:

1. Quasi-steady process.
2. Constant radiation work/heat flux (W/m^2) striking the liquid droplet (*i.e.*, the gas phase does not absorb radiation).
3. Spherical coordinates, radial symmetry: Rate of change and transport phenomena only occurs in the radial direction (*i.e.,* the concentration of water vapor and temperature of the gas are functions only of the coordinate “r” and do not depend on coordinates “θ” and “φ”).
4. Quiescent droplet (*i.e.*, there is no relative velocity between the droplet and the surrounding gas).
5. The material properties: λ, c_p and D are assumed to be constant, and are evaluated at the droplet surface conditions.
6. There is no pressure gradient in the gas phase.
7. There is no temperature gradient inside the droplet (*i.e.*, Bi << 1).
8. Kelvin effect due to small droplet radius is negligible.
9. The particle radius is much larger than the mean free path of the surrounding gas – continuum theory applies.

A detailed explanation of the basic initial assumptions made in this section is presented in Appendix A.

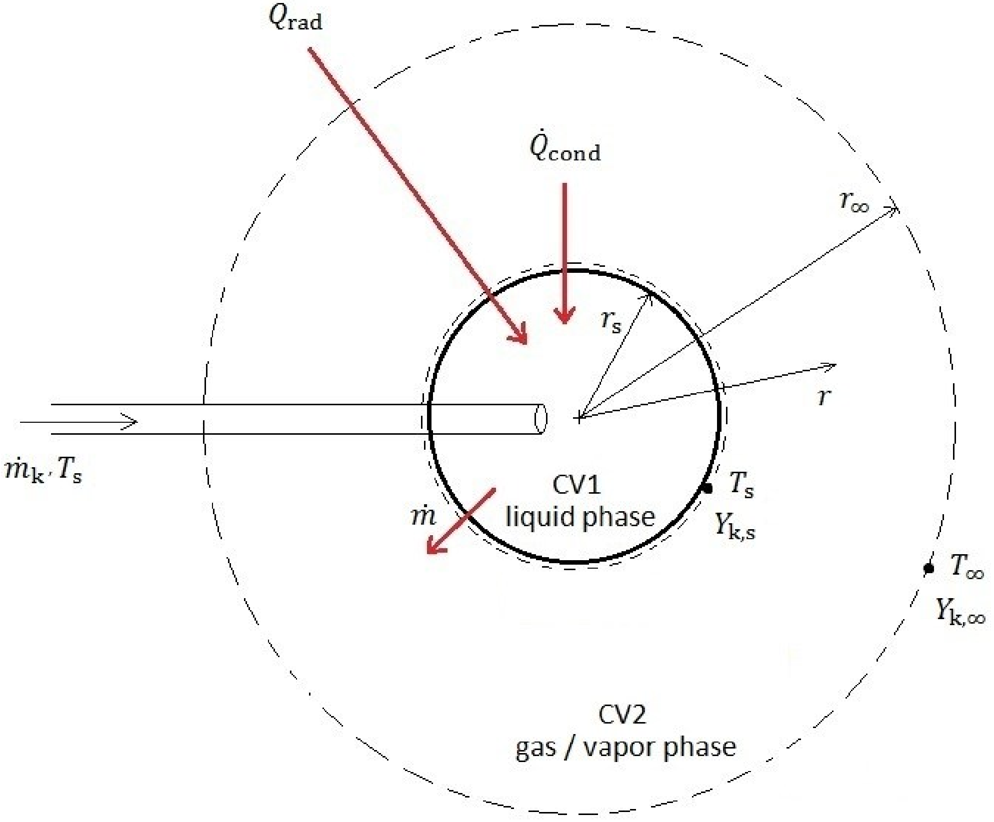

Figure 2.1: Control volume schematic

Figure 2.1 represents a schematic of the coupled heat and mass transfer problem that is being proposed to be solved. It consists of three concentric spheres that determine the boundaries of the two control volumes that will be used to describe the physics of the phenomenon. The inner, continuous line represents the liquid sphere (which also defines control volume 1, CV1) of radius r_{s}, where "s" means "surface". The material properties of the liquid in control volume 1, as well as its temperature, are considered uniform in space.

The middle and outer spheres, shown as dashed lines, represent the boundaries of interest for the gas/vapor phase (also defines control volume 2, CV2). The infinity symbol, ∞, represents a distance far away from the droplet surface such that the properties at this point are not affected by variations at the droplet surface.

A small hollow cylinder or "tube" has been inserted into the liquid phase boundary as a concrete reminder in the figure of the addition of liquid water needed to satisfy the steady state assumption. The liquid enters CV1 at a constant temperature equal to the droplet temperature and mass flow rate needed for the steady state assumption.

An incoming vector, $\dot{Q}_{\mathrm{rad}}$ represents the radiative energy flux that goes into the liquid phase. It is important to remark that this radiative energy flux is assumed not to interact with the surrounding gas/vapor phase.

2.2.1 Liquid Phase Control Volume:

An energy balance is done in the liquid phase control volume (control volume 1) as follows:

$$\frac{\mathrm{d}E}{\mathrm{d}t} = \dot{E}_{\mathrm{in}} - \dot{E}_{\mathrm{out}} + \dot{W}_{\mathrm{f,in}} - \dot{W}_{\mathrm{f,out}} + \dot{Q}_{\mathrm{rad}} + \dot{Q}_{\mathrm{cond}} \tag{2.23}$$

Where $\frac{\mathrm{d}E}{\mathrm{d}t}$ is the time rate of change of total energy within a control volume. $\dot{E}_{\mathrm{in}}$ and $\dot{E}_{\mathrm{out}}$ are the total rate of energy going in and coming out of the control volume carried with the mass crossing its boundaries, respectively. Similarly, $\dot{W}_{\mathrm{f,in}}$ and $\dot{W}_{\mathrm{f,out}}$ are the rate of work done by the fluid crossing the boundaries (*i.e.*, flow work); $\dot{Q}_{\mathrm{rad}}$ is the external work into the system (representing the radiative heat flux) and $\dot{Q}_{\mathrm{cond}}$ is the total heat conducted into the liquid surface from the surrounding gas.

Equation 2.23 states that the rate of change of energy with respect to time is equal to the energy that goes into the system minus the energy that goes out, plus the difference between the flow works, plus the external work exerted to the system (*i.e.*, radiation), plus the heat that goes in due to conduction. The time dependent term is set to zero for a steady-state approach. Additionally, if the kinetic and potential energy components of the in and out flows are assumed small, then the energy term $\dot{E}$ becomes internal energy and can be combined with the flow work term, $\dot{W}_{\mathrm{f}}$, such that $\dot{H}_{\mathrm{in}} = \dot{E}_{\mathrm{in}} + \dot{W}_{\mathrm{f,in}}$, $\dot{H}_{\mathrm{out}} = \dot{E}_{\mathrm{out}} + \dot{W}_{\mathrm{f,out}}$, $\dot{H}_{\mathrm{out}} - \dot{H}_{\mathrm{in}} = \dot{m}(h_{\mathrm{out}} - h_{\mathrm{in}})$, and thus $\dot{H}_{\mathrm{out}} - \dot{H}_{\mathrm{in}} = \dot{m}h_{fg}$ (since there is no change in sensible energy) to yield the difference of fluid enthalpies.

$$0 = -\dot{m}\, h_{fg} + \dot{Q}_{\mathrm{rad}} + \dot{Q}_{\mathrm{cond}} \tag{2.24}$$

Where $\dot{m}$ is defined by the conservation of mass principle as the mass flow rate of liquid water being added to the droplet or the vapor that is being evaporated away from the droplet surface; and h_{fg} is the latent heat of vaporization, sometimes given the notation L in the literature. In Equations 2.23 and 2.24, as seen in Figure 2.1, the term $\dot{Q}_{\mathrm{rad}}$ represents the radiative heat. The radiative energy is believed to be absorbed almost entirely by the liquid phase because the number density of the particles in the liquid is more than three orders of magnitude higher than in the vapor phase; hence, its interaction with the surrounding gas and vapor is often neglected. After re-arranging Equation 2.24 to find an expression for the mass flux, it yields:

$$\dot{m} = \frac{\dot{Q}_{\mathrm{cond}} + \dot{Q}_{\mathrm{rad}}}{h_{fg}} \tag{2.25}$$

Equation 2.25 gives the mass flux of water that is being evaporated away from a droplet surface. The conduction of heat can be linked to the vapor phase by using Fourier's Law, and Equation 2.25 results in:

$$\dot{m} = \frac{\left(\lambda\, A_{\mathrm{s}} \left.\frac{\mathrm{d}T}{\mathrm{d}r}\right|_{r=r_{\mathrm{s}}}\right) + \dot{Q}_{\mathrm{rad}}}{h_{fg}} \tag{2.26}$$

Where the sign on the heat transfer substitution is consistent with the thermodynamic schematic shown in Figure 2.1 (*i.e.,* a positive gradient in T with r leads to heat going into the droplet), λ is the thermal conductivity of the gas/vapor mixture and A_{s} is the surface area of the droplet. The value of $\left.\frac{\mathrm{d}T}{\mathrm{d}r}\right|_{r=r_{\mathrm{s}}}$, which is also on the gas-vapor side of the control volume, can be obtained by doing an energy balance in the gas/vapor phase control volume (CV2) to find the temperature distribution of the surroundings, subject to conditions of temperature and water vapor concentration specified far away from the surface.

2.2.2 Gas/vapor Phase Control Volume

The evaporation process in the gas/vapor phase is a function not only of the temperature gradient but also of the concentration gradient of water vapor in air. The two mechanisms that drive the evaporation phenomenon are diffusion and advection. Each mechanism is present in both heat and mass transfer, *i.e.*, heat conduction and species diffusion are both analog phenomena. As well, heat convection and the Stefan flow phenomenon are analog advective mechanisms. The main difference in these two transport phenomena is that diffusion transports heat/mass by a difference between temperature/concentration and advection requires movement of the bulk material.

Due to the fact that evaporation is a coupled heat-mass transfer problem, the description of the physics that governs the problem should consider the conservation of mass, energy and species equations. It is important to remark that the momentum conservation equation will not be used due to the fact that the pressure field in the gas/vapor control volume is assumed to be constant.

The gas/vapor phase control volume, as seen in Figure 2.1, consists of a shell of thickness $r_\infty - r_\mathrm{s}$, where r_∞ is a distance far away from the droplet surface, usually two orders of magnitude higher, such that temperature and/or mass concentration at this location is not affected by any change in temperature or mass concentration in the droplet surface. The temperature and mass fraction of species k far from the surface, T_∞ and $Y_{k,\infty}$, respectively, are specified to be at a constant temperature and relative humidity.

2.2.2.1 Conservation of Mass:

The conservation of mass in its most general form (Kee, Coltrin, & Glarborg, 2003) can be described by:

$$\frac{\mathrm{d}\rho}{\mathrm{d}t} + \nabla \cdot (\rho v) = 0 \tag{2.27}$$

where ρ, v and t are the density of the fluid, the velocity vector in spherical coordinates and the time, respectively. After neglecting the rate of change of density with respect to time due to the steady state assumption, the equation equals:

$$\nabla . (\rho v) = 0 \tag{2.28}$$

Expanding the operator ∇ in spherical coordinates yields:

$$\frac{1}{r^2}\frac{\mathrm{d}(r^2\rho\, v_r)}{\mathrm{d}r}+\frac{1}{r\ \sin\theta}\frac{\mathrm{d}(\rho\, v_\theta \sin\theta)}{\mathrm{d}\theta}+\frac{1}{r\ \sin\theta}\frac{\mathrm{d}(v_{\varphi\ \rho})}{\mathrm{d}\varphi}=0 \tag{2.29}$$

Only the radial coordinates will survive due to the initial assumptions:

$$\frac{1}{r^2}\frac{\mathrm{d}(r^2\rho\, v_r)}{\mathrm{d}r}=0 \tag{2.30}$$

This equals:

$$\frac{\mathrm{d}(r^2\rho\, v_r)}{\mathrm{d}r}=0 \tag{2.31}$$

Integrating both sides of the differential equation yields:

$$\int 1\,\mathrm{d}(r^2\rho\, v_r)=\int 0\,\mathrm{d}r \tag{2.32}$$

After integrating, this yields:

$$r^2\rho\, v_r + C_1 = C_2 \tag{2.33}$$

where the constants C_1 and C_2 were added to account for the solution of the integral without defined boundaries. To find the values for the constants, the equation should be evaluated at the surface conditions and the conditions far from the droplet

$$\begin{aligned} {r_\mathrm{s}}^2\rho_\mathrm{s}\, v_{r_\mathrm{s}} + \mathrm{C}_1 &= \mathrm{C}_2 \\ {r_\infty}^2\rho_\infty\, v_{r_\infty} + \mathrm{C}_1 &= \mathrm{C}_2 \end{aligned} \tag{2.34}$$

Solving the system of equations yields:

$$ {r_\mathrm{s}}^2\rho_\mathrm{s}\, v_{r_\mathrm{s}} = {r_\infty}^2\rho_\infty\, v_{r_\infty} = r^2\rho\, v_r = \frac{\dot{m}}{4\pi} \tag{2.35}$$

Equation 2.35 simply states that the mass flow rate, $\dot{m}_\mathrm{s}$, that leaves the droplet surface equals the mass flow rate that leaves the boundary of the control volume $\dot{m}_\infty$, or any radial position, therefore the mass flow rate is conserved; also the velocity decreases as $\frac{1}{r^2}$.

2.2.2.2 Conservation of Energy:

The general form of the conservation of energy equation shown below includes the effects of work, heat conduction, chemical reaction ($\sum_{k=1}^{K}\nabla\cdot h_k j_k$), and dissipation ($\Phi$). The rate of change of energy does not include the effect of potential or kinetic energies (Kee, Coltrin, & Glarborg, 2003).

$$\rho\ \frac{\mathrm{D}h}{\mathrm{D}t} = \frac{\mathrm{D}P}{\mathrm{D}t} + \nabla\cdot(\lambda\ \nabla\mathrm{T}) - \sum_{k=1}^{K}\nabla\cdot h_k j_k + \Phi \tag{2.36}$$

After neglecting the work, chemical reaction and dissipation terms:

$$\rho\ \frac{\mathrm{D}h}{\mathrm{D}t} = \nabla\cdot(\lambda\ \nabla\mathrm{T}) \tag{2.37}$$

Expanding the substantial derivative and the **∇** operator:

$$\rho\ \left[\frac{\mathrm{d}h}{\mathrm{d}t} + v_r\frac{\mathrm{d}h}{\mathrm{d}r} + \frac{v_\theta}{r}\frac{\mathrm{d}h}{\mathrm{d}\theta} + \frac{v_\varphi}{r\sin\theta}\frac{\mathrm{d}h}{\mathrm{d}\varphi}\right] = \nabla\cdot\left(\lambda\ \left[\frac{\mathrm{d}T}{\mathrm{d}r}\hat{r} + \frac{1}{r}\frac{\mathrm{d}T}{\mathrm{d}\theta}\hat{\theta} + \frac{1}{r\sin\theta}\frac{\mathrm{d}T}{\mathrm{d}\varphi}\hat{\varphi}\right]\right) \tag{2.38}$$

where $\hat{r}$, $\hat{\theta}$, $\hat{\varphi}$ are unit vectors that represent the radial, polar and azimuthal directions in the spherical coordinate system. After neglecting the transient, polar and azimuthal terms and keeping only the radial coordinates:

$$\rho\ \left[v_r\frac{\mathrm{d}h}{\mathrm{d}r}\right] = \nabla\cdot\left(\lambda\ \left[\frac{\mathrm{d}T}{\mathrm{d}r}\hat{r}\right]\right) \tag{2.39}$$

This equals:

$$\rho\, v_r \frac{\mathrm{d}h}{\mathrm{d}r} = \frac{1}{r^2}\frac{\mathrm{d}}{\mathrm{d}r}\left(r^2\lambda\,\frac{\mathrm{d}T}{\mathrm{d}r}\right) \tag{2.40}$$

By expressing the enthalpy in terms of the temperature ($h = c_p\, T$), which is an ideal gas assumption, we obtain:

$$\rho\, v_r \frac{\mathrm{d}(c_p T)}{\mathrm{d}r} = \frac{1}{r^2}\frac{\mathrm{d}}{\mathrm{d}r}\left(r^2\lambda\,\frac{\mathrm{d}T}{\mathrm{d}r}\right) \tag{2.41}$$

The material properties c_p and λ are assumed independent of r, therefore:

$$\rho\, v_r c_p \frac{\mathrm{d}T}{\mathrm{d}r} = \frac{\lambda}{r^2}\frac{\mathrm{d}}{\mathrm{d}r}\left(r^2\,\frac{\mathrm{d}T}{\mathrm{d}r}\right) \tag{2.42}$$

After re-arrangement and introduction of the thermal Peclet number (Pe_{T}):

$$Pe_{\mathrm{T}} \frac{\mathrm{d}T}{\mathrm{d}r} = \frac{1}{r}\frac{\mathrm{d}}{\mathrm{d}r}\left(r^2\,\frac{\mathrm{d}T}{\mathrm{d}r}\right) \tag{2.43}$$

where:

$$Pe_{\mathrm{T}} = \frac{r\, v_r\, \rho\, c_p}{\lambda}$$

The thermal Peclet number was included in the final expression of the energy conservation equation to compare the heat transport phenomenon with the mass transport phenomenon as it will be shown in Equation 2.53. After inserting the conservation of mass expression (Equation 2.35) into Equation 2.43, the following expression can be obtained:

$$A' \frac{\mathrm{d}T}{\mathrm{d}r} = \frac{\mathrm{d}}{\mathrm{d}r}\left(r^2 \frac{\mathrm{d}T}{\mathrm{d}r}\right) \tag{2.44}$$

where:

$$A' = \frac{\dot{m}\, c_p}{4\, \pi\, \lambda}$$

An analytical solution for Equation 2.44 can be found with its respective specified temperature boundary conditions. Equations 2.45 and 2.46 show the expressions for the temperature function and the slope of the temperature distribution at the droplet surface, respectively:

$$T(r) = T_\infty + B \exp\left(\frac{-A'}{r}\right) - B \tag{2.45}$$

$$\left.\frac{\mathrm{d}T}{\mathrm{d}r}\right|_{r=r_\mathrm{s}} = \frac{A'\, B \exp\left(\frac{-A'}{r_\mathrm{s}}\right)}{{r_\mathrm{s}}^2} \tag{2.46}$$

where A' is the advective coefficient shown in Equation 2.44 and:

$$B = \frac{(T_\mathrm{s} - T_\infty)\exp\left(\frac{A'}{r_\mathrm{s}}\right)}{1 - \exp\left(\frac{A'}{r_\mathrm{s}}\right)}$$

The expression for $\left.\frac{\mathrm{d}T}{\mathrm{d}r}\right|_{r=r_\mathrm{s}}$ is what is needed for the conduction of heat back into the droplet as described in Equation 2.26.

2.2.2.3 Conservation of Species:

The analysis begins by assuming that the mass transfer will occur only between 2 different substances ($k = 2$), water and air (*i.e.,* not separating out the oxygen and nitrogen). The dissolving of gas into the liquid phase is neglected. To correctly formulate the problem, only $k - 1$ equations should be used, as the use of the other species conservation equation will be redundant and provides the same information as using the mass conservation equation.

$$\rho \frac{\mathrm{D}Y_k}{\mathrm{D}t} = -\nabla . j_k + \dot{\omega}_k W_k \tag{2.47}$$

where the term $\dot{\omega}_k W_k$ accounts for the chemical reactions between the species (Kee, Coltrin, & Glarborg, 2003), Y_k is the mass fraction of species k, and j_k is the mass flux per unit area of one of the species with respect to another. Since there is no chemical reaction, the term $\dot{\omega}_k W_k$ can be neglected, thus:

$$\rho \frac{\mathrm{D}Y_k}{\mathrm{D}t} = -\nabla . j_k \tag{2.48}$$

After expanding the material derivative and the divergence of the mass flux and simplifying:

$$\rho\, v_r \frac{\mathrm{d}Y_k}{\mathrm{d}r} = -\frac{1}{r^2}\frac{\mathrm{d}(r^2 j_k)}{\mathrm{d}r} \tag{2.49}$$

The mass flux of species k per unit area, j_k, can be modeled by Fick's first law of diffusion:

$$j_k = -\rho\, D_{k,\mathrm{mix}} \nabla Y_k \tag{2.50}$$

The variable $D_{k,\mathrm{mix}}$ is the diffusivity of species k with respect to the other species of the mixture and can be calculated with an empirical expression found in the literature, as it will be shown later. Equation 2.50 in spherical coordinates equals:

$$j_k = -\rho\, D_{k,\mathrm{mix}} \frac{\mathrm{d}Y_k}{\mathrm{d}r} \tag{2.51}$$

By inserting Fick's Law into the differential equation it yields:

$$\rho\, v_r \frac{\mathrm{d}Y_k}{\mathrm{d}r} = \frac{1}{r^2}\frac{\mathrm{d}}{\mathrm{d}r}\left(r^2 \rho\, D_{k,\mathrm{mix}} \frac{\mathrm{d}Y_k}{\mathrm{d}r}\right) \tag{2.52}$$

The diffusivity can be considered independent of r, especially in dilute systems, and therefore can be taken out of the derivative. This assumption may be a concern for temperatures near the boiling point with the existence of a high concentration of water vapor near the droplet surface in contrast to the value of the concentration in the rest of the gas phase. After re-arranging the terms and the introduction of the mass Peclet number (Pe_{M}), the species equation results as:

$$\rho \, Pe_{\mathrm{M}} \frac{\mathrm{d}Y_k}{\mathrm{d}r} = \frac{1}{r} \frac{\mathrm{d}}{\mathrm{d}r} \left(r^2 \rho \, \frac{\mathrm{d}Y_k}{\mathrm{d}r} \right) \tag{2.53}$$

where:

$$Pe_{\mathrm{M}} = \frac{r \, v_r}{D_{k,\mathrm{mix}}}$$

It is important to acknowledge the existence of an analogy between Equations 2.53 and 2.43. In both differential equations the term in the left hand side represents the advection or transport phenomenon due to the motion of the bulk material away from the droplet surface. The term on the right hand side represents the diffusive part or transport phenomena due to a gradient in temperature or concentration.

Equation 2.53 differs from Equation 2.43 by having the density of the mixture gas inside a first order derivative with respect to radius. If an assumption of a constant density could be made, then the density variable in both sides of Equation 2.53 would cancel and its solution will be given by a similar expression to Equation 2.45. Unfortunately, the density of the gas mixture cannot be considered constant as it is a function of the mass fractions of water vapor and air and temperature, and these values may change dramatically with radius. The fact that Equation 2.53 includes the variable density in both sides of the equal sign makes it coupled with the energy equation, hence a variation in the temperature profile of the gas mixture will automatically affect the mass fraction profile and therefore the evaporation rate will change.

As a result, the coupling between the transport of energy and mass is not symmetric. While the temperature directly depends only on the mass flow rate (*i.e.*, coefficient A' in Equation 2.46, which is affected by mass transport), the mass fraction depends directly on both the mass transport and the temperature field. A better known comparison between the energy and mass transport phenomena can be made by the Lewis number, which is simply the ratio between the mass and thermal Peclet numbers:

$$Le = \frac{Pe_{\mathrm{M}}}{Pe_{\mathrm{T}}} = \frac{\frac{r\, v_r}{D_{k,\mathrm{mix}}}}{\frac{r\, v_r\, \rho\, c_p}{\lambda}} = \frac{\lambda}{D_{k,\mathrm{mix}}\, \rho\, c_p} = \frac{a}{D_{k,\mathrm{mix}}} \tag{2.54}$$

where $a = \frac{\lambda}{\rho\, c_p}$ is called the thermal diffusivity. The Lewis number is therefore a ratio between the heat diffusivity and the mass diffusivity. It gives the relative importance of each transfer phenomenon (heat or mass) in the overall process. To express the species conservation equation in terms of the evaporation rate, it is useful to insert the conservation of mass expression into Equation 2.53; this results in:

$$\left(\frac{\dot{m}}{4\, \pi\, D_{k,\mathrm{mix}}}\right)\frac{\mathrm{d}Y_k}{\mathrm{d}r} = \frac{\mathrm{d}}{\mathrm{d}r}\left(r^2 \rho\, \frac{\mathrm{d}Y_k}{\mathrm{d}r}\right) \tag{2.55}$$

The density ρ can be expressed in terms of the temperature, pressure and molecular mass of the mixture by using the ideal gas law:

$$\rho = \frac{P}{R_{\text{mix}} T} = \frac{P\,\overline{W}}{R\,T} \tag{2.56}$$

where P, $\overline{W}$, R_{mix}, and R are the total pressure, the molecular mass of the mixture, the mixture gas constant and the universal gas constant, respectively. The molecular mass of the mixture in a $k = 2$ species system is a function of the mass fraction of species k:

$$\overline{W} = \sum_{k=1}^{2} (Y_k\, W_k) \tag{2.57}$$

where W_k is the molecular mass of each species. In this case, Equation 2.57 can be expressed as:

$$\overline{W} = Y_{\text{vap}}\, W_{\text{vap}} + (1 - Y_{\text{vap}})\, W_{\text{air}} \tag{2.58}$$

After substituting both Equations 2.58 and 2.56 into Equation 2.55, and taking the constant values P and R out of the derivative, we obtain the final expression for the conservation of species equation:

$$\left(\frac{\dot{m}\,R}{4\,\pi\,D_{k,\mathrm{mix}}\,P}\right)\frac{\mathrm{d}Y_k}{\mathrm{d}r}=\frac{\mathrm{d}}{\mathrm{d}r}\left(r^2\,\frac{[Y_k\,W_{\mathrm{vap}}+(1-Y_k)\,W_{\mathrm{air}}]}{T}\,\frac{\mathrm{d}Y_k}{\mathrm{d}r}\right) \tag{2.59}$$

Solving Equation 2.59 requires a significant computational effort and cannot be done analytically as Equation 2.44. Instead, it can be solved using ordinary differential equation solvers available in commercial software, *e.g.*, Matlab. In order to solve Equation 2.59 numerically, some simplifications can be made. The most important is to introduce the assumption of neglecting the effects of Stefan flow, or advective mass transfer.

This simplification can be made only if the ratio of vapor pressure to total atmospheric pressure is much less than 0.1 or 10 percent (Finlay, 2001). Whether this advection term can be neglected in the energy equation requires knowledge of the thermal Peclet number, but since an analytical solution exists for the energy equation it can be left in without increasing complexity. After neglecting the advective term in Equation 2.59, the second order differential equation yields the expression shown by Equation 2.60. It will be demonstrated later by the numerical and experimental solutions that this simplification does not affect the result.

$$\frac{\mathrm{d}}{\mathrm{d}r}\left(r^2\,\frac{[Y_k\,W_{\mathrm{vap}}+(1-Y_k)\,W_{\mathrm{air}}]}{T}\,\frac{\mathrm{d}Y_k}{\mathrm{d}r}\right)=0 \tag{2.60}$$

After expanding the derivatives and introducing the analytic solution for T, the differential equation can be written in terms of mass fraction and r only. Equation 2.61 can be solved using a numerical method *e.g.,* Runge-Kutta, Euler.

$$\frac{\mathrm{d}^2 Y_k}{\mathrm{d}r^2} = \left(\frac{\frac{A' \, B \exp\left(\frac{-A'}{r}\right)}{r^2}}{T_\infty + B \exp\left(\frac{-A'}{r}\right) - B} - \frac{(W_{\mathrm{vap}} - W_{\mathrm{air}}) r^2 \frac{\mathrm{d}Y_k}{\mathrm{d}r} + 2\,(W_{\mathrm{vap}} - W_{\mathrm{air}}) r \, Y_k + 2 W_{\mathrm{air}} r}{(W_{\mathrm{vap}} - W_{\mathrm{air}}) \, r^2 \, Y_k + W_{\mathrm{air}} \, r^2} \right) \frac{\mathrm{d}Y_k}{\mathrm{d}r} \tag{2.61}$$

2.2.3 Models for transport properties:

The material properties for the studied components (water and air) need to be accurately determined in order to avoid the introduction of errors in the numerical calculation. In the present work, some of the properties were estimated by fitting data obtained in book tables. Other properties were calculated using correlations given in previous investigations. In general, a good agreement between the data and the correlations was obtained for a range of temperatures between 273 and 373 Kelvin and a pressure of 1 atm.

The diffusion coefficient of water vapor was estimated using a correlation proposed by Marrero and Mason (1972), where D is in $\left[\frac{\mathrm{m}^2}{\mathrm{s}}\right]$ and T_{s} is in Kelvin:

$$D_{k,\mathrm{mix}} = 1.87 \times 10^{-10} \, {T_{\mathrm{s}}}^{2.072} \tag{2.62}$$

The vapor pressure was calculated using the Antoine equation:

$$P_{\text{vap}} = 10^{\left(\text{A} - \frac{\text{B}}{T + \text{C}}\right)} \tag{2.63}$$

where the parameters A, B, and C were obtained by fitting the water vapor data from the *CRC handbook of chemistry and physics* (2002), as it was described by Vehring *et al.* (2007):

$$\text{A} = 10.113$$

$$\text{B} = 1685.6$$

$$\text{C} = -43.154$$

T = Temperature of the vapor (in Kelvin)

P_{vap} = Saturation pressure of water vapor in Pascal

The density, specific heat capacity and thermal conductivity of dry air and water (in liquid and vapor phase) were determined as functions of temperature by fitting data obtained in the tables of properties from Cengel and Ghajar (1998) (See Appendix B for detailed information):

$$\rho_{\text{liq}} = -7 \times 10^{-6}\, T^3 + 6 \times 10^{-3}\, T^2 - 2.1739\, T + 1296 \tag{2.64}$$

$$\rho_{\text{vap}} = 2 \times 10^{-40}\, T^{15.356} \tag{2.65}$$

$$\rho_{\text{air}} = 352.82\, T^{-1} \tag{2.66}$$

$$c_{p_{\text{liq}}} = 0.012\,T^2 - 7.615\,T + 5393.5 \tag{2.67}$$

$$c_{p_{\text{vap}}} = 9 \times 10^{-5}\,T^3 - 0.0684\,T^2 + 17.793\,T + 283.53 \tag{2.68}$$

$$c_{p_{\text{air}}} = 0.0502\,T + 991.46 \tag{2.69}$$

$$\lambda_{\text{liq}} = -7 \times 10^{-6}\,T^2 + 0.0057\,T - 0.46 \tag{2.70}$$

$$\lambda_{\text{vap}} = 0.0051\,\mathrm{e}^{0.0043\,T} \tag{2.71}$$

$$\lambda_{\text{air}} = 5 \times 10^{-12}\,T^3 - 3 \times 10^{-8}\,T^2 + 9 \times 10^{-5}\,T + 0.001 \tag{2.72}$$

The latent heat of vaporization of water was also determined as a function of temperature by fitting the data available in the literature (Cengel and Ghajar, 1998). The correlation obtained showed a good agreement for a range of temperatures between 273 K and 600 K:

$$h_{fg} = -0.0428\,T^3 + 46.394\,T^2 - 19144\,T + 5 \times 10^6 \tag{2.73}$$

To summarize, an energy balance on the liquid created an expression (Equation 2.26) for how the steady state evaporation rate was related to the energy conducted into the liquid, as well as the thermal radiation. The above section developed a system of ordinary differential equations that will, once solved, describe the conduction component, though their solution is coupled through Equation 2.26 to the radiation component that will be model in the subsequent section.

2.3 Estimating the amount of incident radiation absorbed by the droplet ($\dot{Q}_{\mathrm{rad}}$):

Up to this section, the numerical model includes all the necessary equations to solve the proposed problem, except one equation to estimate the radiation that is absorbed by the liquid phase of the droplet. The derivation of such an expression is dependent upon two factors: (i) the geometry of the problem and (ii) the properties of the involved materials across the electromagnetic spectrum. In the different geometries shown by Figure 2.2, the continuous black line circle represents the spherical droplet. Although the representation of a three-dimensional object in a two-dimensional figure represents a difficult task, a *xyz* coordinate system was introduced in the centre of the circles as a reminder of the three-dimensional nature of the geometries that are being studied. The red arrows in the figure are used to represent the direction of the radiation magnitude, $\dot{Q}''_{\mathrm{rad}}$, which is equal to the energy flux per unit area.

In the most general case of a water droplet being surrounded by a flame (*e.g.,* gas flaring devices), the droplets can be modelled as spheres that receive thermal radiation from the environment in all directions and in a broad wavelength range (*i.e.,* the infrared range extends from 700 nm to 1 mm in the electromagnetic spectrum, approximately). A first limitation of this model exists in the sense that an unknown geometry of the energy source prevents the application of existing equations in the literature to estimate the amount of heat transfer between two bodies with known geometries. The second limitation is the fact that the absorption of infrared radiation by water in the liquid phase is dependent on the wavelength of the energy; thus, a complete description of the emissive and absorptive properties is needed for the materials.

Further simplifications can be made to this case and the heat radiation source can be represented by a concentric spherical chamber that surrounds the droplet, as it can be observed in Figure 2.2(a). In this model, the geometric limitation is no longer present; however, the calculation of the absorption capacity of the liquid across the entire spectrum is still needed in order to determine the total amount of absorbed energy. Though this represents a simpler geometry, it was unclear how such a model would be validated, therefore it was decided to develop a radiation heating model based on the use of a collimated energy beam (*e.g.*, a laser), which also eliminates the complexities of having a spectrum since the energy is produced in a single wavelength.

Figure 2.2(b) shows a model where a laser beam illuminates the lower hemisphere of a droplet. In this model, the energy is produced at a constant wavelength, thus eliminating the need to calculate the absorption of infrared heat at different wavelengths and integrating numerically to obtain a final result. A remaining complexity of this geometry is related to the directional characteristics of the absorptivity. It will be demonstrated later in section 2.3.2 that the absorptivity of water droplets is dependent upon the incidence angle of the energy ray that hits the surface. It can be observed in Figure 2.2(b) that a collimated beam of energy will hit the surface of spherical droplets at different angles of incidence, thus, the absorptivity will not remain constant across the surface and a geometrical integration will be needed.

In order to remove this complexity as a first attempt to include radiation, the model shown in Figure 2.2(c) will be applied. In this model the parallel beams of the laser hit the projected area of the droplet instead of the lower hemisphere as shown in Figure 2.2(b). This simplification allows all the energy to enter the droplet surface with a 0° incidence angle between the beam and the surface's normal, thus eliminating the need of a surface integration of the absorptivity. A limitation of this approach exists when it is compared to the geometric model shown in Figure 2.2(b) because the surface area that is in contact with the energy beam in the projected area model is equal to half the surface area of the lower hemisphere model. However, it will be demonstrated that the projected area of the droplet is approximately equal to a reduced hemispherical area with an effective absorptivity higher than 98%.

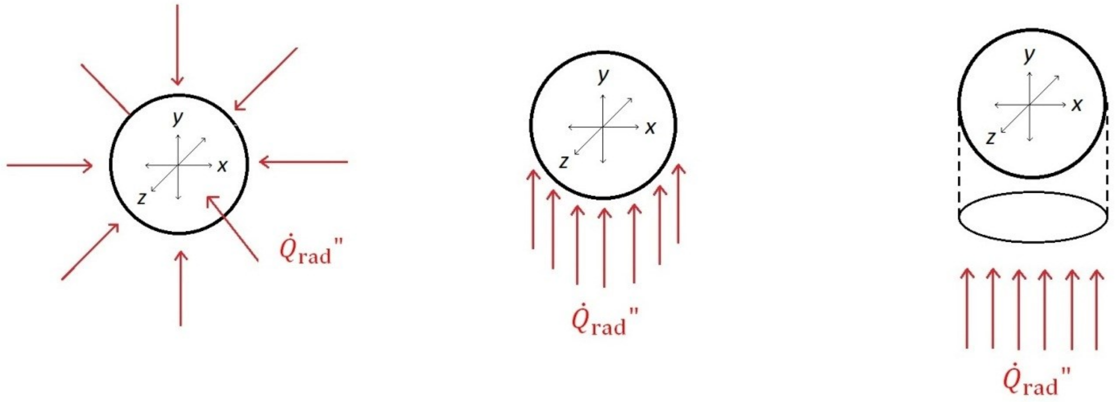

(a) (b) (c)

Figure 2.2: Different geometrical approximations used in the estimation of the total incoming heat radiation into the droplet: (a) Radiation coming from all directions; (b) Collimated energy beam hitting the droplet's lower hemisphere; (c) Collimated energy beam hitting the projected area of the droplet's hemisphere in the *x*-*z* plane.

In this section, a general description of the physics involved in the radiation heat transfer mechanism between perfect energy absorbers and emitters will be initially made. A general expression to estimate the total heat transfer between a spherical droplet and an infinite spherical chamber will be presented first. Subsequently, some simplifications will be applied to the general expression of $\dot{Q}''_{\text{rad}}$ in order to model the heat transfer of infrared heat between a laser and the droplets (*i.e.*, the model shown in Figure 2.2(c)).

2.3.1 Blackbody radiation

All materials are capable of emitting radiant energy when their bulk temperature is above zero Kelvin. The maximum energy per unit area and per unit wavelength that can be produced by a material at a certain temperature is known as blackbody radiation and it can be described by the Stefan-Boltzmann law and Plank's law. The main characteristics of a blackbody, as described by Modest (2003) and Cengel & Ghajar (1998) are: (a) a blackbody is a material that can absorb and emit the maximum possible amount of energy compared to other materials; and (b) the blackbody emits/absorbs energy in all directions and from all wavelengths. Stefan (1879) determined experimentally the expression for the maximum total energy per unit area in the whole spectrum of a surface that has a temperature T (in Kelvin). This expression was then verified theoretically by Boltzmann (1884):

$$E_{\mathrm{b}}(T) = \sigma_{SB}\, T^4 \tag{2.74}$$

where σ_{SB} is the Stefan-Boltzmann constant and equals:

$$\sigma_{SB} = 5.670 \times 10^{-8}\ \frac{\mathrm{W}}{\mathrm{m}^2\mathrm{K}^4}$$

Given the numerical nature of the droplet model, it is important to know the amount of radiative energy emitted by the energy source in each wavelength, thus, a numerical integration can be made after taking into account the spectral properties of the water. Planck (1901) derived the expression for the spectral blackbody radiation:

$$E_{\mathrm{b\eta}}(\eta, T) = \frac{C_1}{\eta^5\left[\exp\left(\frac{C_2}{\eta\, T}\right) - 1\right]} \tag{2.75}$$

where η is the wavelength of the incident radiation and the value of the constants C_1 and C_2 are, respectively:

$$C_1 = 2\,\pi\, h_p {c_0}^2 = 3.74177 \times 10^8 \ \frac{\mathrm{W\,\mu m^4}}{\mathrm{m^2}}$$

$$C_2 = \frac{h_p c_0}{k_\mathrm{B}} = 1.43878 \times 10^4 \ \mathrm{\mu m\ K}$$

The parameters h_p, k_B and c_0 represent the Planck's constant, Boltzmann's constant, and the speed of light in a vacuum, respectively. The values of the constants are:

$$h_p = 6.62606957 \times 10^{-34} \ \frac{\mathrm{m^2 kg}}{\mathrm{s}}$$

$$k_\mathrm{B} = 1.3806488 \times 10^{-23} \ \frac{\mathrm{J}}{\mathrm{K}}$$

$$c_0 = 2.99792458 \times 10^8 \ \frac{\mathrm{m}}{\mathrm{s}}$$

It is well known that Equation 2.74 is the exact solution to the integration of $E_{b\lambda}$ over the whole wavelength spectrum (*i.e.,* zero to infinity) as shown by Equation 2.76:

$$E_\mathrm{b}(T) = \int_0^\infty E_{\mathrm{b\eta}}(\eta, T)\, d\eta = \sigma_{SB}\, {T_\mathrm{b}}^4 \tag{2.76}$$

The total energy that can be absorbed by a spherical water droplet subject to radiation from a radiative heating source, can be described by Equation 2.77:

$$E(T) = \alpha\, \sigma_{SB}\, F_{21}\, A_2\, T^4{}_{\mathrm{source}} \tag{2.77}$$

where α is the absorptivity of the liquid droplet, σ_{SB} is the Stefan-Boltzmann constant, F_{21} is the fraction of energy that leaves the heat source and hits the droplet surface, and A_2 is the surface area of the energy source. It is important to remark that for an accurate application of Equation 2.77 (for the case of energy sources at a known temperature) the absorptivity is not an average value but the result of integrating numerically the absorptivity in the complete spectrum, as it will be shown later. An energy balance can be done in the liquid phase of the droplet to determine the net incoming radiation:

$$E(T) = \alpha\, \sigma_{SB}\, F_{21}\, A_2\, T^4{}_{\mathrm{source}} - \alpha\, \sigma_{SB}\, F_{12}\, A_1\, T_{\mathrm{s}}{}^4 \tag{2.78}$$

where T_{source} and T_{s} are the temperatures of the blackbody and the droplet surface, respectively. By applying the reciprocity principle, one can obtain the following expression:

$$\dot{Q}_{\mathrm{rad}} = \alpha\, \sigma_{SB}\, F_{21}\, A_2\, (T^4{}_{\mathrm{source}} - T_{\mathrm{s}}{}^4) \tag{2.79}$$

where:

$$E(T) = \dot{Q}_{\mathrm{rad}}$$

The temperature T_{s} can be neglected from the expression since the value of the temperature of the droplet surface is relatively low when it is compared with the high temperatures of blackbody energy sources, thus, an expression equivalent to the one shown by Equation 2.77 can be used to estimate the total net incoming flux of radiative heat. The temperature of the energy source must be known in order to apply Equation 2.79 in the numerical model; however, this is not possible in the case of using a laser beam. In Chapter 3 it will be shown that an experiment to determine the power distribution of a laser across the cross-sectional area of its beam is an equivalent method to obtain $\dot{Q}''_{\mathrm{rad}}$ (*i.e.,* the rate of radiative heat transfer per unit area produced by the laser, which is equivalent to the multiplication of the terms σ and $T^4{}_{\mathrm{source}}$ found in Equation 2.79). Finally, a method to determine the absorptivity of the water droplets is still needed and it will be shown in the next section.

2.3.2 Absorptivity of water droplets:

From the basic principles of optics, it is known that the total amount of energy (in the form of radiation) that hits an object of any material can be absorbed, transmitted and reflected in different proportions. The variations of these proportions depend on four main factors: The material properties (refractive index), the surface temperature (more important for metals), the wavelength of the energy wave and the angle of incidence between the incoming beam and a vector normal to the surface. In general, most agree to state that in the most general case, the sum of the absorptivity (α), the transmissivity (τ) and the reflectivity (δ) for a material at a certain temperature and wavelength can be expressed as follows (Modest, 2003):

$$\alpha + \tau + \delta = 1 \tag{2.80}$$

In Equation 2.80, each parameter represents the fraction (between 0 and 1) of the energy that is absorbed into the body, transmitted through the body, and reflected away from the surface. It is worth noting that the sum of the three parameters equals one hundred percent of the energy that comes into contact with the material.

Since not all the materials have the same characteristics, some can be classified as opaque or transparent (in terms of transmission), specular or diffuse (in terms of reflection). Opaque surfaces, unlike transparent, are those that don't let any radiation pass through a layer of material at a specific wavelength. If a surface is opaque, then $\tau = 0$, otherwise it is transparent up to a certain degree. Not all the materials that are transparent to the human eye are considered transparent since they can be opaque for radiation energy in the infrared region (Modest, 2003).

Specular surfaces are those that reflect the incident waves following the Fresnel relations. These relations are valid for flat surfaces. In the present work the assumption of a projected flat surface area of a droplet, *i.e.*, having a front face normal to incoming parallel beams will later be made in order to estimate the values of reflectivity, transmisivity and absorptivity. If a surface is diffuse, an incoming beam will be reflected in random directions rather than in a specular mode. Surface properties such as the roughness can affect the reflectivity of a material but for liquid droplets this effect can be ignored. The most important factor to be accounted for in the estimation of the reflectivity by the Fresnel equations is the complex index of refraction of the material ($m = n_{\mathrm{re}} - \mathrm{i}k_{\mathrm{im}}$).

The absorptivity of a material is the ratio between the energy that remains absorbed and the total irradiance that hits its surface. It can be proved that in general, the absorptivity is equal to the emissivity of a surface, *i.e.*, $\alpha = \varepsilon$ (Modest, 2003). Therefore, the total emissivity can be expressed by Equation 2.81 as:

$$\varepsilon = 1 - \delta - \tau \tag{2.81}$$

To estimate the emissivity of a droplet of water it is necessary to calculate the values of the transmissivity and the reflectivity of the water to apply the relation shown in Equation 2.81. The proposed method is to calculate each property by considering that the interaction between the radiation waves and the liquid droplet is similar to the interaction between light and small particles.

When an electromagnetic wave approaches a small particle, the beams can take three different paths: They can change direction as they approach the surface without touching it; this phenomenon is known as diffraction. Some beams can hit the surface and be reflected, and some can pass through the droplet and leave the material with a different angle; this phenomenon is known as refraction (Modest, 2003). Figure 2.3 shows a schematic of the different phenomena that can occur when light approaches a small particle.

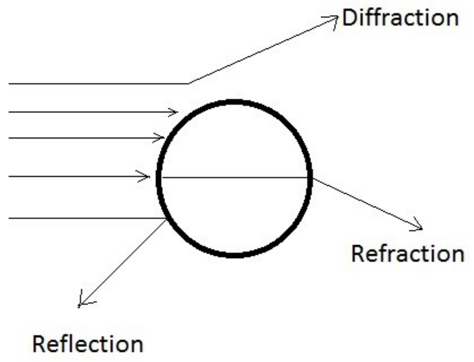

Figure 2.3: Light behavior for small particles

In general, the physics that describe the interaction between light and particles are based on three independent non-dimensional parameters (Modest, 2003):

Complex index of refraction: $m = n_{\mathrm{re}} - \mathrm{i}k_{\mathrm{im}}$

Size parameter: $x = \frac{2\,\pi\,r_{\mathrm{s}}}{\eta}$

Clearance-to-wavelength ratio: $\frac{c}{\eta}$

where:

n_{re} = Real part of the complex index of refraction

k_{im} = Imaginary part of the complex index of refraction

r_{s} = Radius of the droplet

c = Distance between droplets

η = Wavelength

The parameter $\left(\frac{c}{\eta}\right)$ can be ignored because the scope of the present research is to investigate the heat transfer in a single liquid droplet. The effect of having multiple droplets in a stream of gas is a matter of discussion in aerosols and sprays applications; nonetheless, for the case of monodisperse droplet chains applications, it can be safely assumed that the clearance-to-wavelength ratio is large enough such that the refraction, diffraction and reflection effects in one droplet do not affect the nearby droplets.

There are 3 different approaches depending on the size of the particle and the wavelength of the light involved. If the size parameter $x \ll 1$, then the *Rayleigh approximation* can be used. If $x \cong 1$, the *Mie theory* can properly describe the behavior of the light. For the case where $x \gg 1$, the particles are large enough so the behavior can be described using classic optics (Modest, 2003). For the present work, only the last approximation will be used. The Mie theory concepts and equations will be introduced and be left for future discussions.

2.3.2.1 Beer-Lambert Law:

The Beer-Lambert law describes the light absorption behavior of a liquid or gas along the complete spectrum in terms of the material properties and thickness. Let κ be the absorption coefficient of the liquid or gas material, σ the scattering coefficient (which accounts for the refraction and diffraction phenomena in the droplet), and s the distance (cm) that an electromagnetic wave penetrates into the material. As a first approximation, s is assumed to be equal to the diameter of the liquid droplet. The Beer-Lambert law states that the transmissivity, τ, can be expressed by the following exponential relation:

$$\tau = \frac{I}{I_0} = \mathrm{e}^{-(\kappa+\sigma)s} = \mathrm{e}^{-\beta s} \tag{2.82}$$

where:

I = Transmitted power

I_0 = Incident power

τ = Transmissivity

κ = Absorption coefficient

σ = Scattering coefficient

β = Extinction coefficient

Equation 2.82 implies that:

$$\beta = \kappa + \sigma \tag{2.83}$$

The expression above means that the total amount of light that is made extinct by a spherical particle is the sum of the absorbed and scattered light. This can also be expressed in terms of the scattering cross-section C_{sca} and the absorption cross-section C_{abs}, which are simply the cross-sectional areas of removed light by each phenomenon (Modest, 2003):

$$C_{\mathrm{ext}} = C_{\mathrm{sca}} + C_{\mathrm{abs}} \tag{2.84}$$

The ratios of the extinction, absorption and scattering cross-sectional areas and the actual droplet cross-sectional area are known as the *efficiency factor,* Q_{ext} :

$$Q_{\mathrm{ext}} = \frac{C_{\mathrm{ext}}}{\pi r^2} \tag{2.85}$$

$$Q_{\mathrm{abs}} = \frac{C_{\mathrm{abs}}}{\pi r^2} \tag{2.86}$$

$$Q_{\mathrm{sca}} = \frac{C_{\mathrm{sca}}}{\pi r^2} \tag{2.87}$$

where r is the radius of the particle (droplet). Therefore, Equation 2.84 can be also expressed as:

$$Q_{\mathrm{ext}} = Q_{\mathrm{sca}} + Q_{\mathrm{abs}} \tag{2.88}$$

It can be demonstrated that for large particles (*i.e.*, $x \gg 1$) the extinction efficiency tends to a constant value of approximately 2, which is known in the literature as the *extinction paradox* (Hinds, 1998). This effect exists for spheres that fulfill the condition described above ($x \gg 1$) and whose distance between them and an arbitrary point where the incident light extinction is theoretically measured is greater than $\frac{10d^2}{\eta}$. It is suggested (Modest, 2003) that the diffraction can be usually neglected in heat transfer applications and the extinction can be treated solely as transmission, hence $Q_{\mathrm{ext}} = 1$. This value means that all the possible energy that hits the surface of the liquid droplet is reflected, absorbed or transmitted.

A data set compiled by Hale and Querry (1973), in which the absorption coefficient for pure liquid water is available for a range of wavelengths of 0.2 μm – 100 μm is shown below in graphic form. Figure 2.4 shows the variation of the absorption coefficient of water in terms of the wavelength. The data was plotted on a logarithmic scale to better appreciate the water's absorption coefficient variation in the visible, near-IR and mid-IR ranges. A nearly constant κ value of approximately 1000 $\frac{1}{\mathrm{cm}}$ is observed for wavelengths above 15 μm (far-IR), while the parameter ranges considerably from a global minimum of approximately 0.0002 $\frac{1}{\mathrm{cm}}$ to a global maximum of more than 10000 $\frac{1}{\mathrm{cm}}$ between wavelengths of 0.5 μm and 3 μm.

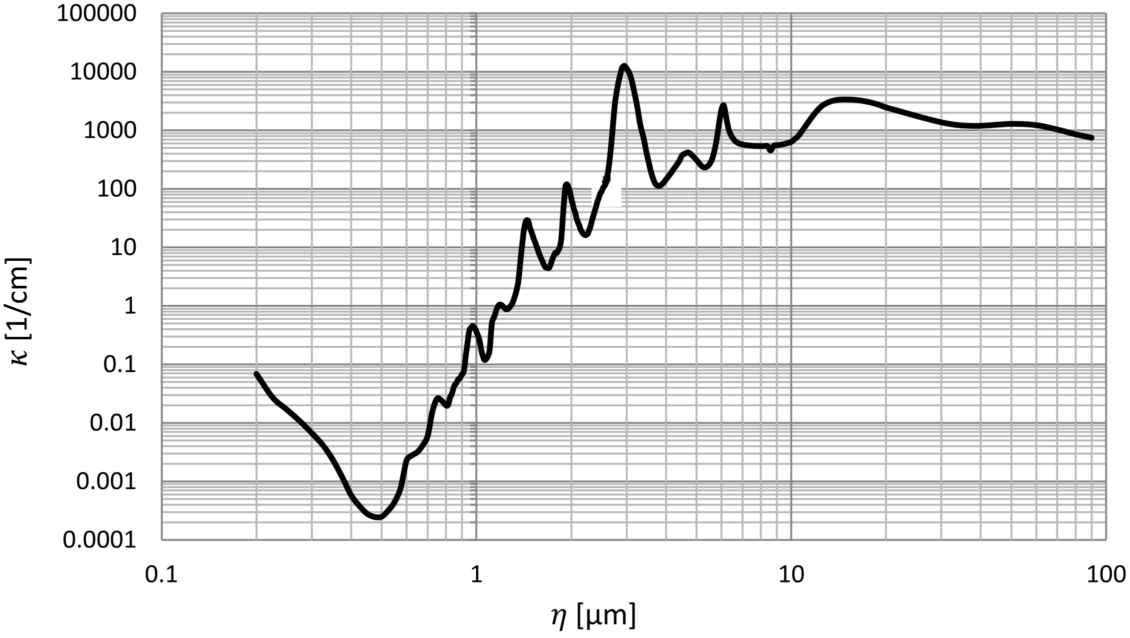

Figure 2.4: Absorption coefficient (κ) of pure water with respect to wavelength at standard temperature and pressure conditions. Graphic plotted using data obtained from Hale and Querry (1973).

Figure 2.5 shows the transmissivity with respect to wavelength obtained by applying Equation 2.82 to the data set obtained by Hale and Querry (1973), assuming that the distance that the light travels inside the liquid is equal to the diameter of an arbitrary droplet of 50 µm. This previous assumption also implies that the incidence angle between the surface normal and the incoming beam is zero. The internal reflections inside the liquid droplet can be neglected while the radius of curvature is greater than approximately 10 µm; below that value, it is believed that this assumption is no longer valid and a more complex approach should be used.

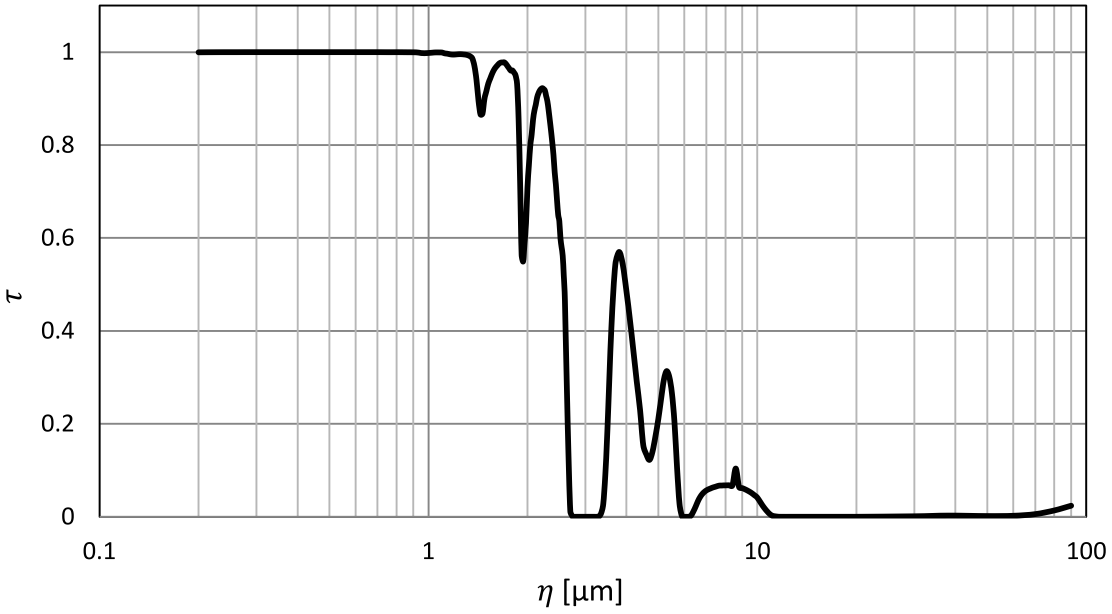

Figure 2.5: Transmissivity with respect to wavelength for a 50 µm droplet diameter. Graphic plotted using data obtained from Hale and Querry (1973).

Two different areas where the transmissivity is minimum along the spectrum can be identified. A narrow band in the proximity of the 3 µm wavelength and a wide band in the far-infrared. These two areas are consistent with the high values of the absorption coefficient shown in Figure 2.4 at the same spectral ranges. The transmissivity curve shown in Figure 2.5 cannot predict the absorption behavior of the water droplet alone. The effect of the reflectivity in terms of the complete spectrum must be added to obtain an estimate of the absorptivity as described by Equation 2.81.

2.3.2.2 The Fresnel relations

When an electromagnetic wave travels through a medium with an index of refraction equal to 1, such as air, and hits a surface at an angle θ with a complex refractive index $m = n_{\text{re}} - \mathrm{i}k_{\text{im}}$, the reflectivity of the parallel and perpendicularly-polarized light can be estimated using the Fresnel relations as follows (Modest, 2003):

$$\delta_{||} = \frac{(p - sin\theta\ tan\theta)^2 + q^2}{(p + sin\theta\ tan\theta)^2 + q^2}\delta_{\perp} \tag{2.89}$$

$$\delta_{\perp} = \frac{(\cos\theta - p)^2 + q^2}{(\cos\theta + p)^2 + q^2} \tag{2.90}$$

where:

$$p = \sqrt{\frac{1}{2}\left[\sqrt{({n_{\mathrm{re}}}^2 - {k_{\mathrm{im}}}^2 - sin^2\theta)^2 + 4{n_{\mathrm{re}}}^2{k_{\mathrm{im}}}^2} + \left({n_{\mathrm{re}}}^2 - {k_{\mathrm{im}}}^2 - sin^2\theta\right)\right]} \tag{2.91}$$

$$q = \sqrt{\frac{1}{2}\left[\sqrt{({n_{\mathrm{re}}}^2 - {k_{\mathrm{im}}}^2 - sin^2\theta)^2 + 4{n_{\mathrm{re}}}^2{k_{\mathrm{im}}}^2} - \left({n_{\mathrm{re}}}^2 - {k_{\mathrm{im}}}^2 - sin^2\theta\right)\right]} \tag{2.92}$$

The total reflectivity for a non-polarized energy wave can be calculated as an average:

$$\delta = \frac{\delta_{||} + \delta_{\perp}}{2} \tag{2.93}$$

The use of Equations 2.89 – 2.93 is subjected to a good estimation of the complex index of refraction of the liquid material and the selection of an incidence angle, hence, the total reflectivity will be a value calculated: (a) at a certain wavelength and (b) at a certain position in the surface of the sphere. The first case is needed in order to compare the spectral reflectivity with τ. A surface integration is needed in order to obtain a hemispherical average value of the reflectivity over the surface.

Figure 2.6 shows a data set compiled by Segelstein (1981) in which the real and imaginary parts of the complex index of refraction of water are plotted for a wide range of wavelengths varying from 0.01 µm up to 1000 µm. This range covers both the visible light and the whole infrared spectrum.

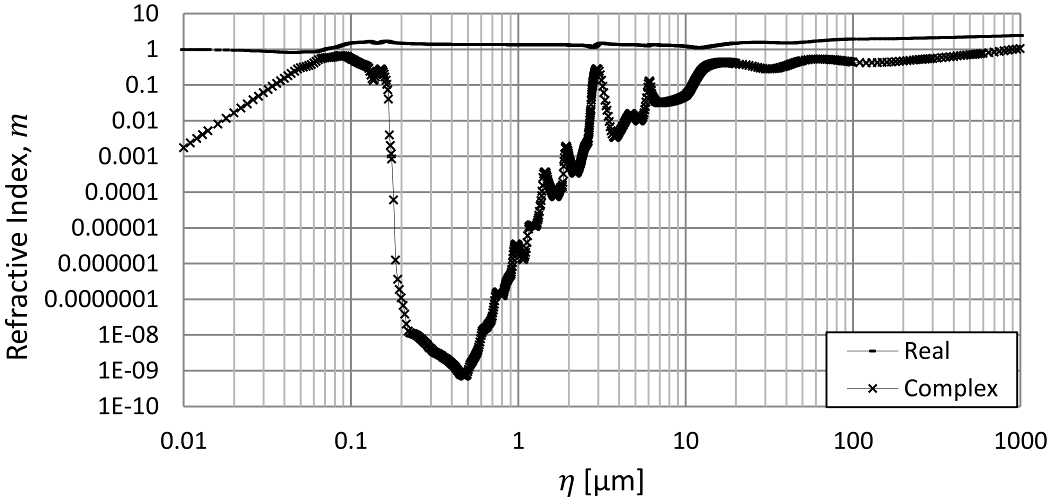

Figure 2.6: Complex index of refraction of water. Graphic plotted using data obtained from Segelstein (1981)

Figure 2.6 shows two different curves. The continuous line, which represents the real part, is nearly constant along the spectrum and has an approximate value of 1.33 within the visible band. It can be observed a global minimum of the complex part around 500 nm (blue light) resulting in the wavelength that absorbs the least amount of the visible light (*e.g.,* the blue color of the water). For practical reasons, general optics neglects the existence of the imaginary part in the visible spectrum and only assumes $m = 1.33$. This assumption is not valid for the whole spectrum as for longer and shorter wavelengths the absorption is considerable higher.

One rapid comparison between Figures 2.4 and 2.6 can conclude that the imaginary part of the complex index of refraction of water is responsible for the absorption/transmission characteristics of the material. The data shown in Figure 2.6 can be used to plot Equations 2.89 – 2.93, resulting in the curve for the spectral reflectivity of water shown in Figure 2.7. For demonstrative purposes, an angle of incidence $\theta = 0°$ was selected. A comparison of the reflectivity for different angles of incidence is shown in Figure 2.8.

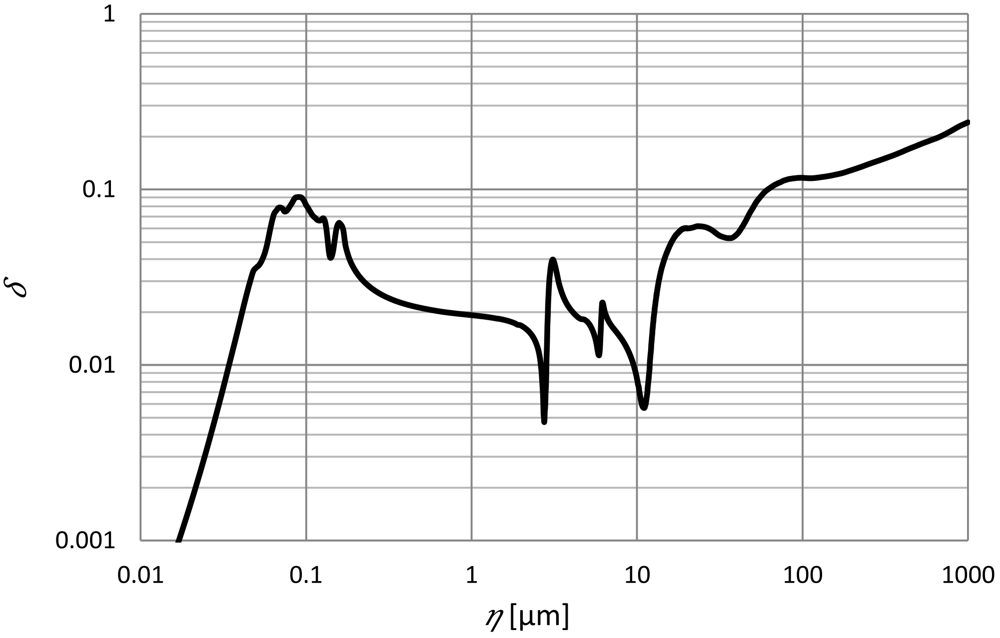

Figure 2.7: Spectral reflectivity of water with respect to wavelength for an incidence angle $= 0°$. Graphic plotted using data obtained from Segelstein (1981)

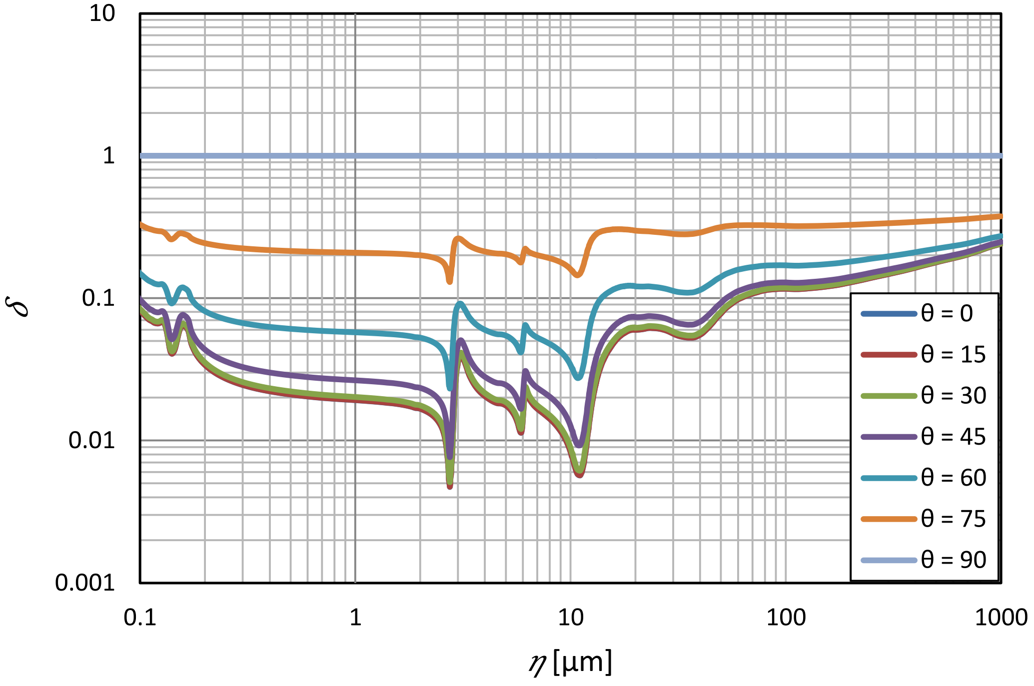

Figure 2.8: Spectral reflectivity of water for various angles of incidence. Graphic plotted using data obtained from Segelstein (1981)

It is shown in Figure 2.8 that there is a small difference in the reflectivity values for angles of incidence between 0° and 45° compared with higher angles. This difference tends to increase with higher angles up to a limit of 1 for an angle of incidence of 90° with respect to a normal surface vector. An integration of the reflectance function with respect to θ is needed in order to obtain the total spectral reflectivity. The application of Equation 2.81 using the data of δ and τ obtained in Figures 2.5 and 2.7 leads to the plot of the absorptivity (and ultimately the emissivity ε) with respect to the wavelength in the Infrared region, as shown in Figure 2.9.

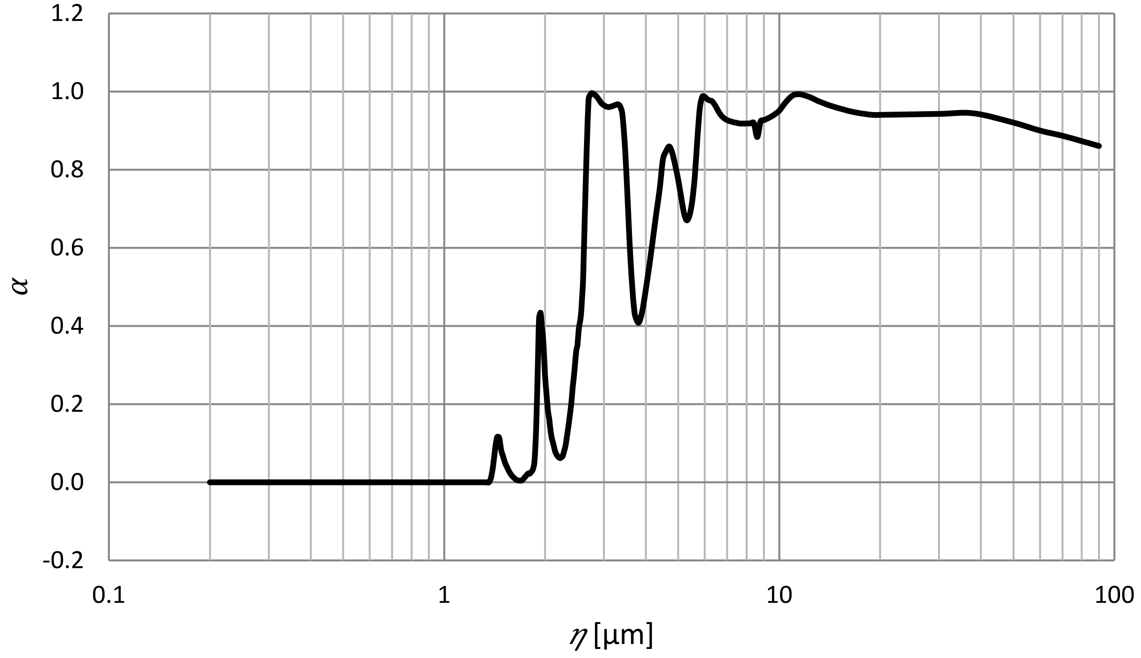

Figure 2.9: Spectral absorptivity of a water droplet (50 µm) with respect to wavelength. Graphic plotted using data obtained from Hale and Querry (1973) and Segelstein (1981)

The absorptivity plot shown in Figure 2.9 consists in several absorption bands. Six different absorption peaks can be observed at 1.92, 2.8, 3, 4.6, 5.9 and 11 µm. The most prominent absorption band is located at a wavelength of 2.8 µm. Emissive spectra from natural gas flames found in the literature also showed the existence of a high emissive peak at a wavelength of 2.8 µm (Gaydon, 1974); (Plyler & Humphreys, 1948). Other investigations, including the works by Penzias (1968), Weeks & Saunders (1958) and Tourin (1966), have also shown the emissive spectrum of pulverized coal flames, liquid fuel flames and exhaust gases from jet engines, respectively. The high amounts of emitted radiation at a wavelength of 2.8 micrometers in these investigations are due principally to the contribution of carbon dioxide and water vapor at high temperatures, and represent a significant amount of the overall power. Since the areas of interest for the current research are the near and mid infrared spectrum, the study of the spectral properties (such as the absorptivity and transmissivity) beyond the current data is out of the scope of the current research.

Although a complete numerical integration should be done across the complete spectrum to obtain the exact value of the absorptivity of water subjected to infrared radiation, experiments were performed with a laser with a single wavelength of 2.8 µm, therefore, no integration is necessary and a value of 0.95 was used. This simplification is due to the necessity of selecting a high power source to emit infrared radiation, *e.g.,* an infrared laser. An additional advantage of the calculation of the absorptivity in a single wavelength is the reduction of the complexity of the model.

Figure 2.10 shows the variation of the calculated absorptivity, α, with respect to the droplet diameter and the incidence angle of the beam. It can be observed that α is approximately constant between 10 µm and 50 µm with an approximate value of 0.99 for an incident beam of light (with respect to the droplet's surface normal) with an angle of 0°. It can also be observed that between the 0° and 60° incident angles, the value of α is greater than 0.95 for the size range between 10 µm and 50 µm. A substantial decrease in the absorptivity occurs when the incidence angle is greater than 80°. An average value of $\alpha = 0.95$ was selected for the radiation absorption calculations by assuming that most of the incident radiation absorbed by the surface of the droplet will occur with an angle between 0° and 60° with respect to the surface's normal. It is important to remark that the validity of the numerical model decreases significantly below the 10 µm diameters, as it can be observed in the figure.

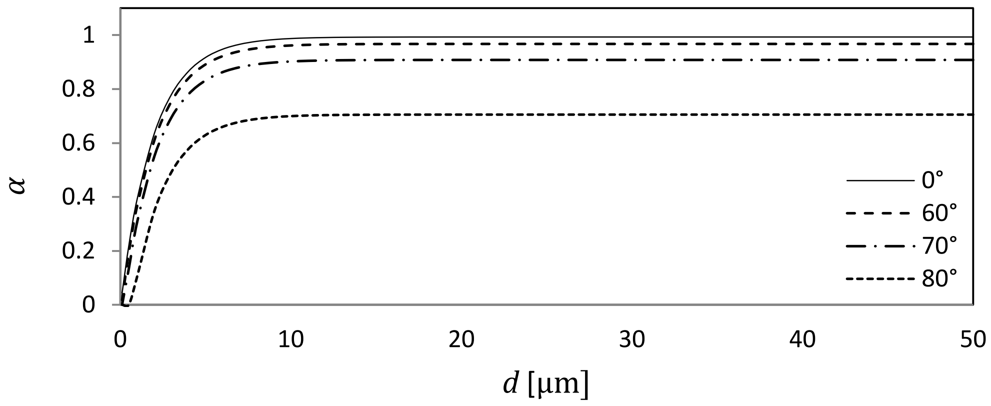

Figure 2.10: Variation of the absorptivity of water droplets with respect to the diameter and the beam's incidence angle.

Finally, a justification is given in order to apply the geometrical model described by Figure 2.2(c). Figure 2.11 shows a schematic of the lower hemisphere of the droplet that is illuminated by the laser's parallel beams. The incidence angle, θ, between any incident beam and the surface's normal is equal to the angle of the arc formed between the vertical axis of the sphere and the point of contact of the beam and the surface, as it is depicted in the figure. For a given angle of incidence, a spherical cap with a total height h is formed, and its surface area can be calculated using the following expression:

$$A_{\text{cap}} = 2\pi r h \tag{2.94}$$

After re-arranging the expression in terms of the incidence angle, θ, an equivalent expression can be obtained:

$$A_{\text{cap}} = 2\pi r^2(1 - \cos\theta) \tag{2.95}$$

It can be observed that for an angle equal to 90° the surface area of the spherical cap is equal to $2\pi r^2$, which is the well-known surface area formula of a hemisphere. Since it was determined that the absorptivity of the water droplets was higher than 95% for incidence angles below 60° and the absorptivity decreases substantially for incidence angles between 60° and 90°, it can be concluded that the area of the hemisphere that absorbs the majority of the radiation energy is the area of a spherical cap exposed to beams with an incident angle of 60° and below. After substituting an angle value of 60° into Equation 2.95, the surface area equals πr^2, which is equivalent to the projected surface area of the droplet used in the model calculations.

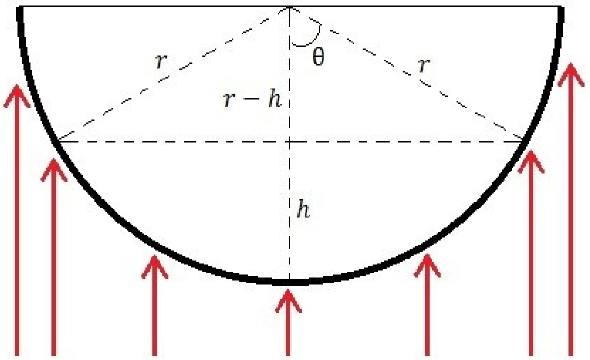

Figure 2.11: Schematic of the droplet's hemisphere subjected to incident parallel beams.

2.3.3 The view factor:

The view factor is defined as the fraction of energy that leaves one surface and hits (but not necessarily absorbed by) another surface. In the case of the radiation heat exchange between two surfaces, F_{12} is defined as the percentage of the energy that leaves surface 1, which area is denoted by A_1 and hits surface 2, which area is denoted by A_2. The percentage of energy that leaves surface 2 and hits surface 1 is denoted by F_{21}. The reciprocity principle allows calculating either F_{12} or F_{21} by applying the following expression:

$$F_{12}A_1 = F_{21}A_2 \tag{2.96}$$

In high-energy combustion applications (*e.g.*, the aerosolization and combustion of micro fuel droplets inside combustion chambers), it is often assumed that the liquid droplet is exchanging energy with an infinite, spherical chamber at an elevated temperature. In such geometry, if the area of the droplet is denoted with 1 and the area of the surroundings is denoted with 2, $F_{12} = 1$ (*i.e.*, the total amount of energy that leaves the droplet is received by the chamber), therefore the total energy emitted/absorbed by the droplet decreases with its own decreasing area as it evaporates.

2.3.4 Lorenz-Mie Theory

The use of Mie theory offers a more precise alternative to the numerical computation of the absorptivity (also called the geometric optics approximation), especially when the size parameter, x, is close to unity. Generally, the use of the geometric optics approximation requires that both the size parameter x and the product of the size parameter and the imaginary part of the index refraction ($k * x$) are much larger than the unity (Modest, 2003). Figure 2.12 shows the variation of the size parameter, x, as well as the parameter $k \times x$ with respect to the wavelength for a 50 µm spherical particle.

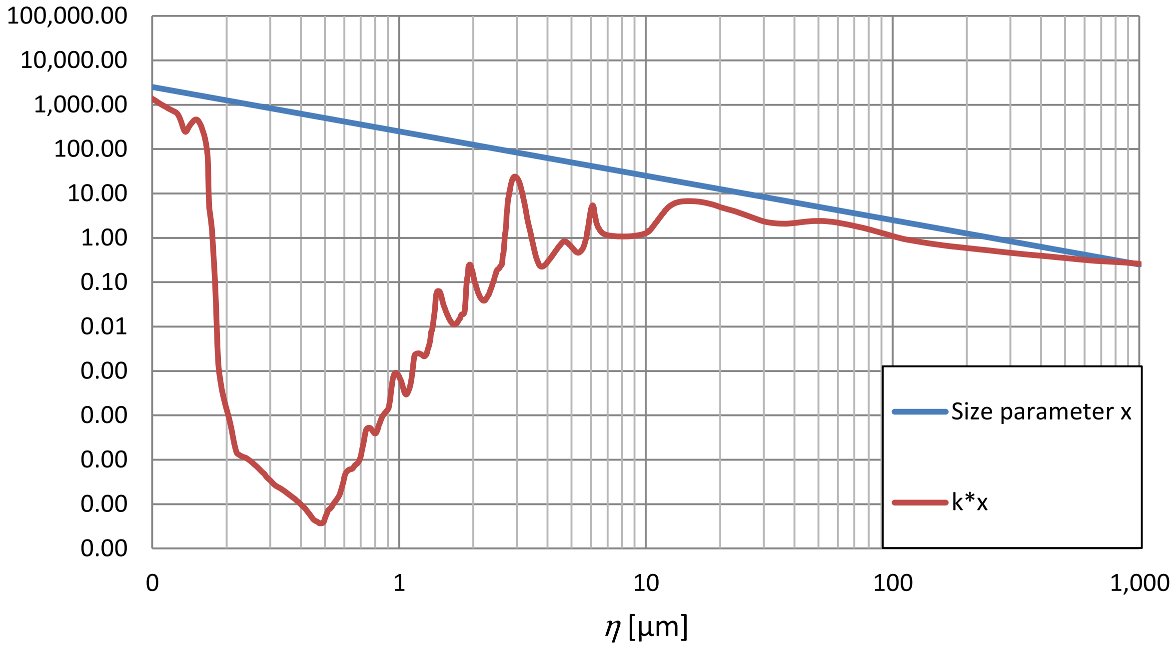

Figure 2.12: Variation of x and $k \times x$ with respect to wavelength. Graphic plotted using data obtained from Segelstein (1981)

It can be observed that the size parameter complies with the condition $x \gg 1$ for wavelengths below 20 µm; however the condition $k \times x \gg 1$ is only accomplished for wavelengths below 0.2 µm (Ultraviolet range) and in the 2.8 µm band. A value of 10 is considered as a threshold to accomplish both conditions with a low estimated error. For this reason, it is believed that the implementation of the geometric approach can be safely used to determine the optical properties in the 2.8 µm absorption band. It is important to remark that the size parameter will decrease with time as the droplet evaporates; therefore, implementing Mie theory to estimate the absorptivity may become important for small droplet diameters (1 µm – 10 µm).

Chapter 3

Experimental Set Up

Experiments were performed in the Particle Engineering Research Laboratory of the National Institute for Nanotechnology, located in the University of Alberta. An opto-mechanical experimental rig was designed to simulate various environmental conditions, including different ambient air temperatures, surrounding air flow rates, infrared (IR) radiation power and relative humidity (RH) inside a controlled area. The objective of the experimental rig was to generate water droplets and measure the droplet size with respect to time in the range between 0 µm and 50 µm subject to different environments without the addition of infrared radiation. A second set of experiments were designed for the case of an external heating source that emits infrared radiation at a specific wavelength in a collimated beam and hits the surface of the droplets in order to increase the evaporation rate.

The droplets were generated using a monodisperse droplet chain setup similar to the one described by Baldelli *et al.* (2014). Pure deionized water (#38796, Sigma-Aldrich Co. LLC.) and acetone were used as the microdroplets test fluids. Initially, air at atmospheric pressure, 0% relative humidity and room temperature (ranging between 20 °C and 25 °C) was used as the carrying gas. The humidity and temperature of air was controlled through the use of an air humidifier and an electric heater installed in the air supply system. The measurement of the droplet diameter was performed using a microscopic lens-CCD camera-light emitting diode (LED) system and applying the shadowgraphy technique. The initial size of the droplets in each experiment varied slightly due to the sensitivity of the droplet generator to changing operational conditions and fluids.

A detailed description of the rig, instruments, apparatuses and materials used to perform the experiments is given in this chapter. The calibration procedures of the image acquisition system and the laser are presented after introducing the technical specifications of their respective instruments. A description of the steps needed for the data acquisition and the image processing by the commercial software is also presented. Estimation of the uncertainties in the data is reported for an example data set in graphical form. Finally, a summary of the different environmental conditions that will be tested and presented in the results sections is given.

3.1 Experimental set up

A schematic of the experimental setup, showing the major components and subsystems is presented in Figure 3.1. The system consists of a cylindrical, borosilicate glass tube, with an internal diameter of 35 mm and a height of 400 mm that is fed from its top aperture by a stream of air at an initial temperature of 20 °C – 25 °C and atmospheric pressure, respectively. Due to varying temperature conditions of the laboratory, a constant temperature across all experiments could not be obtained; however, the temperatures were recorded for every experiment. The relative humidity of the air flow stream inside the tube was measured by locating the probe of a digital hygrometer (Humicap HM70, Vaisala Canada Inc.) in the bottom zone of the flow tube and recording the data after allowing the necessary time for stabilization of the instrument readings. On stabilization of the air flow stream coming from the laboratory compressed air system, at laboratory conditions of temperature and pressure, the relative humidity was measured and reported to be less than 1% with an uncertainty of ± 2%

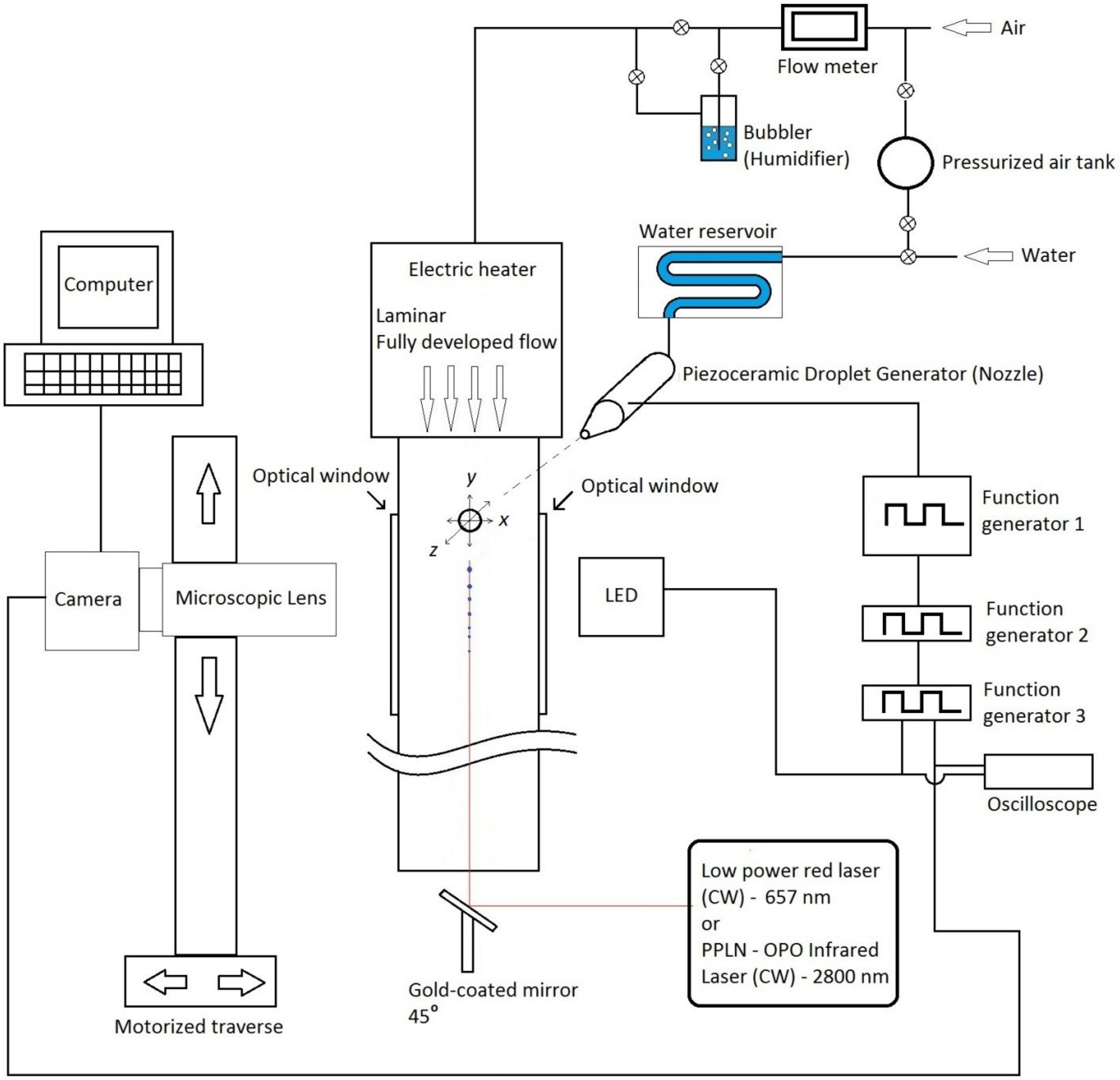

Figure 3.1: Schematic of the experimental set up

In the flow tube shown in Figure 3.1 two flat, optical grade glass windows, with a length of 100 mm and a width of 10 mm, were located parallel to each other to allow the visualization of the droplets without concerns of the refractive effects of glass tube curvature. The volumetric flow rate of air was controlled manually by a set of precision needle valves (B-1KS4, Swagelok Inc.) and measured by a digital flow meter (4000 Series, TSI Inc.), respectively. Three different volumetric flow rates were tested in order to determine the optimum condition for droplet visualization, constant distribution of the air temperature and humidity in the flow tube, and to assure a laminar flow, as it will be shown later in this chapter. A volumetric flow rate of 1 liter per minute (1 LPM ± 0.1 LPM) was chosen to perform the experiments. The calculated Reynolds number associated with the air flow at this volumetric flow rate inside the cylindrical flow tube was $Re_{\mathrm{i}} = 39$. The subscript "i" was used in the present case to represent an internal flow in a cylindrical pipe or tube. The Reynolds number was calculated using the following general definition:

$$Re = \frac{\rho\, v\, D_H}{\mu} \tag{3.1}$$

where D_H is the characteristic length of the flow tube. In the present work the characteristic length used is the internal diameter of the tube, which is also known as the hydraulic diameter. The velocity of the air, v, is the average velocity obtained by dividing the volumetric flow rate by the cross-sectional area of the tube. The density and viscosity of the air, ρ and μ, respectively, were obtained in the property tables shown in Appendix B at an average air temperature of 22.5 °C.

The air was passed through a custom-built humidifying system (bubbler), as shown in Figure 3.1, to achieve variable values of relative humidity prior to entering the vertical flow tube. The bubbler consists of a sealed glass container with two different tubes: a stainless steel tube submerged in pure deionized water (input) and a second stainless steel tube above the water level used to collect the humid air (output). A simple bypass system shown in Figure 3.1 was implemented and various values of relative humidity (up to 90% ± 2%) were obtained. The deionized water used to provide the system with the required humidity was the same water used to generate the microdroplets (#38796, Sigma-Aldrich Co. LLC.). The temperature of the water used to produce the droplets and the water inside the bubbler was not controlled but was in equilibrium with the ambient temperature of the laboratory.

An electric heater, as shown in Figure 3.1, was located above the flow tube for the achievement of various flow gas temperatures required for the different experiments. Once a desirable value was selected, the heater temperature was controlled automatically by a control system (Digi-Sense, Cole-Parmer Canada Inc.) that received the readings of a Type-K thermocouple (TFE-K-20, Omega Engineering Inc.) located at the same level of the droplet generator tip.

The droplet generation section shown in Figure 3.1 consists of a glass capillary tube with an orifice diameter of 30µm surrounded by a piezo-ceramic element (MJ-AL-01-030, Microfab Technologies Inc.). The electrical signal needed to activate/trigger the piezo-ceramic component was produced by a driver shown as "function generator 1″ in the figure (Model MD-E-3000, Microdrop Technologies GmbH). The function generator produces a square-wave signal in which three parameters can be tuned: voltage, frequency and pulse width. Voltage control determines the amplitude of the signal and thus the strength which is applied to contract the piezo-ceramic component to generate each droplet. Frequency determines how many droplets are being generated per second, and finally, the pulse width determines the period of time that the voltage will be applied to the piezo-ceramic. The initial diameter of the produced droplets was in the range of 45 µm - 50 µm with a Gaussian size distribution. The droplet generator device was inserted into the flow tube through a lateral orifice such that the device axis was oriented perpendicularly with respect to the flow tube axis and its projected distance intersected the vertical axis of the flow tube, as shown in Figure 3.1. A dual axis goniometer stage (Model GN2, Thorlabs Inc.) and a single-axis translation stage (Model PT1, Thorlabs Inc.) were used to vary the position of the tip of the droplet generator in the *x*, *y* and *z* coordinates, respectively. The liquid was fed into the droplet generator device by filling an s-shaped glass reservoir (total volume of 2 ml) with the aid of a polyethylene syringe (Luer fitting model, Fisher Scientific Company). Prior to filling the reservoir, the testing fluids passed through two 0.2 µm PTFE filters (Model 09-754-28, Fisher Scientific) to remove any solids that could potentially obstruct the capillary tube of the dispensing device. The initial impulsive pressure needed to generate the droplets was achieved by a pressurized air tank connected to the reservoir. The air pressure of the tank was maintained below 20 MPa to avoid damage to the glass reservoir and the dispensing glass tip.

Since the droplet generator is introduced into the flow tube perpendicularly with respect to the air stream, it was necessary to determine if this could affect the flow pattern, thus, creating turbulence downstream that could potentially affect the vertical path of the droplets. After applying the general definition given by Equation 3.1 to a flow stream of air around a cylinder with a diameter of 3.9 mm (*i.e.,* the diameter of the droplet generator is considered to be the hydraulic diameter D_H in the expression given by Equation 3.1), the Reynolds number obtained was $Re_{\mathrm{e}} = 4$. In this case, the subscript "e" was used to represent the external flow around an object. The properties of air and the volumetric flow rate used to calculate Re_{e} were the same as the ones used to calculate Re_{i}. At this value of the Reynolds number, a separation of the fluid from the cylindrical object will begin but it is still not sufficient to create a von Karman vortex sheet, which is estimated by the literature to be generated at $Re_{\mathrm{e}} \cong 90$ (Tritton, 1959). Therefore, the potential disturbances in the air flow caused by the droplet generator were neglected.

The electrical signal generated by the function generator 1 was also used to trigger a low voltage signal in "function generator 2" (Model 4001, Global Specialties), which was used as an intermediate control unit to vary the pulse width and the pulse spacing of the main signal. The output of the function generator 2 served as an input signal to activate a third function generator (Model 575, Berkeley Nucleonics Corporation). The two different signals coming from the "function generator 3" were used to activate a 2/3" CCD color camera (Model BB-500 GE, JAI Ltd.) and a strobe light (Model M530L3, Thorlabs Inc.) in trigger mode, respectively, at the same frequency of the droplet dispensing device. A variable delay (as low as 1 nanosecond) and variable pulse width between the main generator signal and the camera's and strobe light's signals allows the illumination and instant "freezing" of the droplets to record the images in different positions along the vertical flow tube. An oscilloscope (Model TDS 30143, Tektronix

Inc.) was connected in parallel to the main signal and the signals of the camera and the LED in order to visualize the phase difference between them.

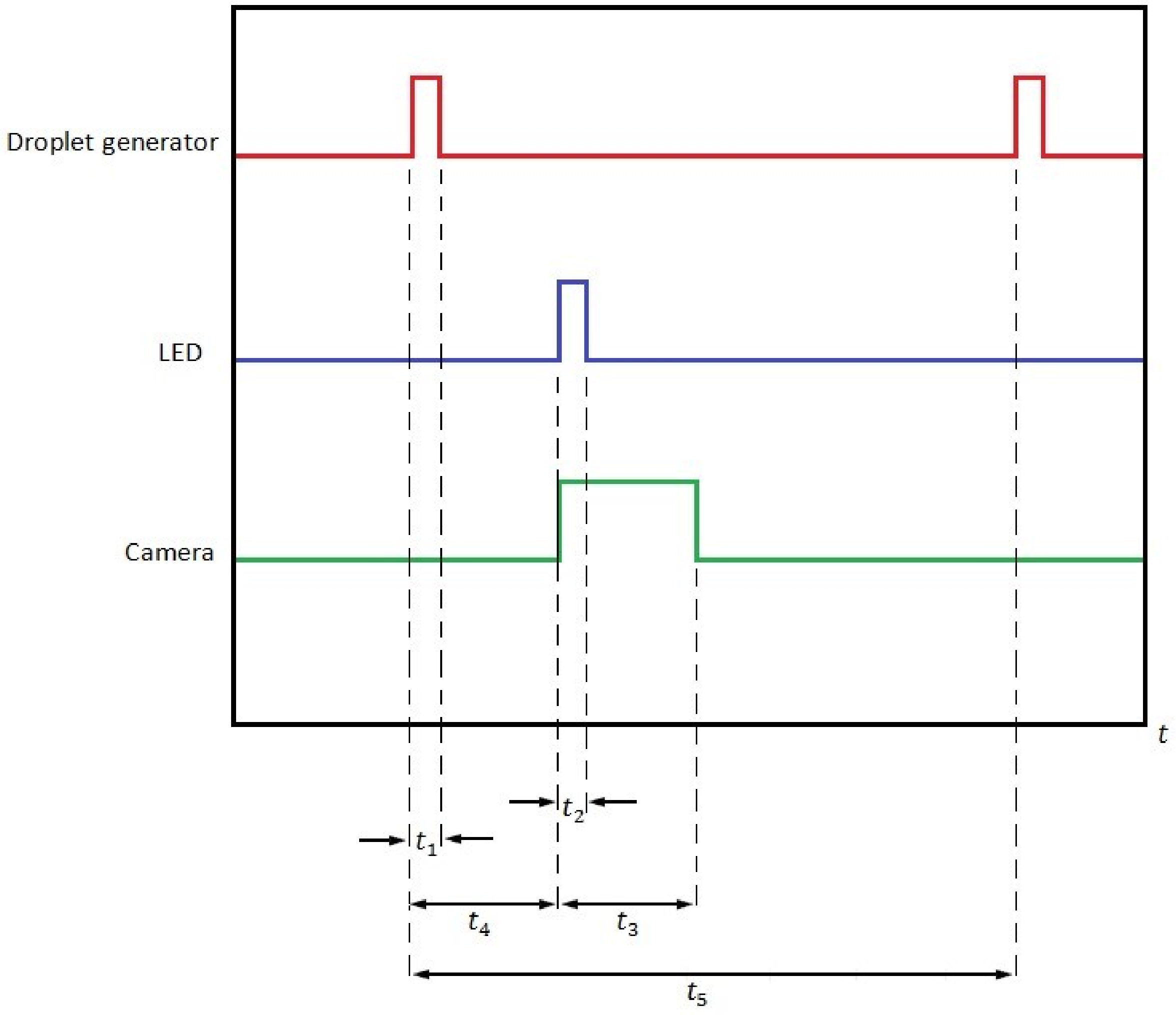

Figure 3.2: Timing diagram of the droplet generator, LED and camera signals

Figure 3.2 shows a timing diagram of the electrical signals used to activate the droplet dispensing unit, the camera and the stroboscope light. In the figure, the red, blue and green step functions are used to represent the droplet generator, stroboscopic light (LED), and the camera signals, respectively. The pulse width of each signal is represented in the figure by the times t_1, t_2, and t_3. The pulse width of the camera signal (t_3) is equal to the time the sensor becomes exposed to the incoming light, also called the exposure time. The pulse width of the stroboscopic light (t_2) was determined experimentally since at short times the sensor did not receive enough photons for good contrast images and at long pulse times the droplet was perceived as an elongated shadow due to its vertical movement within the exposure time. In order to obtain a "freezing" effect of the droplet in the field of view, t_2 was calculated as the time that the droplet must spend travelling a distance S with its total velocity v_{tot}:

$$t_2 = \frac{S}{v_{\text{tot}}} \tag{3.2}$$

In Equation 3.2, S represents the maximum distance that a droplet is allowed to travel during the image acquisition process for the purpose of obtaining images of steady shadows (*i.e.*, circular shapes rather than elongated) and thus decrease the uncertainty of the measurement technique, as it will be demonstrated later. A distance of $S = 0.5$ µm was selected to perform the calculations since it is equal to the distance of 1 pixel (the minimum discernible unit by the sensor) in the field of view, as it will be shown in section 3.1.3.1, where the pixel-to-physical space calibration is performed. The total velocity of the droplet in the air flow stream relative to a fixed observer in the system (*e.g.*, the origin of the coordinate system shown in Figure 3.1) is equal to the sum of the velocity of the air plus the droplet terminal velocity, also known as the settling velocity in the literature:

$$v_{\text{tot}} = v_{\text{ter}} + v_{\text{air}} \tag{3.3}$$

The velocity of the air stream, v_{air}, was assumed to be the average velocity of a stream of air with a volumetric flow rate of 1 liter per minute flowing through a cylindrical pipe with an internal diameter of 35 mm. An average air velocity $v_{\mathrm{air}} = 0.0173\,\frac{\mathrm{m}}{s}$ was obtained. The terminal velocity of the droplets was determined using an expression derived from Stokes' law after assuming that the droplets were in the Stokes regime (*i.e.*, $Re_{\mathrm{d}} \leq 1$) of particles with linear motion immersed in steady flows (Hinds, 1998):

$$v_{\mathrm{ter}} = \frac{(\rho_{\mathrm{d}} - \rho_{\mathrm{air}})\, d^2 \mathrm{g}}{18\, \mu_{\mathrm{air}}} \tag{3.4}$$

where ρ_{d} and ρ_{air} are the densities of the droplet and the surrounding air, respectively; d is the droplet diameter, g is the acceleration of gravity (approximately 9.8 meters per second squared for all the calculations in this work), and μ_{air} is the viscosity of the air. The properties of the water and air were evaluated at standard pressure and temperature of 1 atm and 20 °C, respectively. A value of $v_{\mathrm{ter}} = 0.0743\,\frac{\mathrm{m}}{s}$ was obtained for the case of falling droplets with a diameter of 50 µm. For smaller droplets, the terminal velocity decreases with the square of the diameter, as it can be observed in Equation 3.4. A droplet diameter of 50 µm was used in the calculations since a higher terminal velocity would result in a more conservative estimation of the time t_2. After calculating the terminal velocity, the Reynolds number of the droplet was determined in order to verify the initial assumption of droplets falling in the Stokes regime:

$$Re_{\mathrm{d}} = \frac{\rho_{\mathrm{air}}\, v_{\mathrm{ter}}\, d}{\mu_{\mathrm{air}}} \tag{3.5}$$

Equation 3.5 shows a similar expression as the definition shown by Equation 3.1. In the case of flow around a spherical liquid droplet, the characteristic length (hydraulic diameter) is replaced by the droplet diameter, d. The terminal velocity, v_{ter}, is assumed to be equal to the relative velocity between the air and the surface of the droplet since it was assumed that the droplets are carried by the flowing air stream. The value of the calculated Reynolds number of the droplets with a diameter of 50 µm was $Re_{\mathrm{d}} = 0.25$, hence the terminal velocity can be calculated safely using Equation 3.4 and the total droplet velocity was calculated as $v_{\mathrm{tot}} = 0.0916\frac{\mathrm{m}}{s}$. Finally, after substituting the calculated velocity and the distance of 1 pixel into Equation 3.2 the estimated time of the light pulse was determined to be 5.46 µs. In other words, the pulse width of the LED has to be set to a value equal or less than 5.46 µs in the function generator in order to obtain droplet images without motion. An alternative approach for the image acquisition process is to maintain a constant illumination of the LED and set the exposure time of the camera equal or less to a time of 5.46 µs.

The time t_4 represents the delay time between the instant when the droplets emerged from the nozzle and the instant that both the LED and the sensor (and the droplets) flashed and became exposed to light, respectively. A variable delay time permitted the visualization of the droplets at different vertical positions across the flow tube, thus, it is the main timing parameter in the experimental results (*i.e.*, the delay time appears as the time variable in the experimental results plots). Finally, t_5 represents the frequency of the droplet generator, which was set to 1Hz for the experiments. This frequency was selected to ensure that each produced droplet was located at a distance sufficiently far from its neighbors above and below with respect to its own position in the droplet chain, thus there was no interaction between them and the measured droplet could be safely considered isolated. This is an important assumption that was introduced and discussed in Chapter 2. An additional advantage of this approach was the reduction of the amount of water droplets in the vertical path of the infrared laser beam in the IR heating scenarios (discussed later); thus, each droplet absorbed a higher amount of infrared radiation and did not “block” the energy for the droplets located on top.

A motorized vertical traverse (Model BiSlide, Velmex Inc.) was used to hold and transport in the vertical *y*-direction, the CCD camera and LED as shown in Figure 3.1. The movement of the traverse was achieved through built-in software that allows the user to control the vertical position in a computer terminal. The minimum displacement of the stepping motor was 0.00025 inches per step. The movement of the camera in the *x* and *z* directions was performed manually by adjusting two different linear manual stages (Model LT1, Thorlabs Inc.).

Droplet visualization was achieved by connecting the CCD camera to a microscopic lens (Model 12x Zoom, Navitar Inc.). The lens allows the magnification of the image produced by the back illumination of the liquid droplets using the LED (shadowgraphy). The image collected in the sensor consists of a bright field of view with the exception of the area where the droplets or particles are located, in which no intensities of light (shadows) are recorded by the sensor. Real time visualization of the droplets was possible by using the camera’s built-in software (Jai Vision Software). Image processing, including particle recognition and diameter calculations was made using commercial software (DaVis 8.1.4, LaVision GmbH) and it will be discussed in detail later in this chapter.

A continuous wave (CW), diode laser light (Model SNF Lasiris, Coherent Inc.) with a wavelength of 657 nm and a power output of 500 mW was generated and reflected upwards from the bottom aperture of the flow tube using a gold coated mirror (Model NB1-L01, Thorlabs Inc.) in order to illuminate the droplet chain and visually ensure that it is stable and located in the central axis of the tube. The droplet chain position can be modified by adjusting the different mechanical stages and goniometers described previously. Once the droplet chain was in the desired position in the flow tube, the diode laser light was no longer needed and turned off.

A periodically-poled lithium niobate (PPLN) optical parametric oscillator (OPO) CW laser at a wavelength of 2800 nm was reflected upwards by the gold-coated mirror for the case of experiments with IR heat addition. A gold coated mirror was selected due to the high reflectance properties, *i.e.*, approximately 95% of reflectance at the specified wavelength of operation of the infrared laser. The reflective efficiency of the gold-coated mirror (0.95) was included in the estimation of the total infrared energy produced by the laser.

3.1.1 Micro droplet generator system

The dispensing device used to generate the droplets consists of 3 main components: An external housing, a piezo-ceramic component and an inner capillary glass tube. The housing material is made of commercial grade stainless steel and it has a Luer-type fitting that allows the connection of plastic tubing of several different sizes by using the appropriate Luer-tubing adapter. A 5 µm stainless steel mesh filter is inserted into the housing structure to avoid the accumulation of debris and other impurities inside the capillary tube. The mesh is sealed in the stainless steel housing by an ethylene propylene diene monomer (EPDM) O-ring seal. Two different fluids were used in the experiments: pure deionized water and acetone (99% purity). The housing and capillary tubing materials offered high resistance for both substances, although higher voltages and pulse width values were needed to produce acetone droplets due to its low surface tension at room temperature when compared to water. Figure 3.3 shows the droplet dispensing device used to perform the experiments.

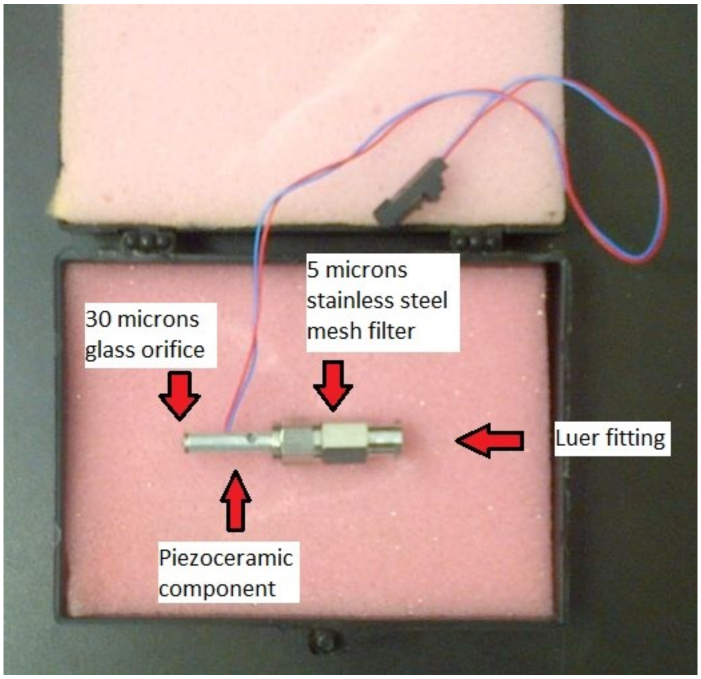

Figure 3.3: Piezoelectric droplet dispensing device

The initial diameter of the droplets generated by the nozzle is dependent on the pulse width selected in the signal generator and the properties of the liquid being used. The two material properties that influence the initial diameter are the surface tension and the viscosity. In all the experiments performed, a constant pulse width of 40 µs was selected. For water, two different experiments were performed at low and high relative humidity (1% and 90%, respectively) for a period of time of 2.5 hours and a droplet generation frequency of 1Hz in order to measure the consistency of the initial droplet diameter with respect to time. Average values of 47 µm and 50 µm for the low and high RH cases were obtained, respectively, with a variability of approximately ± 1 µm. The results of these experiments are shown in Appendix D.

3.1.2 Infrared energy source

In the spectroscopy section of the model development chapter (sections 2.3.1, 2.3.2 and 2.3.3 from Chapter 2) it was discussed that a laser beam could be used as the source of infrared energy since it can generate high power parallel beams at a constant wavelength, hence simplifying the calculation of the total absorbed heat across the entire spectrum. In the model, different peak absorption bands of water were determined and 2800 nm was proposed as the necessary wavelength of a laser to be used as a source of infrared heat. A Lockheed Martin Aculight's Argos, model SF-15, periodically-poled Lithium Niobate, optical parametric oscillator, continuous wave (CW) laser beam at a wavelength of 2800 nm (2.8 µm) was used as the source of infrared radiation to perform the experiments. The apparatus consists of three different components: a pump laser, the optical parametric oscillator (OPO) module and the control unit. A view of the three main components of the laser is shown by Figure 3.4:

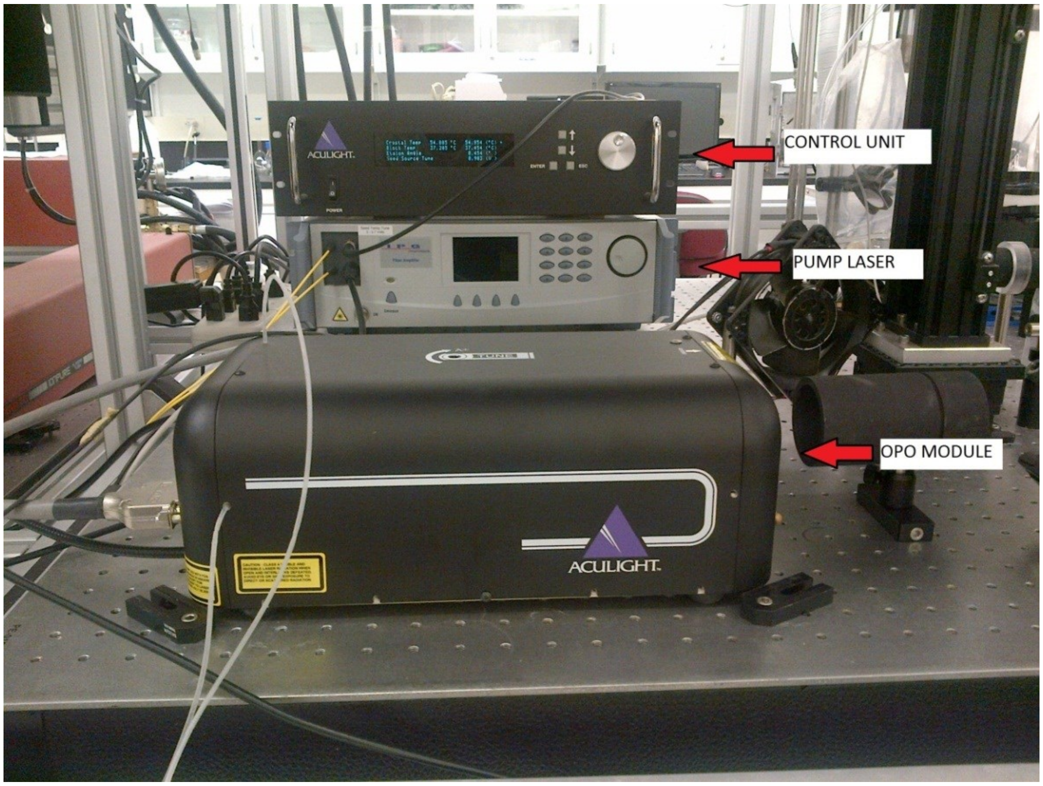

Figure 3.4: View of the main components of the infrared laser

The pump source consists of a distributed feedback fiber laser (DFB) with low power that operates at a wavelength of 1064 nm. The produced signal is then passed through a 15 W fiber amplifier and connected to the OPO module using a fiber cable with a collimator lens at the end. The OPO module consists of a sealed cavity in which the nonlinear element used is a magnesium-doped periodically poled lithium niobate crystal (MgO:PPLN). Three different beam outputs can be obtained from the head: the “pump” and “idler”, which exit the cavity on a single pass, and the “signal”, which is resonant in the cavity. The “idler” and “signal” beams exit the module at longer wavelengths than the “pump” beam. Four different modules are available to cover a wide range of the mid-IR spectrum. For the present work, module B was selected, which range of operation covers wavelengths from 1.60 µm to 1.85µm for the “signal” beam and from 2.5 µm to 3.2µm for the “idler”.

A control unit is used to control the temperatures of the cavity block and the crystal of the OPO module. It also controls the voltage values of the galvanometer and the etalon angle inside the cavity needed for intermediate-level tuning of the wavelength via angle adjustment. “Coarse” and “fine” wavelength adjustment can also be achieved by translating the MgO:PPLN crystal in the OPO module and by applying strain to the DBF fiber in the pump, respectively.

The maximum capacity power of the pump laser unit is 15 W. After turning the laser on, this value was achieved by increasing the power knob with increments of 3 W and a waiting time of 30 seconds between each increment. At this point, a warming period of approximately 1 hour is needed for the beam stability. For a maximum pump power of 15 W, a maximum idler beam (*i.e.,* the beam with a wavelength of 2800 nm) power of 2.5 W was obtained.

3.1.2.1 Laser calibration procedure

A manual tuning process was performed in the OPO module to set the wavelength of the idler beam to the desired value of 2.8 μm. This is the band that accounts for the maximum absorptivity of the water droplets, as it was determined in section 2.3.2 after the corresponding geometrical simplifications. Figure 3.5 shows a top view schematic of the calibration components that were used. The process consisted of turning a screw located on top of the OPO module or “head” with a special screwdriver until the desired wavelength was achieved. The adjustment of the “tune” screw allows the precise movement of the crystal inside the cavity of the head, hence, varying the output wavelength of the beam. The wavelength was measured prior to performing the experiments using a wavelength meter (Model 621A-IR, Bristol instruments Inc.). The beam was reflected towards the meter by a barium-fluoride uncoated window, acting as a beam splitter (Model #87-701, Edmund Optics Inc.) and passed through a barium-fluoride linear polarizer (Model WP25H-B, Thorlabs Inc.) to attenuate the power intensity of the beam, as shown in Figure 3.5.

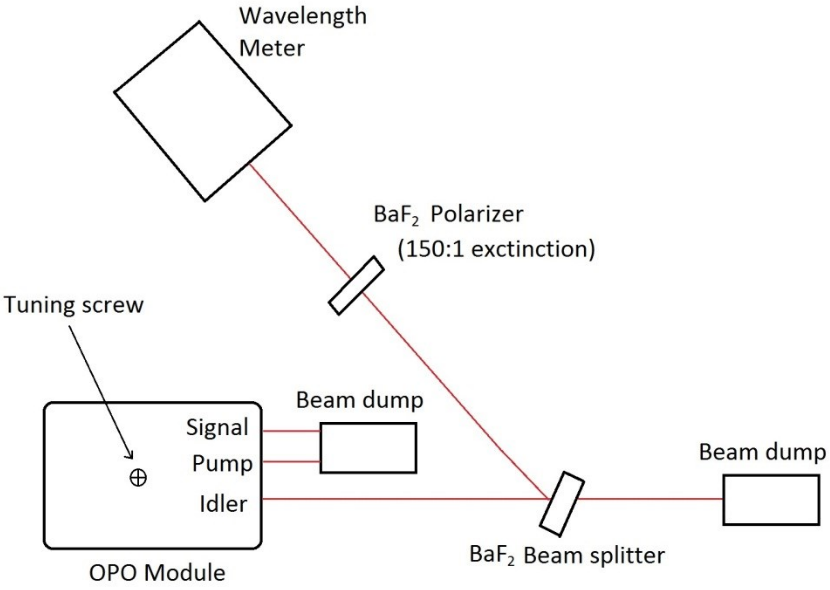

Figure 3.5: Layout schematic of the laser calibration components

Following this procedure, a wavenumber of 3571.45 cm^{-1} was obtained; this wavenumber is equivalent to a wavelength of 2.7999 µm. After all the experiments were performed, the wavenumber was measured and a value of 3571.76 cm^{-1} was reported. The second corresponds to a wavelength of 2.7997 µm. The accuracy of the wavelength meter is reported to be ± 0.0002 nm.

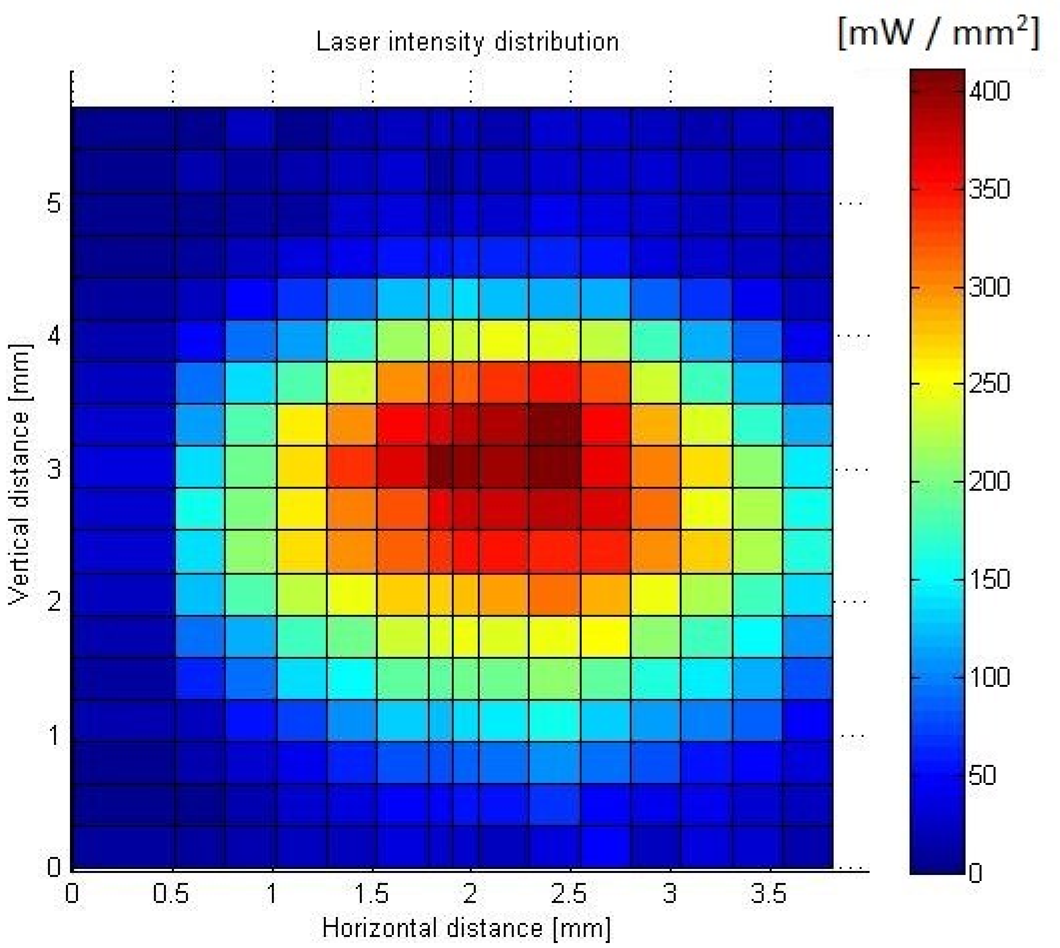

Figure 3.6: Laser beam power distribution map

Experiments to determine the profile of the laser beam and the power distribution were also performed. Figure 3.6 shows a plot of the laser power density distribution (in Watts per millimeters squared) in a 2-dimensional array, perpendicular to the laser beam. In the figure, the intersections of each horizontal and vertical line represent a data point recorded in the profiling experiment; hence the grid may not appear even. The objective of the experiment was to determine the area of the beam in which the droplets had to fall into in order to receive the maximum amount of infrared energy. From the figure it can be observed that the beam power distribution is Gaussian. Based on two different definitions used in the literature for the laser beam diameter, $1/e^2$ and the full width at half maximum (FWHM), the calculated values of the beam diameters were approximately 3.9 mm and 2.6 mm, respectively. The $1/e^2$ is the defined as the diameter of a laser beam that has 86% of the total integrated power circumscribed to its cross-sectional area, while the FWHM is the width of the Gaussian function where the value of the power is equal to half of the function's peak value. The beam diameter and the total integrated beam power are the parameters that are needed as inputs in the numerical model to determine the total incoming amount of infrared heat into the spherical droplets if the assumption of a constant power distribution is made. Alternatively, the position of the droplets in the map shown in Figure 3.6 could be used to determine the amount of power that hits the droplet surface by multiplying the density (in Watts per squared millimeter) by the projected area of the droplet; However, the knowledge of the exact position of the droplet chain with respect to the laser beam cross-sectional area would be needed in each experiment in order to determine this properly. The detailed procedure of the laser beam profiling experiments and the results are shown in Appendix E.

3.1.3 Imaging Sensor and Lens

A color charge-coupled device (CCD) camera (Model BB-500 GE, JAI Ltd.) was used to record the images. The 2/3" CCD sensor has a resolution of 2456 (horizontal) by 2058 (vertical) pixels and a shutter speed of up to 15 frames per second with full resolution in continuous mode, however, in trigger mode, the recording speed decreases considerably. The variable exposure time ranges from 64 µs to 2 seconds. The camera was connected to a computer using an ethernet cable to transfer the data between the memory and the software terminal.

The microscopic lens attached to the sensor (Navitar Inc.) has a zoom ratio of 12:1 with a dynamic magnification range of 0.07X to 583X. The working distance ranges between 32 mm and 341 mm and the field of view (FOV) ranges between 0.006 mm and 85.71mm depending on the accessories installed. The high zoom ratio can be achieved at the expense of the loss of light; therefore, due to the amount of light that the LED can emit, a zoom of 6X was achieved without compromising the contrast of the image. The images obtained were calibrated for correlating pixel space-to-physical space, as it will be shown in section 3.1.3.1. Calibrations for the image distortion due to the curvature of the lens and depth of field were not considered.

3.1.3.1 Image calibration procedure

The calibration procedure consisted of linearly correlating the space in the camera's sensor, in pixels, to physical space, in micrometers, for the given magnification of 6X. In order to do this, a multi-function high magnification calibration target (Model #56-076, Edmund Optics Inc.) was used. The target included various sets of concentric circles and grids. Figure 3.7 shows an image of the grid used to calibrate the system, which consisted of a 2.55mm x 2.55 mm square grid composed of equally spaced vertical and horizontal lines (50 µm space between the lines and 2.5 µm line width). The overall accuracy of the target is ± 1 µm.

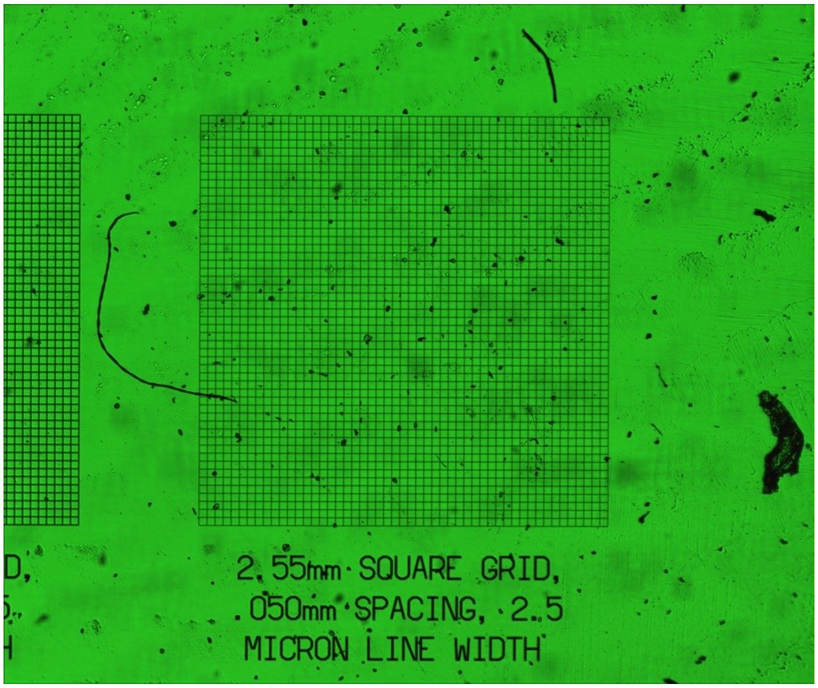

Figure 3.7: Image of the calibration target grid with low amplification

Calibration images were recorded after each experiment to minimize the uncertainties introduced by the movement of the complete optical system between experiments. To record the images, the flow tube was removed in order to place the grid in the same plane where the droplets were located (without changing the focus or position of the camera). The correct position was considered to be achieved when the grid lines were in sharp focus. After obtaining the images, the pixel-to-physical space correlation was made in the software by accessing the scaling function. A scaling factor of 0.500653 µm per pixel was obtained for all the experiments, which resulted in an image with a horizontal and vertical field of view of 1229.6 µm x 1030.34 µm.

3.2 Experiment procedure

This section offers a detailed description of the steps performed during the experiments, including: the production of microdroplets, the use of the infrared laser as a heating device, and the acquisition of the images. For simplification, only the simplest case (*i.e.*, droplets evaporating in dry, ambient temperature air) will be shown. The procedures for the addition of infrared heat, hot air, and humidity are shown in a general description since various operational conditions can be achieved.

The droplet chain was produced using the following procedure:

- The following electric systems were turned on: the three function generators, the oscilloscope, the air flow meter, the motorized traverse, and the low-power red laser.
- The pressurized air coming from the laboratory feed line was allowed to pass through the air flow meter and hence through the flow tube. The needle valves were adjusted manually in order to obtain a constant flow rate of 1 liter per minute through the system. In the case of humid air requirement, a by-pass system (as the one shown in Figure 3.1) was implemented to allow a certain amount of dry air to pass through the

bubbler. The amount of air that passed though the bubbler was controlled manually by the needle valves.

- The pressurized air feed line from the laboratory was also used to fill a pressurized air tank at a constant pressure of 15 MPa that was connected to the liquid reservoir through a quarter-turn ball valve (Model SS-4P4T-BK, Swagelok Inc.) and acted as the initial driving force to move the liquid from the reservoir towards the nozzle.
- The deionized water was manually fed into the reservoir using a Luer-type syringe until the system was completely filled with the liquid and no air bubbles were present. A quarter-turn valve was closed between the syringe and the reservoir to ensure that the liquid did not return.
- After completely filling the system, a thin, continuous stream of water would emerge from the droplet generator due to a pressure difference between the ambient and the interior of the reservoir. The stream was observed due to the illumination of the red laser beam. At that instant, the function generator 1, which is responsible for generating the main electric signal for the droplet production in the piezoceramic nozzle, was set to an initial voltage of 25 V, a frequency of 50 Hz. Finally, the droplets would emerge from the orifice of the droplet generator and hit the wall of the flow tube due to the excessive voltage.
- To create a vertical droplet chain, the voltage of the function generator 1 was reduced until the droplets did not hit the wall of the flow tube. Further control of the voltage was done to adjust the position of the vertical stream of droplets until it was visually located approximately in the central axis of the tube. The position of the chain was also varied by the goniometer and the linear stage, as described in section 3.1. The vertical chain was visualized by the illumination given by the low power red laser beam. A manual adjustment of some optical mirrors (not shown in Figure 3.1) was needed in order to locate the vertical chain with the light beam.
- The frequency of the droplet chain was decreased slowly until a frequency of 1 Hz was achieved.

The images were acquired using the following procedure:

- Once the droplet chain was produced, the following parameters were visually inspected and recorded to ensure proper settings for each experiment: nozzle frequency, gas flow rate, relative humidity, gas temperature, and position of the chain relative to the tube's axis.
- The LED and camera were turned on and set in *trigger mode* and low magnification in order to locate the first droplet in the field of view. The function generator connected to the nozzle, camera and LED was previously set to a delay time of 0.02 seconds between the nozzle signal and the camera trigger signal in order to capture an image of the first droplet along the centerline of the tube. This delay time is equivalent to the time the droplet takes to reach full vertical motion (with no horizontal velocity component) after it is produced by the nozzle.
- After the first droplet image is observed in real time, a manual adjustment of the camera position was done by moving the traverse in the vertical and horizontal directions until the droplet was located in the center of the image.
- A magnification of the image was done by "zooming in" with the microscopic lens. This step requires the light source to be located closer to the droplet chain due to the loss of light intensity caused by the magnification.
- A manual focusing of the microscopic lens was performed until a sharp "shadow" of the droplet was obtained. Another sign of optimal focus was the presence of a "bright spot" in the middle of the droplet's shadow, which represents the light that is transmitted through the liquid sphere without diffracting.
- Once a desirable number of images were recorded in one position, the delay time between the nozzle signal and the camera signal was increased and the camera was moved in the vertical direction until the next droplet appeared in the middle of the field of view.
- The process was repeated with increments of 0.02 s, 0.05 s, and 0.1 s in the delay time for the experimental cases of acetone in dry air, water subjected to infrared heat, and

water without infrared heat, respectively. The magnification of the camera was constant for all the experiments.

3.3 Measurement technique: Shadowgraphy

The use of shadowgraphy as an image-based technique for measuring particle size and shape has been used for different applications in the literature. Similar experimental setups to the one used in this study have been implemented to determine the mean diameter and the shape of liquid droplets in sprays (Simmons H. , 1977), (Oberdier, 1984), (Weiss, Derov, DeBiase, & Simmons, 1984), (Kim & Lee, 2001), (Kashdan, Shimpton, & Whybrew, 2007), and (Ghaemi, Rahimi, & Nobes, 2008); and of gas bubbles in effervescent atomization (Gomez, Fleck, Olfert, & McMillan, 2011). The technique allows the non-intrusive acquisition of images via the backlight illumination of the droplets, thus, creating a shadow pattern that coincides with the shape and size of the measured object.

The shadowgraphy technique offers some advantages when compared with other non-intrusive techniques such as the phase Doppler particle analyzer (PDPA) or forward-scattering techniques (Fraunhofer diffraction rings). Since it is an image-based technique, shadowgraphy is suitable for measuring the size and shape (centricity) of non-spherical particles whereas the PDPA and forward-scattering techniques are based on the assumption of perfectly spherical particles. However, a limitation exists for the measurement of particle size below certain limits due to uncertainties associated with the image discretization by the pixels of the sensor (Ghaemi *et al.*, 2008), and indistinct boundaries (Podczeck, Rahman, & Newton, 1999). To minimize these uncertainties, a minimum number of 40 -50 pixels across the image was proposed by Podczeck *et al.* (1999), and Ghaemi *et al.* (2008).

Figure 3.8 shows a sample image of a single droplet recorded by the camera. Image analysis was performed using commercial software (DaVis 8.1.4, LaVision GmbH). A monochromatic light emitting diode with a diffuser was used to produce the light for the back-illumination of the droplets. This type of light was chosen to reduce the chromatic aberrations caused by the variation of the refractive index of the lens at different wavelengths.

A bright “spot” can be observed in Figure 3.8 at the center of the droplet when the lens is focused and a sharp contour of the droplet shadow is achieved. This phenomenon is produced by the light beams that hit the droplet surface perpendicularly and are not refracted in a different direction. This phenomenon was used during an image pre-processing stage to manually eliminate the images that were out of focus, thus decreasing the uncertainties reported by Podczeck *et al.* (1999).

A minimum of 100 images were evaluated at each camera position in the flow tube to obtain the average droplet diameter at an acceptable uncertainty. The processing algorithm consisted of 3 steps. First, a pre-processing step was performed manually to remove all the images where no droplets were present as well as the ones where the droplet was out of the focal point of the camera. The second and third steps were performed automatically by the software after selecting the proper particle recognition and sizing parameters. In the particle recognition step, the image intensities are inverted, thus the darker pixels (shadows) appear bright and *vice versa*. After doing this, the software will recognize all the adjacent pixels that have a higher intensity than the threshold intensity selected by the user. In the present work, several particle recognition intensity levels were tested and 20% was selected as the optimum value at which the largest amount of particles were recognized, in contrast with the higher values 50% and 70% in which only some particle were recognized and no particles were recognized, respectively. Alternatively, at intensity levels lower than 20%, a considerable amount of dust and debris present in the optics were recognized as particles.

Finally, the third step consisted in measuring the diameter of the recognized particles by counting the total amount of pixels and transforming the pixel area into physical area by using a calibration correlation (physical space per pixel).

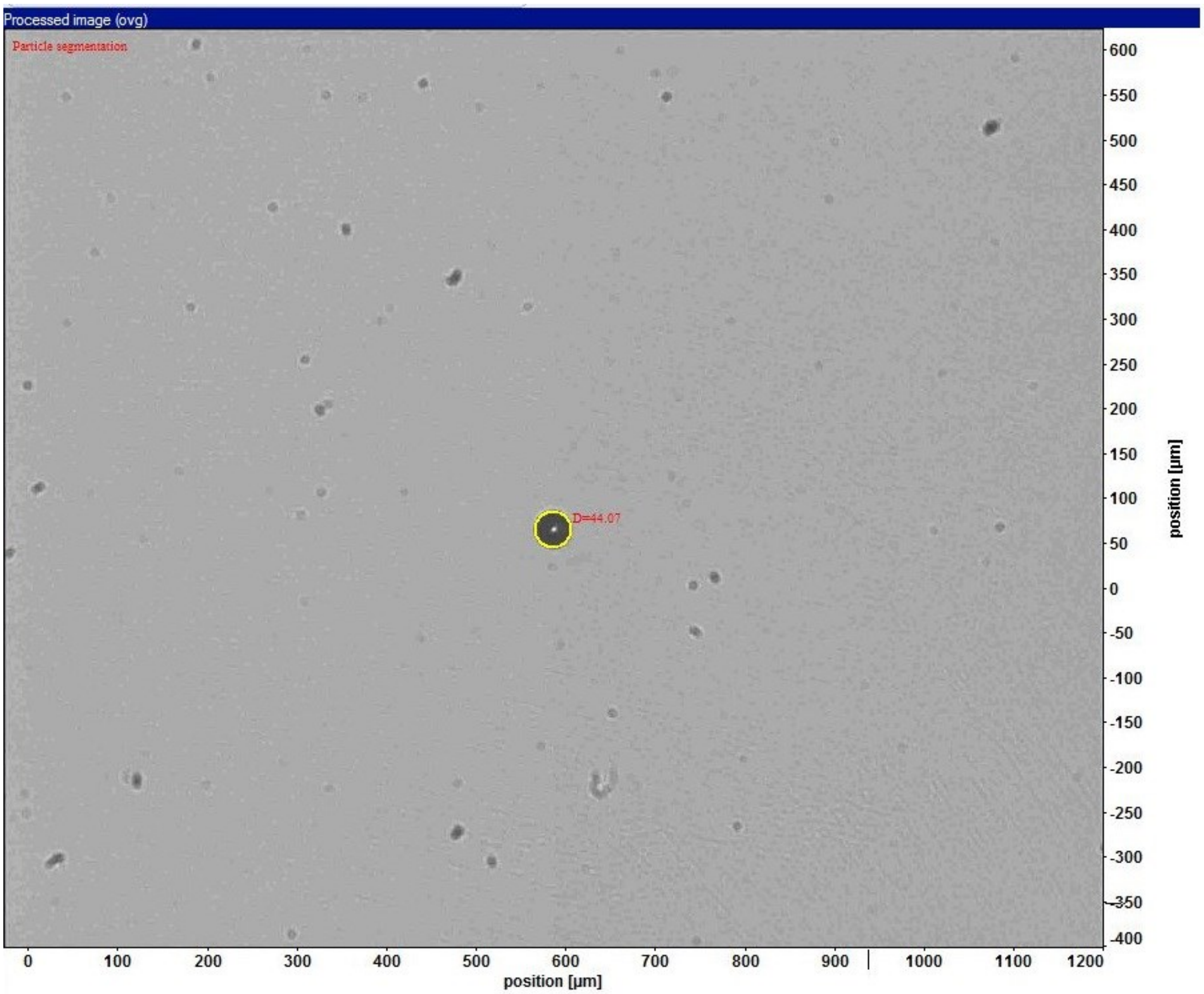

Figure 3.8: Main screen of the commercial software showing the particle recognition and sizing functions applied to the recorded image

Not all the captured images can be obtained with a sharp droplet edge. Instead, the intensities of the pixels that surround the centre will diminish as their radial position increases, thus making the decision of which pixel is counted difficult. To avoid uncertainties introduced by indistinct boundaries, the particle sizing function is divided in two steps. In the first step, the software will count the total amount of pixels that have a higher intensity than a low level threshold. In the second, the pixels that have a lower intensity than a high level threshold will be counted. In both steps, a size value will be given for each calculation and a mean value will be calculated.

Since it is evident that the droplet size will be affected by varying the low and high level parameters of the particle sizing function, a preliminary experiment is necessary to study the effect of these variations in the droplet diameter. Figure 3.9 shows the effect of varying the particle sizing parameters (*i.e.*, varying the thresholds for the low and high level pixel intensity recognition parameters of the software) in a specific data set. The results are shown in a probability distribution function N versus d, where $\bar{d}$, d, and σ_d are the droplet mean diameter, the data diameter and the standard deviation, respectively. N can be calculated using the following expression:

$$N = \frac{1}{\sigma_d \sqrt{2\pi}} \mathrm{e}^{-\frac{(d-\bar{d})^2}{2\,\sigma_d{}^2}} \tag{3.6}$$

The data set selected to perform the analysis shown corresponds to the simplest case of a water droplet chain immersed in dry air (0% relative humidity), no infrared heat radiation, frequency of 1 Hz, and room air temperature. The position of the camera in the *y*-direction with respect to the origin (as shown in Figure 3.1) was such that the recorded images correspond to droplets that have been immersed in the air stream for 0.42 seconds after they were produced by the generator. A total number of 100 images were processed for each case of pixel intensity level. The pixel-to-physical space scaling factor used was 0.500653 µm per pixel. This value was used in later calculations as the uncertainty of the camera since it is the minimum possible unit that can be measured by the sensor.

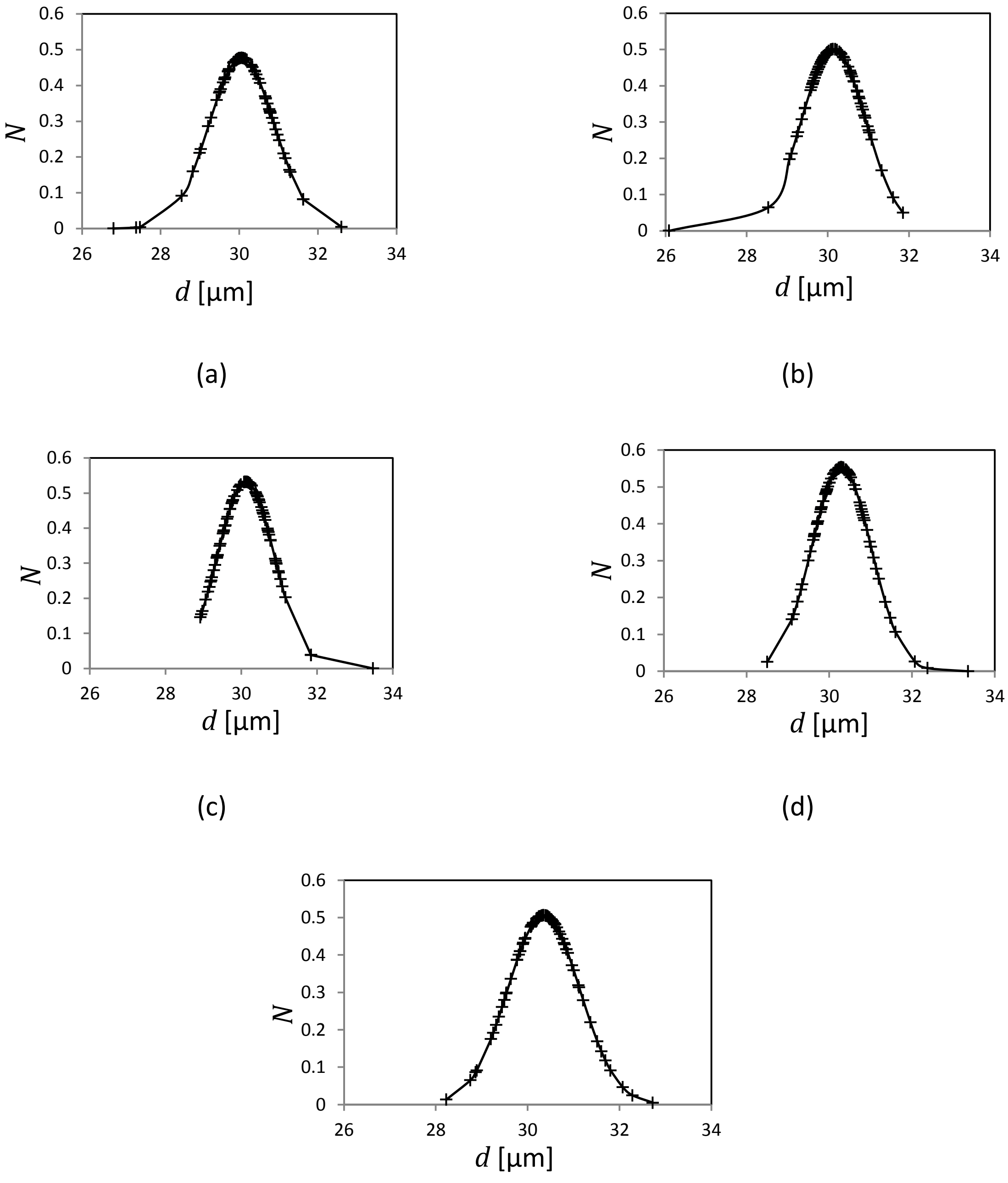

(a)

(b)

(c)

(d)

(e)

Figure 3.9: Droplet diameter probability distribution function obtained for the same data set and varying particle sizing parameters (pixel intensity levels): (a) Low level = 50% and High level = 50%; (b) Low level = 45% and High level = 55%; (c) Low level = 40% and High level = 60%; (d) Low level = 35% and High level = 65%; (e) Low level = 30% and High level = 70%

In Figure 3.9, it can be observed that the size distribution of the droplets is Gaussian for all the analyzed cases. The values of the mean diameter and the standard deviation are shown in Table 3.1. Results show little variance of the mean diameter with respect to the varying threshold parameters. It was also observed that the difference between the maximum and minimum mean value obtained was less than the averaged standard deviation for all the studied cases. In case “a”, since the low and high intensity levels are equally 50%, a unique amount of pixels is recognized by the software, thus, only one value of the droplet diameter is reported. In the rest of the cases, two different diameters are reported: one diameter corresponds to the amount of recognized pixels that have a higher intensity than the low level threshold and another diameter associated with the total amount of recognized pixels that have a lower intensity than the upper threshold. In cases ”b”, “c”, “d”, and “e”, the two different diameters calculated at low and high intensity levels are averaged and a single value will be shown for each image.

Table 3.1: Mean diameter and standard deviation for the different pixel intensity level cases shown in Figure 3.9

Pixel intensity level case	**Mean diameter ($\bar{d}$), in µm**	**Standard deviation (σ_d), in µm**
(a) Low level = 50% High level = 50%	30.059570	0.836005
(b) Low level = 45% High level = 55%	30.142335	0.796414
(c) Low level = 40% High level = 60%	30.122742	0.749350
(d) Low level = 35% High level = 65%	30.293330	0.721319
(e) Low level = 30% High level = 70%	30.351096	0.787745

3.3.1 Determination of the uncertainty in the measuring technique

The total uncertainty of the droplet diameter in all the experiments was determined by the following expression:

$$U_x = \sqrt{{P_x}^2 + {B_x}^2} \tag{3.7}$$

where U_x is the total uncertainty of the measured value, P_x represents the precision error, and B_x the bias error. The bias error was assumed to be equal to 1 pixel (0.500653 µm), since it is the minimum unit of measurement of the sensor. The precision error was calculated using the following equation:

$$P_x = z_{c/2} \frac{\sigma_d}{\sqrt{n_s}} \tag{3.8}$$

where $z_{c/2}$ is known in the literature as the z-factor for a confidence interval of c%, σ_d is the standard deviation of the sample, and n_s is the total number of images analyzed. For a confidence interval of 95%, the z-factor used was $z_{c/2} = 1.96$ (Beckwith, Maragoni, & Lienhard, 2007). The method described above was applied to the experimental data and a range of uncertainty of the droplet diameter between ± 0.5 µm and ± 0.6 µm was obtained for all the experiments. A higher value of uncertainty (approximately ±0.6µm) was obtained for the case of droplets smaller than 35 µm, due principally to the reduced amount of images captured in the lower part of the optical window, while the lower uncertainties were obtained for the droplets located above. This range of uncertainty represents approximately 3% of the droplet diameter for the case of the smallest droplets recorded in the experiments (*i.e.,* 25 µm).

3.4 Operating conditions

Several conditions of air flow, humidity, temperature and infrared radiation were tested in the experiments performed. All the experiments were performed at atmospheric pressure. Table 3.2 summarizes the ranges of the parameters tested.

Table 3.2: Operating conditions

Parameter	**Range**
Air temperature	20 °C ; 25 °C ; 60 °C ± 1.5 °C
Air volumetric flow rate	0.5 LPM ; 1 LPM ; 2 LPM ± 0.1 LPM
Relative Humidity	1% ; 30% ; 60% ; 90 % ± 2%
Total incident infrared radiation power	200 – 400 mW/mm^2

In the case of air flow rate, different values were tested in order to determine the optimal conditions of flow that satisfied the following: (a) a constant distribution of relative humidity and temperature along the flow tube; (b) an adequate residence time of the droplet inside the flow tube so visualization of size change due to evaporation could be achieved; and (c) a flow pattern that ensures the existence of a perfectly vertical droplet path without disturbances due to turbulence (*i.e.*, laminar flow). Experiments were performed using water droplets immersed in dry air (0% RH) at room temperature and volumetric flow rates of 0.5, 1 and 2 liters per minute, respectively. All the flow rates were observed to comply with condition “c”. It was observed that the volumetric air flow rate of 0.5 liters per minute had adequate residence time to visualize a substantial size change, however, the measured values of relative humidity and temperature at the bottom of the flow tube were not equal to the values measured in the upper section due to a mixing phenomenon with the surrounding air in the laboratory, thus, these parameters could no longer be considered constant. The use of a higher air volumetric flow rate (2 liters per minute) allowed a constant distribution of the relative humidity and temperature fields across the flow tube. However, the droplets had a higher velocity and hence, a significantly lower amount of time was available for their visualization. Finally, a flow rate of 1 liter per minute was chosen to perform the experiments since it allowed a constant distribution of air RH and temperature, and relatively moderate residence times for the droplets.

Chapter 4

Results – Numerical

The proposed method to solve the numerical model developed in Chapter 2, and a series of predicted results are presented in this chapter. The aim of the numerical model implementation is to find the temperature and mass fraction of water vapor at the droplet surface, as well as the water mass flow rate, that coincidentally satisfies the heat and mass transfer phenomena for the steady state assumption for a given set of droplet radius, ambient temperature, ambient relative humidity and radiation flux rate. If the problem were formulated as being fully de-coupled, the challenge would be to find the spatial gradient of temperature and mass fraction at the surface that allows $\dot{m}_{\text{energy}} = \dot{m}_{\text{species}}$, where $\dot{m}_{\text{energy}}$ is the mass flow associated with the energy equation and $\dot{m}_{\text{species}}$ is the mass flow associated with the species equation, as it was introduced in Chapter 2. Although strictly speaking, there is only one driving mechanism for evaporation, which is the difference in vapor concentration between the surface and the ambient gas, the concept of $\dot{m}_{\text{energy}}$ and $\dot{m}_{\text{species}}$ was introduced as a means to bring these two balance equations into agreement since they share a common water mass flow rate. After calculating a steady state mass flow rate, a time step would be taken to calculate the new mass of the droplet and the process repeated until a minimum droplet size was achieved.

The algorithm implemented to solve the numerical model is shown below. The computational code that was generated following the algorithm steps can be found in Appendix C:

- Set the initial value of the droplet radius, and the temperature and the relative humidity of the environment air, *i.e.*, r_s, T_∞ and RH_∞, respectively.

- Calculate the mass fraction of water vapor, Y_∞ at the far field position relative to the surface of the droplet (*i.e.,* $r = r_\infty$) using the model proposed in Equation 2.63 to obtain the saturation vapor pressure at the given conditions. The far field position, r_∞, is an arbitrary distance that is much larger than the radius of the droplet (*e.g.*, two orders of magnitude higher). For this work, a value of 1 cm was used.

- Estimate the total incoming radiative heat into the droplet, $\dot{Q}_\mathrm{rad}$, for a droplet of that size by multiplying the amount of energy per unit area, $\dot{Q}''_\mathrm{rad}$, times the projected area of the droplet. The absorption occurs over the depth of the droplet.

- Select a value of the surface temperature, $T_\mathrm{s} = T|_{r=r_\mathrm{s}}$.

- Calculate the vapor properties: c_p, λ and h_{fg} at $r = r_\mathrm{s}$.

- Guess a value for $\dot{m}_{\,\mathrm{energy}}$.

- Calculate A', B and $\left.\frac{\mathrm{d}T}{\mathrm{d}r}\right|_{r=r_\mathrm{s}}$ from Equations 2.44 and 2.46.

- Calculate $\dot{m}^*{}_\mathrm{energy}$ from Equation 2.26, where the "*" represents a refined guess on the mass flow rate.

- Since the guess of $\dot{m}_\mathrm{energy}$ will not equal $\dot{m}^*{}_\mathrm{energy}$, then iterate by letting the new guess of $\dot{m}_\mathrm{energy} = \dot{m}^*{}_\mathrm{energy}$, continue to iterate until reaching convergence, *i.e.,* $\frac{\left||\dot{m}_\mathrm{energy}|-|\dot{m}^*{}_\mathrm{energy}|\right|}{|\dot{m}^*{}_\mathrm{energy}|} \ll 0.01.$

- Repeat the iterative process for several values of T_s and plot $\dot{m}_\mathrm{energy}$ versus T_s for the given droplet size and ambient conditions, as shown in Figure 4.1. This plot shows a series of solutions of the energy equation of the gas phase coupled with the energy balance done in the liquid phase, which is the function $\dot{m}_\mathrm{energy}$. The problem is that without the species equation it is impossible to know the point along this plotted curve where this mass flow coincidentally equals $\dot{m}_\mathrm{species}$.

- For each value of T_s, the mass fractions of water vapor and air at the surface conditions, $Y_\mathrm{vap,s}$ and $Y_\mathrm{air,s}$, respectively, are calculated by Equations 2.4, 2.63 and 2.66, and the following definition:

$$Y_\mathrm{air,s} = 1 - Y_\mathrm{vap,s}$$

- Calculate the density of the gas mixture, ρ_{mix}, using the ideal gas law:

$$\rho_{\mathrm{mix}} = \frac{P\,W_{\mathrm{mix}}}{R\,T_s}$$

where:

$$W_{\mathrm{mix}} = Y_{\mathrm{vap,s}}\,W_{\mathrm{vap}} + Y_{\mathrm{air,s}}\,W_{\mathrm{air}}$$

to capture the temperature dependency (density variations due to compositional changes are not included).

- Calculate the diffusivity coefficient of water vapor with respect of the mixture, $D_{\mathrm{vap,mix}}$, using Equation 2.62.

- Apply a shooting method to solve the second-order ordinary differential equation (Equation 2.61) with boundary conditions for each T_{s} and obtain the value of $\left.\frac{\mathrm{d}Y_{\mathrm{k}}}{\mathrm{d}r}\right|_{r=r_{\mathrm{s}}}$ that satisfies the boundary conditions $Y_{\mathrm{vap}}(r = r_{\mathrm{s}})$ and $Y_{\mathrm{vap}}(r = r_{\infty})$ to calculate $\dot{m}_{\mathrm{species}}$.

- Plot $\dot{m}_{\mathrm{species}}$ versus T_{s}, as shown in Figure 4.1, to show the series of solutions of the species equations.

- Locate the intersection of the mass flow rate versus surface temperature curves due to heat and mass transfer to find a unique solution of $\dot{m}$ and T_s.

- As part of the quasi-steady approximation, allow this unique mass flow from the droplet to exist for a time period to evaporate a small fraction of the droplet's mass (*e.g.*, 0.1% of the droplet mass) – record the results of this time step.

- Calculate the new droplet size, r_s, with the smaller mass and repeat entire numerical methods (with a new total radiation energy striking its smaller profile) until the droplet reaches a size that is no longer of interest.

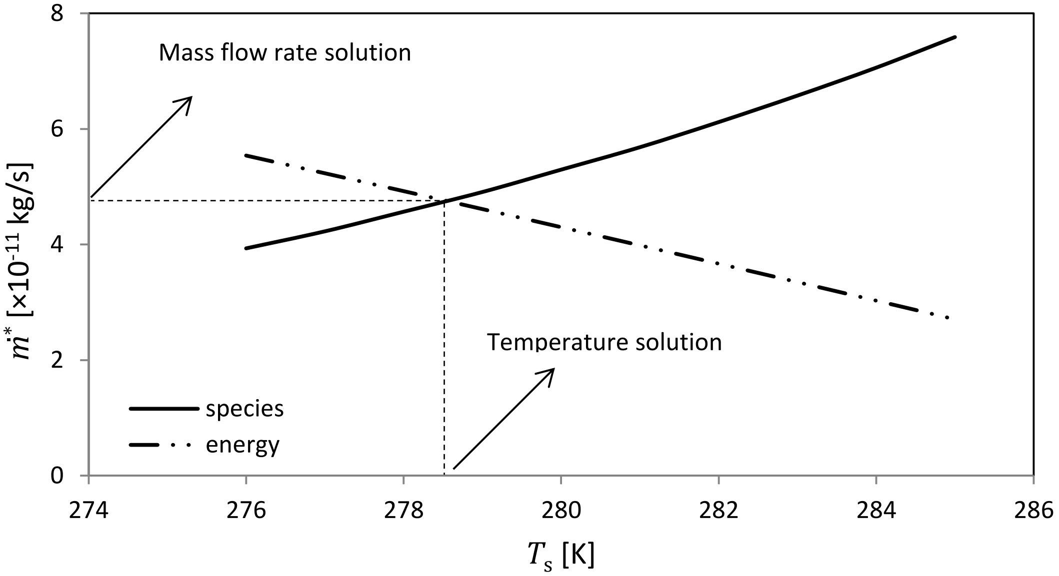

Figure 4.1: Unique solution (T_s , $\dot{m}$) of the system of differential equations (energy + species) for a single time step iteration.

The algorithm was coded using commercial software (Matlab version 8.0.0.783, The MathWorks Inc.) in order to obtain numerical data of various simulation scenarios. The second order ordinary differential equation (ODE) was solved using the built-in function *ode45,* which is based in the Runge-Kutta-Fehlberg method for non-stiff problems. The commercial software code used can be found in Appendix C.

4.1 Numerical Simulations

Different scenarios were studied in order to test the numerical model with different conditions of relative humidity and infrared radiation. Four main simulation cases, with different relative humidity values of 0%, 30%, 60% and 90%, were studied. The environment air temperature, T_{∞}, and the initial droplet diameter used for all the simulation cases were 20 °C and 50 µm, respectively. The material properties of the water vapor (specific heat, thermal conductivity, diffusion coefficient and latent heat of vaporization) were calculated using the *1/3 rule* method proposed by Hubbard *et al*. (1975) and later implemented by Vehring *et al*. (2007). The method consists in evaluating the properties at a value of temperature and vapor mass fraction that results in adding one third of the difference between the values at the droplet's surface and the far-field condition to the original temperature and mass fraction at the surface. Different values of radiative heat transfer rate per unit area ($\dot{Q}''_{\mathrm{rad}}$) were tested in each of the four relative humidities, ranging between 0 and 10000 $\frac{\mathrm{mW}}{\mathrm{mm}^2}$ with increments of 1 order of magnitude between each value (*i.e.*, 10, 100, 1000, and 10000), with the addition of two intermediate magnitudes of 200 and 500 $\frac{\mathrm{mW}}{\mathrm{mm}^2}$, respectively, which is the power intensity limits of the IR laser used in the experiments. The results for each simulation will be presented in two different figures. The first set of figures (Figures 4.2, 4.4, 4.6, and 4.8) show the evolution of the droplet diameter with respect to time. Various time resolutions (time steps) were decreasingly implemented for each simulation in order to determine the minimum resolution at which the droplet diameter did not vary significantly (i.e., < 1%) with respect to a previous iteration (*i.e.,* a larger time step) without significantly increasing the computational time.

The second set of figures (Figures 4.3, 4.5, 4.7, and 4.9) were plotted in order to determine the total evaporation time of each simulation without significantly increasing the computational effort. The plots show the evolution of d^2, with respect to time. A linear fitting was performed to d^2 with respect to time for the simulation cases with no radiation and a second-order polynomial was fit to the remaining data, with a resulting coefficient of determination, R^2, better than 0.9999 for all the studied cases. The intersection between the fitted curve and the horizontal axis of the figures was calculated numerically and plotted into Figure 4.15, which shows the total evaporation time with respect to the incident radiation heat transfer rate per unit area, $\dot{Q}''_{\mathrm{rad}}$, for the four different RH scenarios.

4.1.1 Low Relative Humidity

Figure 4.2 shows the evolution of the droplet diameter with respect to time for a simulation scenario with an initial droplet diameter of 50 µm, an environmental temperature of 20 °C, a relative humidity of 0%, and various values of infrared radiation per unit area (*i.e.*, a range of 0 to 10000 $\frac{\mathrm{mW}}{\mathrm{mm}^2}$) at a wavelength of 2.8 µm, where the absorptivity of water is maximum. A distinctly non-linear evolution of the droplet diameter can be observed for all the curves with an incident radiation lower than 500 $\frac{\mathrm{mW}}{\mathrm{mm}^2}$, with a slope that is approximately constant between the initial droplet diameter (50 µm) and 20 µm. After this, a negatively increasing slope can be observed between 20 µm and 0 µm. For the curves with incident radiation values higher than 1000 $\frac{\mathrm{mW}}{\mathrm{mm}^2}$, this effect cannot be easily observed due to the low resolution of the horizontal axis of the figure in which these results are shown.

The time of evaporation of the droplets decreases with increasing radiation. A relatively small difference (*i.e.*, less than 10%) in the time of evaporation can be observed between the curve with $\dot{Q}''_{\mathrm{rad}} = 0\,\frac{\mathrm{mW}}{\mathrm{mm}^2}$ and the curve with $\dot{Q}''_{\mathrm{rad}} = 10\,\frac{\mathrm{mW}}{\mathrm{mm}^2}$ for the case of 0% RH. However, the difference in evaporation time between the cases without incident radiation and the ones subjected to radiation will increase for the cases with relative humidity larger than zero.

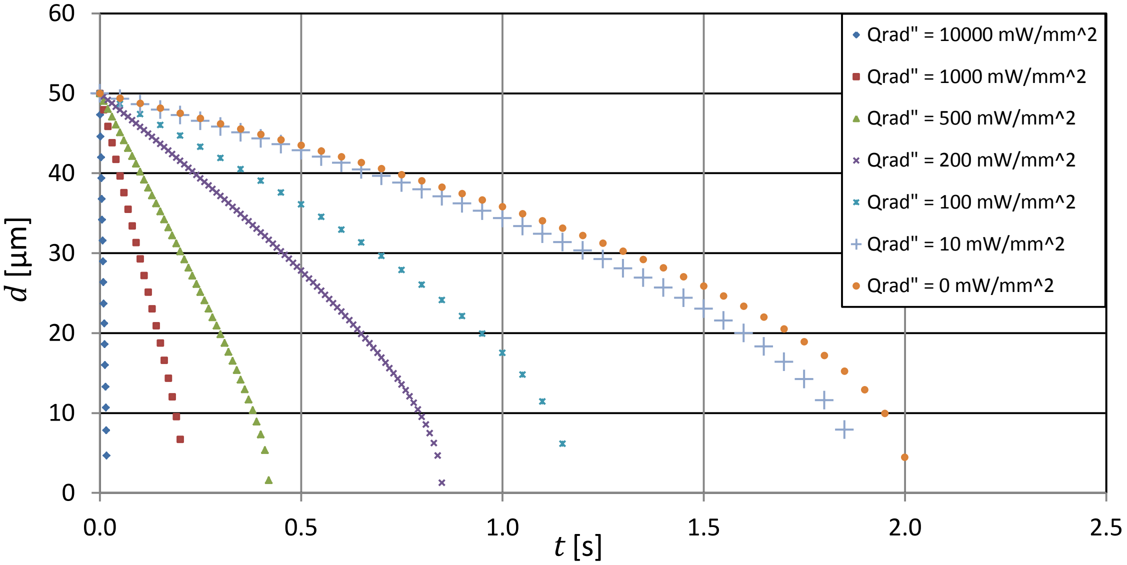

Figure 4.2: Evolution of droplet diameter (micrometers) with respect to time (seconds) for pure water droplets with conditions of RH = 0%, T_∞= 20 °C, initial diameter of 50 μm and varying infrared radiation

Figure 4.3 shows the evolution of the squared droplet diameter with respect to time. A constant slope can be observed in the simulation curve with no incident radiation ($\dot{Q}''_{\mathrm{rad}} = 0\,\frac{\mathrm{mW}}{\mathrm{mm}^2}$) in contrast with the simulation curves with $\dot{Q}''_{\mathrm{rad}} > 0$, where a negatively decreasing slope can be observed when the time increases. The linear behavior of the curve without incident radiation can be described using the expression shown in Equation 2.13 of Chapter 2 for the case of the steady-state evaporation of droplets, as it was described by Vehring, Foss, and Lechuga-Ballesteros (2007):

$$d(t)^2 = {d_0}^2 - \kappa\, t \tag{4.1}$$

where d_0 is the initial droplet diameter, t is the time, and κ is the evaporation rate in units of area per unit time. In Figures 4.3, 4.5, 4.7, and 4.9, a constant evaporation rate, κ, can be observed for all the droplet evaporation simulations with zero incident radiation. This gives an indication that the evaporation of liquid droplets under the steady-state assumption and without an external energy is purely a surface phenomenon as expected. With external radiation, the amount of energy absorption also depends on the depth of the droplet, not just its frontal area, so the situation is not strictly an area phenomenon.

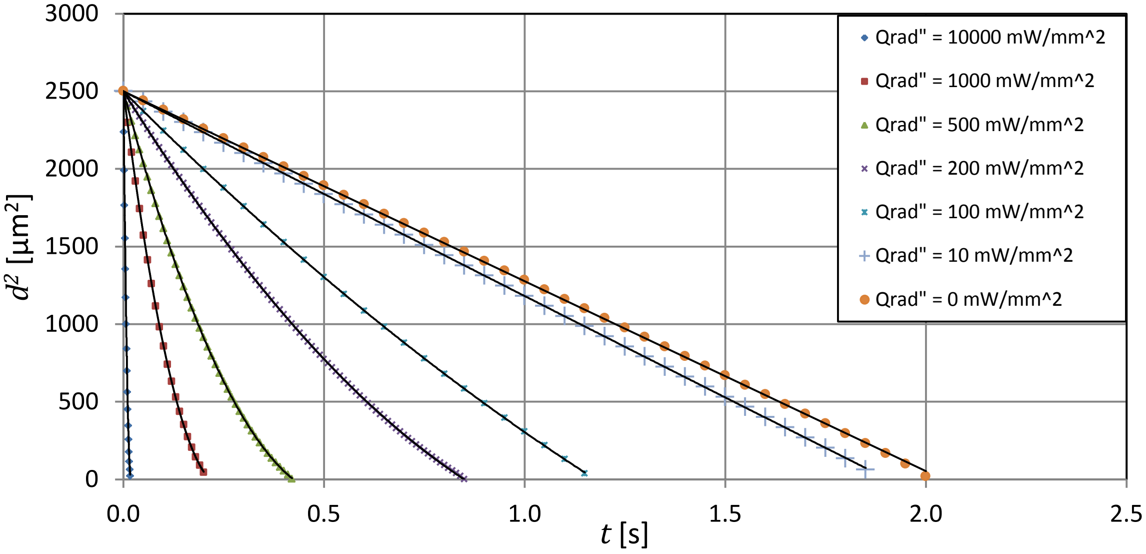

Figure 4.3: Evolution of squared diameter (micrometers squared) with respect to time (seconds) for pure water droplets with conditions of RH = 0%, T_∞= 20 °C, initial diameter of 50 μm and varying infrared radiation

For the cases with $\dot{Q}''_{\mathrm{rad}} > 0$ it can be observed that the constant evaporation rate model shown by Equation 4.1 is no longer valid since the curves do not have a constant slope. It can be observed that the evaporation rate is nearly constant for early times and decreases gradually with increasing time. It can also be observed that the value of the varying slope for the case of droplets with $\dot{Q}''_{\mathrm{rad}} > 0$ is never lower than the value of the slope for the case of droplets without incident radiation. An explanation of this phenomenon is the fact that the introduction of an external energy term that is not constant but dependent upon the size of the droplets, such as $\dot{Q}''_{\mathrm{rad}}$, will dominate the heat transfer over the heat conduction. Therefore, the rate of evaporation will increase until the size of the droplet is small enough so little radiation is absorbed and the conduction between the gas phase and the liquid phase of the droplet becomes the dominating effect, as is the case of droplets with $\dot{Q}''_{\mathrm{rad}} = 0$.

4.1.2 Medium Relative Humidities:

Similar results were obtained for the simulation cases with 30% and 60% RH. An increase of the total evaporation time can be observed with increasing relative humidity. For the cases with zero incident radiation this difference between the total evaporation time between 0%, 30%, and 60% becomes more evident. Droplets subjected to radiation values of $\dot{Q}''_{\mathrm{rad}} = 10\,\frac{\mathrm{mW}}{\mathrm{mm}^2}$ are also observed to increase their total evaporation time significantly (*i.e.*, a 45% increase in evaporation time between 0% RH and 30% RH, and a 36% increase in evaporation time between 30% RH and 60% RH) with increasing RH. A smaller difference in evaporation time between RH cases occurs when the magnitude of the radiation is higher than $\dot{Q}''_{\mathrm{rad}} = 10\,\frac{\mathrm{mW}}{\mathrm{mm}^2}$, becoming almost undistinguishable for the highest radiation cases.

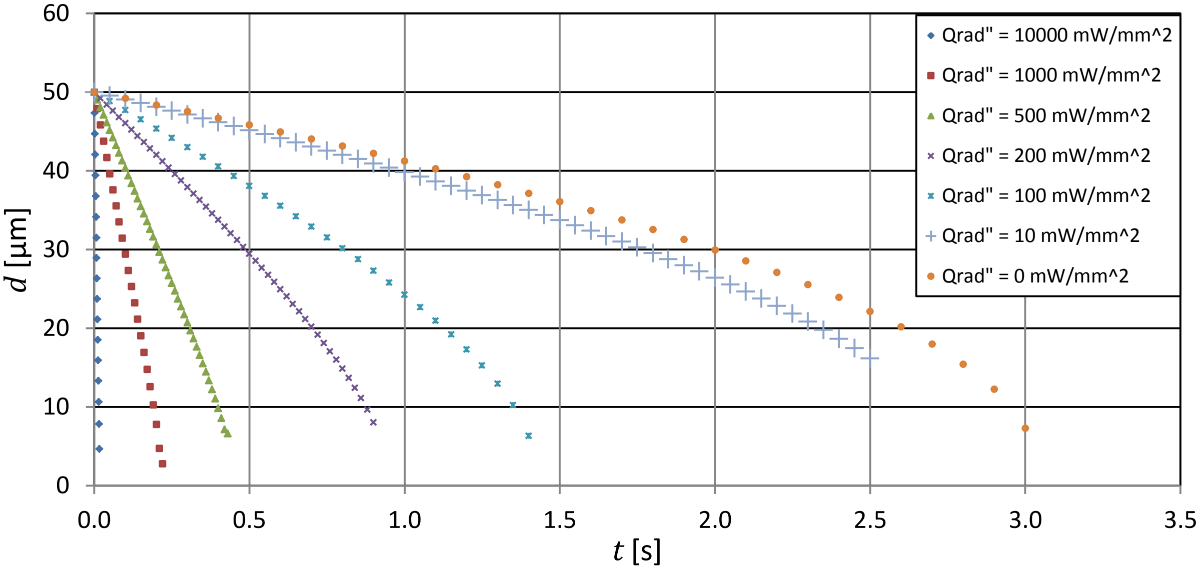

Figure 4.4: Evolution of droplet diameter (micrometers) with respect to time (seconds) for pure water droplets with conditions of RH = 30%, T_∞= 20 °C, initial diameter of 50 µm and varying infrared radiation

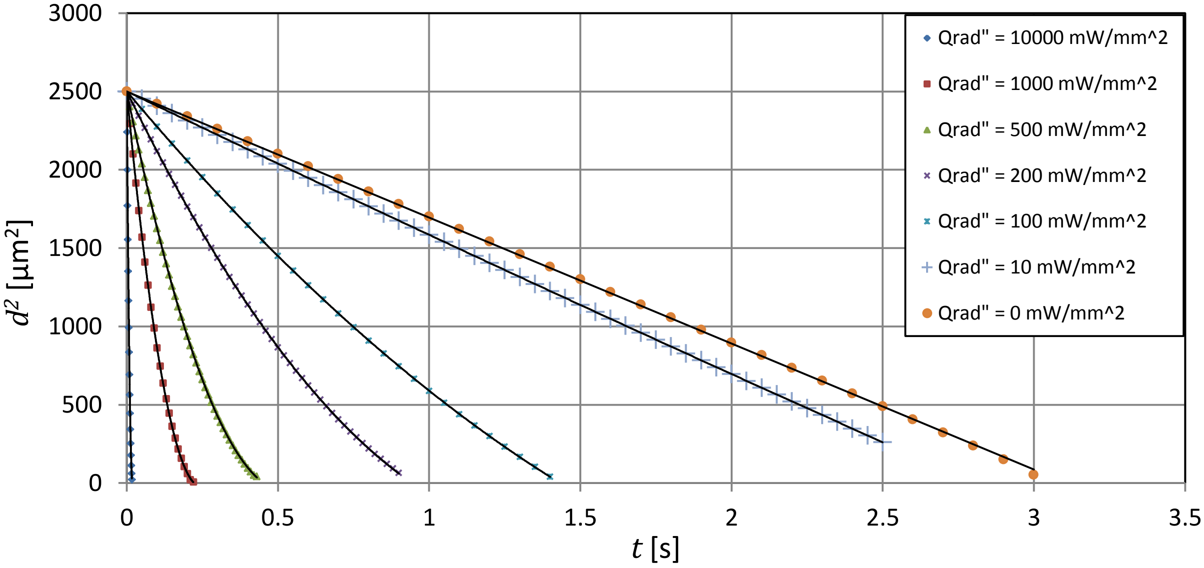

Figure 4.5: Evolution of squared diameter (micrometers squared) with respect to time (seconds) for pure water droplets with conditions of RH = 30%, T_∞= 20 °C, initial diameter of 50 µm and varying infrared radiation

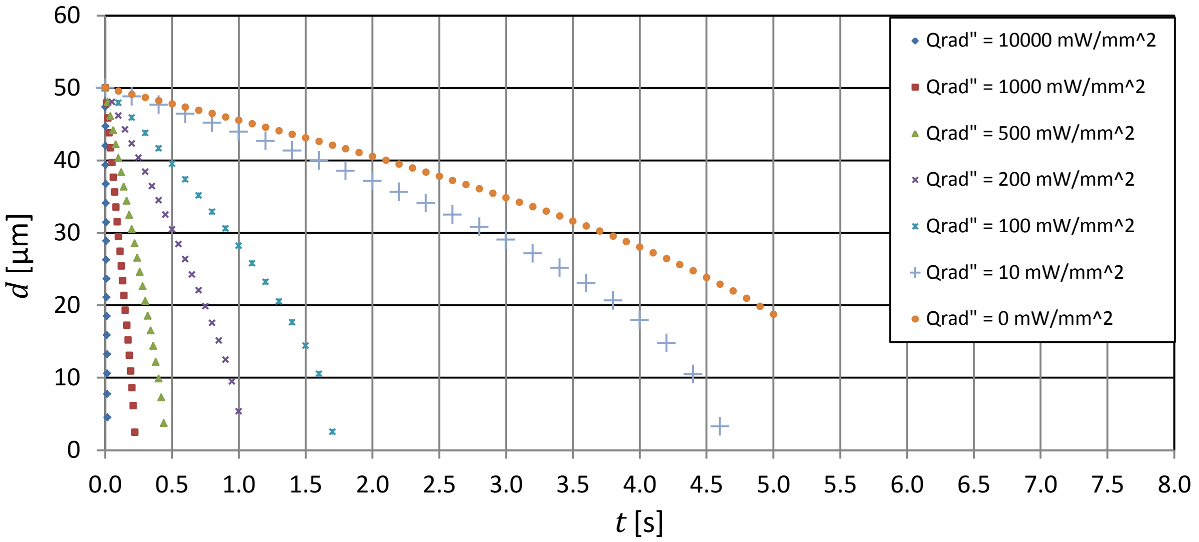

Figure 4.6: Evolution of droplet diameter (micrometers) with respect to time (seconds) for pure water droplets with conditions of RH = 60%, T_{∞}= 20 °C, initial diameter of 50 µm and varying infrared radiation

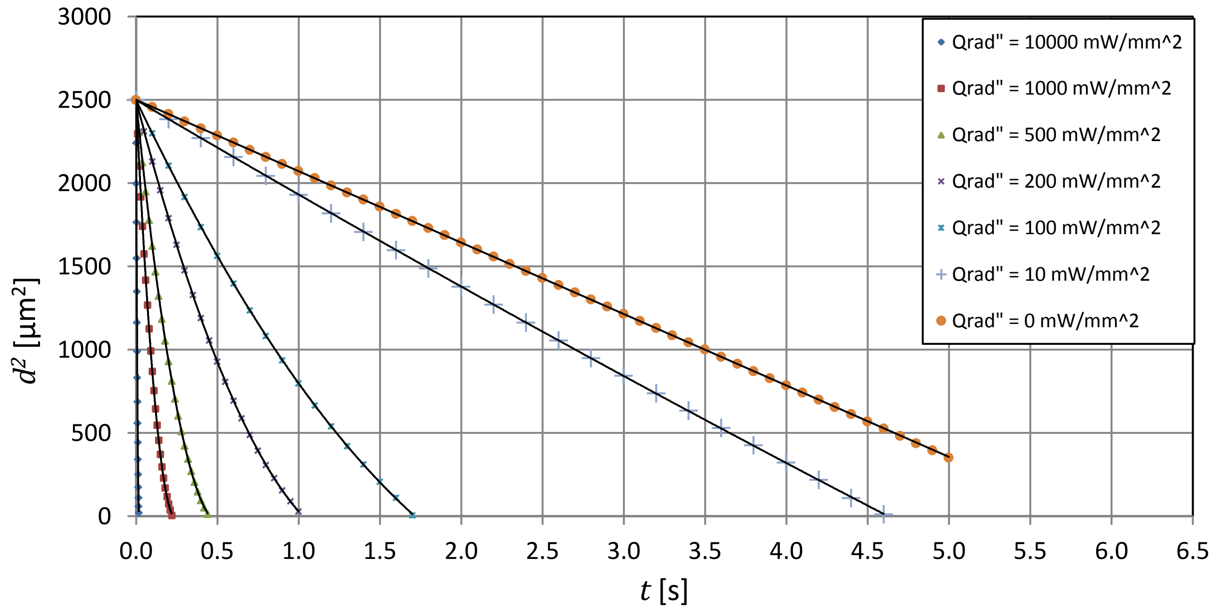

Figure 4.7: Evolution of squared diameter (micrometers squared) with respect to time (seconds) for pure water droplets with conditions of RH = 60%, T_{∞}= 20 °C, initial diameter of 50 µm and varying infrared radiation

4.1.3 High Relative Humidity

A significant increase in the evaporation time of droplets without incident radiation and 90% relative humidity air can be observed in Figures 4.8 and 4.9. Alternatively, there is no significant increase in the evaporation time of droplets subjected to values of $\dot{Q}''_{\mathrm{rad}} \geq 100\,\frac{\mathrm{mW}}{\mathrm{mm}^2}$. It can be observed that the complete droplet evaporation for the case of $\dot{Q}''_{\mathrm{rad}} = 10\,\frac{\mathrm{mW}}{\mathrm{mm}^2}$ is achieved approximately at half of the time (*i.e.*, 12s) that takes the droplets without radiation to achieve a complete evaporation, as it is shown in Figure 4.9. This result is in contrast with the low and medium relative humidity results, in which the two curves reached a complete evaporation with a difference smaller than 1 second. Thus, one conclusion is that the introduction of an external energy, such as $\dot{Q}''_{\mathrm{rad}}$, will reduce drastically the dependence of the total time of evaporation on the relative humidity whereas the evaporation time for droplets without incident radiation grows significantly with increasing relative humidity.

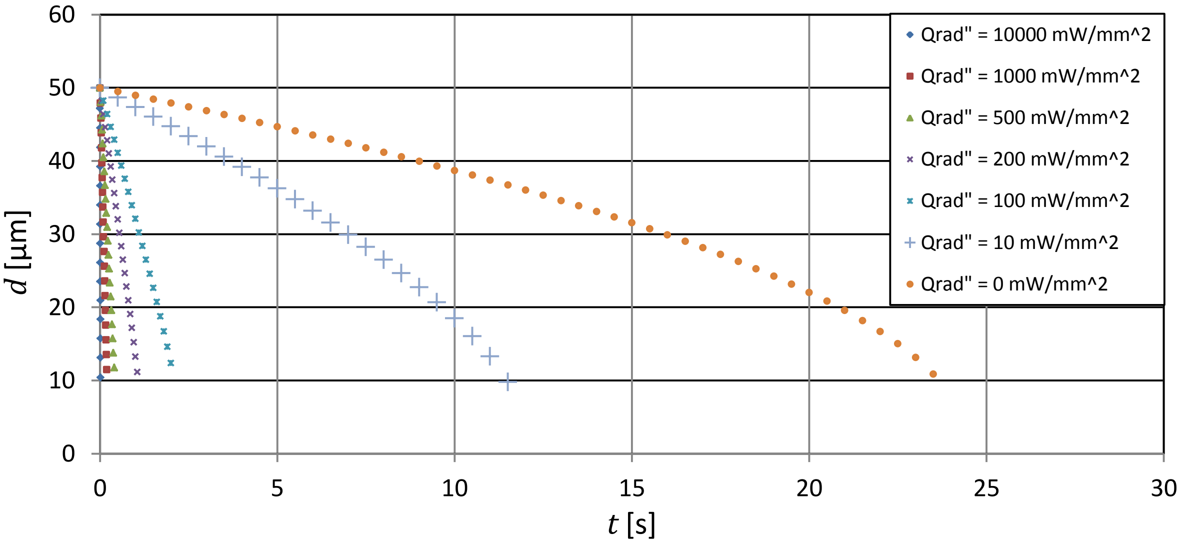

Figure 4.8: Evolution of droplet diameter (micrometers) with respect to time (seconds) for pure water droplets with conditions of RH = 90%, T_∞= 20 °C, initial diameter of 50 µm and varying infrared radiation

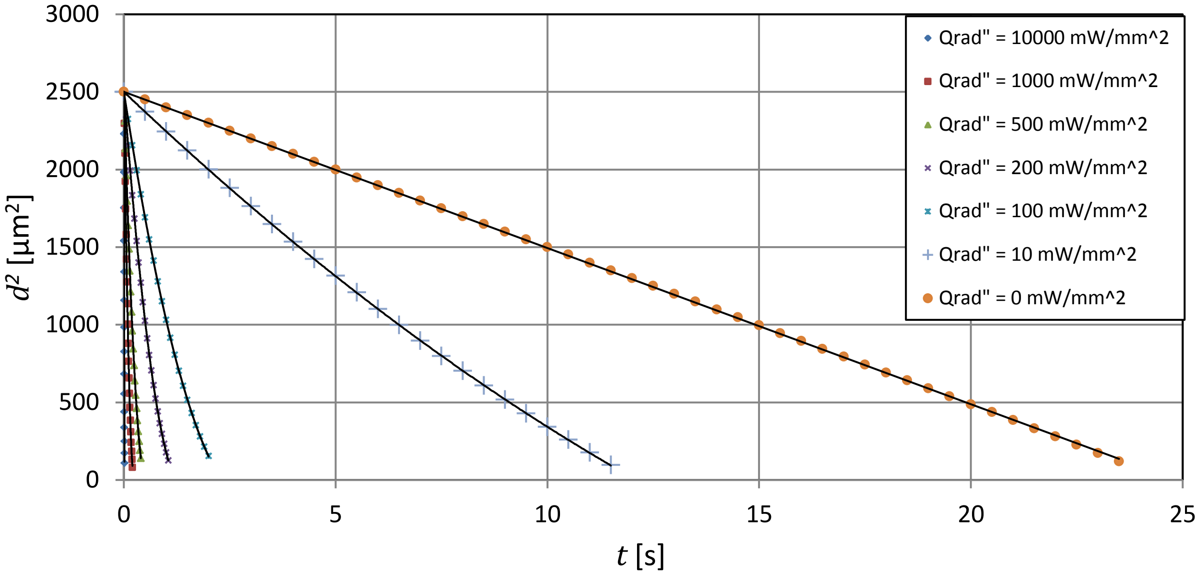

Figure 4.9: Evolution of squared diameter (micrometers squared) with respect to time (seconds) for pure water droplets with conditions of RH = 90%, T_∞= 20 °C, initial diameter of 50 µm and varying infrared radiation

4.1.4 Influence of infrared radiation and relative humidity on droplet surface temperature and vapor concentration

An alternative method to understand the influence of the external radiation and the environmental relative humidity on the evaporation rate of the droplets is to show how the driving forces of the energy and species conservation equations (*i.e.*, the temperature difference and vapor mass concentration difference, respectively) vary with respect to time for different conditions of radiation and RH. These temperature and vapor concentration differences correspond to the difference between the temperature and vapor concentration values at the surface of the droplet minus the values at the far field (*i.e.*, $[T_s - T_\infty]$ and $[Y_s - Y_\infty]$, respectively). Although the vapor mass concentration difference is the only driving mechanism for evaporation, the temperature difference affects evaporation since a rise in the temperature of the droplet at the surface will increase the saturation vapor pressure, $P_{\text{vap,s}}$, and the mass flow rate of vapor diffusing away from the droplet surface will increase, as it was shown in Equation 2.5.

Figure 4.10 shows the variation of the droplet temperature at the surface, T_s, with respect to the normalized droplet diameter for different radiation intensities with air temperature and relative humidity of 20 °C and 0%, respectively. Additionally, Figure 4.11 shows the variation of the vapor mass fraction, Y_s, with respect to the normalized droplet diameter for the same conditions. The time parameter shown in the horizontal axis is represented by the normalized diameter, which is equal to the droplet diameter at each time step divided by the initial droplet diameter (50 µm) since the total evaporation time is different for each radiation intensity case (*i.e.,* for droplets with an initial diameter of 50 µm, the time of evaporation is approximately 2 seconds for the no incident radiation case, and approximately 0.4 seconds for the case with an incident radiation of 500 mW/mm^2).

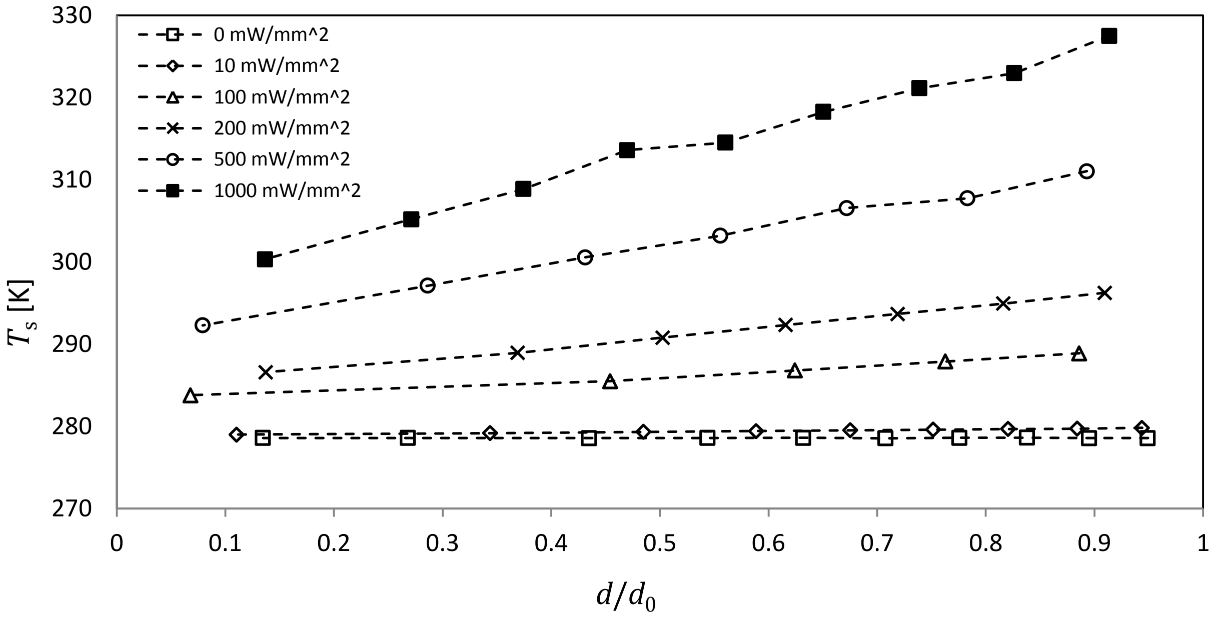

Figure 4.10: Variation of the surface temperature of water droplets, T_s, with respect to droplet size for various amounts of infrared radiation intensities, RH = 0%, and T_∞= 293.15 K

From Figure 4.10 it can be observed that the average surface temperature increases with increasing values of radiation intensity. By examining in detail the case with no incident radiation, $\dot{Q}''_{\mathrm{rad}} = 0\,\frac{\mathrm{mW}}{\mathrm{mm}^2}$, it can be observed that the droplet temperature falls below the ambient to a value of approximately 278.5 K and then maintains a constant value for the remaining of the droplet lifetime, as it was described in Chapter 2. In contrast, as the radiation intensity increases, a constant temperature of the droplet surface is no longer observed. For cases with radiaton intensities in the range $0\,\frac{\mathrm{mW}}{\mathrm{mm}^2} < \dot{Q}''_{\mathrm{rad}} \leq 200\,\frac{\mathrm{mW}}{\mathrm{mm}^2}$, a decrease in the surface temperature occurs below the temperature of the environment, while for $\dot{Q}''_{\mathrm{rad}} > 200\,\frac{\mathrm{mW}}{\mathrm{mm}^2}$ the value of T_{s} remains greater than T_{∞} during the complete lifetime of the droplet. This decrease in the droplet temperature with respect to a decreasing droplet diameter is not due only to a smaller projected area (*i.e.,* the area of the droplet that is exposed to radiation) but also to a reduced depth, hence, the droplet absorbs less radiation with time.

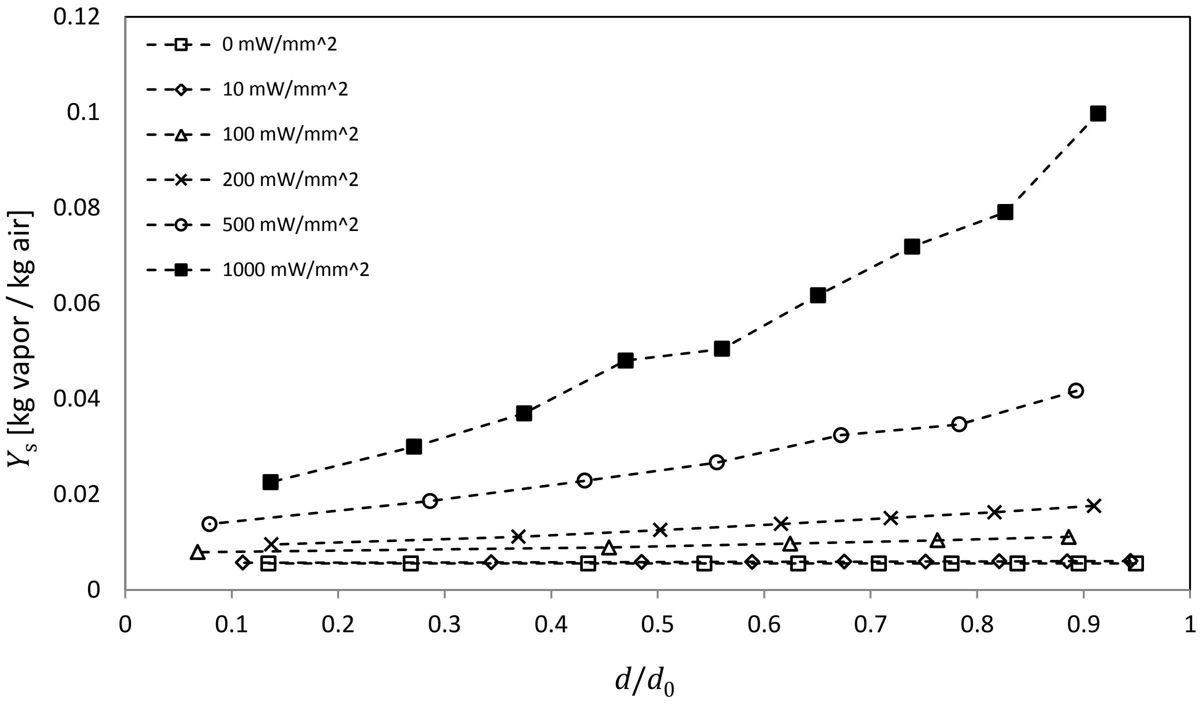

Figure 4.11: Variation of the vapor mass fraction at the surface of water droplets, Y_s, with respect to droplet size for various amounts of infrared radiation intensities, RH = 0%, and T_∞= 293.15 K

Figure 4.11 shows the variation of the water vapor mass fraction at the droplet surface, Y_s, with respect to the lifetime of the droplets for the same conditions shown in Figure 4.10. A high similarity can be observed between both figures, which shows the indirect influence that the droplet temperature has over the evaporation rate. A clear correlation can be observed between $\dot{Q}''_{\mathrm{rad}}$ and Y_s, such that the value of Y_s increases with increasing $\dot{Q}''_{\mathrm{rad}}$. Figure 4.11 also describes the behavior of the evaporation driving force ($Y_s - Y_\infty$) since at 0% RH the value of the water vapor mass fraction at the far field, Y_∞, is equal to zero, thus, the model predicts that the evaporation will increase with increasing radiation, as expected.

By observing the evolution of Y_s with respect to the droplet lifetime in Figure 4.11 for the different radiation intensity cases, it is straightforward to conclude that the introduction of an external energy term, such as infrared radiation, into the energy balance of the droplet converts that part of the problem into a non-steady phenomenon, but as with other non-steady effects it is neglected because the sensible energy changes of the liquid are small compared to that associated with the phase change.

Another significant objective of this study is to investigate the effect that the relative humidity of the environmental air has over the surface temperature and vapor mass fraction of the droplet for a case where the droplet is being heated by a given radiation intensity. Since it is already known that an increase in the radiation intensity will result in an increased evaporation rate, only one radiation intensity ($\dot{Q}''_{\mathrm{rad}} = 200\frac{\mathrm{mW}}{\mathrm{mm}^2}$) was selected for the numerical analysis. Additionally, four different values of relative humidity (*i.e.,* 0%, 30% 60% and 90%) and air temperature of 293.15 K were selected to perform the simulation. Figures 4.12 and 4.13 show the variation of the surface temperature, T_{s}, and the surface vapor mass fraction, Y_{s}, of the droplet at the given conditions, respectively.

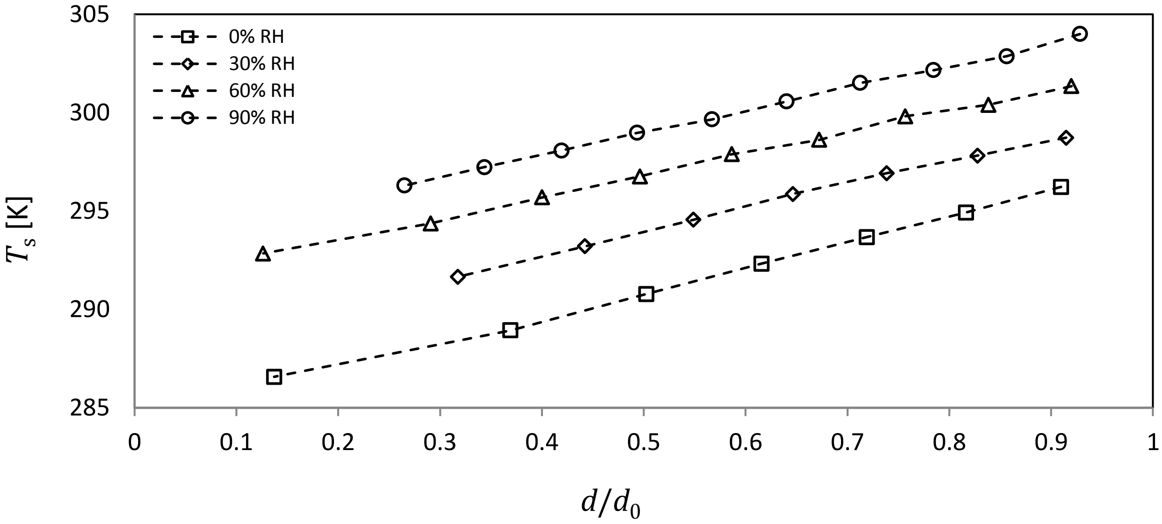

Figure 4.12: Variation of the surface temperature of water droplets, T_{s}, with respect to droplet size for various conditions of relative humidity, with a constant radiation intensity of $\dot{Q}''_{\mathrm{rad}} = 200\frac{\mathrm{mW}}{\mathrm{mm}^2}$ and T_{∞}= 293.15 K

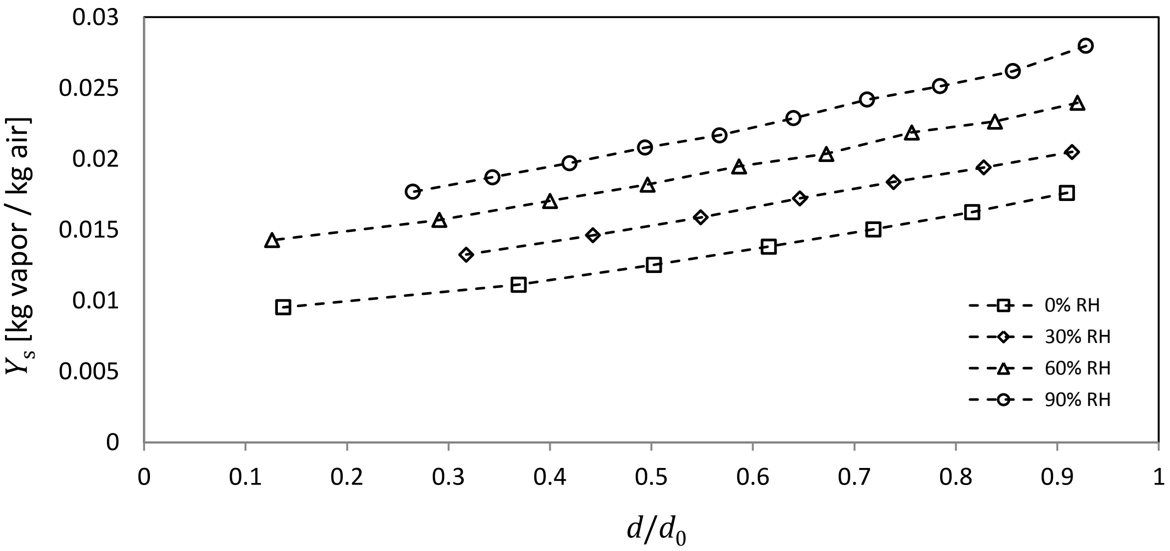

Figure 4.13: Variation of the vapor mass fraction at the surface of water droplets, Y_s, with respect to droplet size for various conditions of relative humidity, with a constant radiation intensity of $\dot{Q}''_{\mathrm{rad}} = 200\,\frac{\mathrm{mW}}{\mathrm{mm}^2}$ and T_∞= 293.15 K

As observed in Figure 4.12, the surface temperature of the droplet increases for increasing values of environmental relative humidity. Similarly to the cases with incident radiation (shown by Figure 4.10), and assuming an initial droplet temperature of 293.15 K, the magnitude of T_s increases initially up to a maximum value and is observed to decrease linearly with respect to the droplet lifetime for all the studied RH cases. The four RH cases show a similar slope, showing no apparent relative importance over each other within the droplet lifetime range.

A similar behavior can be observed for the different RH cases in Figure 4.13, where an increased value of the environmental relative humidity results in increased values of the surface vapor mass fraction, Y_s. However, for this case, the fact that the values of Y_s are higher for higher values of RH does not imply that the evaporation rate increases with RH since the values of Y_∞ are different than zero for RH > 0%. Therefore, the values of Y_∞ for each RH case must be subtracted from Y_s in order to observe the real effect of increasing the amount of the environmental relative humidity on the evaporation rate. Figure 4.14 shows the variation of $Y_s - Y_\infty$ with respect to the droplet lifetime for the different cases of RH.

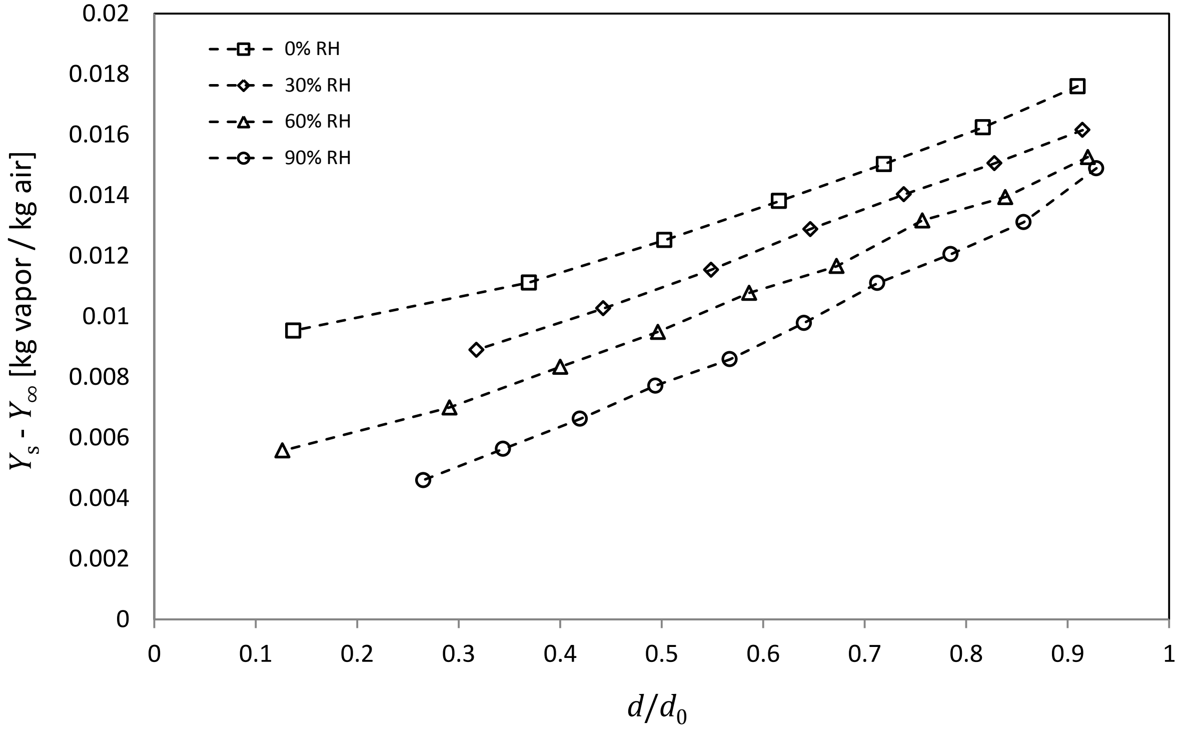

Figure 4.14: Variation of the vapor mass fraction difference, $Y_s - Y_\infty$, with respect to droplet size for various conditions of relative humidity, with a constant radiation intensity of $\dot{Q}''_{\mathrm{rad}} = 200\,\frac{\mathrm{mW}}{\mathrm{mm}^2}$ and T_∞= 293.15 K

From Figure 4.14 it can be observed that an increase in RH results in a decrease in the driving force of evaporation, $Y_s - Y_\infty$, and thus a decrease in the evaporation rate for the same conditions of incident radiation and air temperature. Additionally, if a comparison is made between the results given in Figure 4.14 with the results given in Figure 4.11, it can be shown that there exists a minimum value of radiation intensity, $\dot{Q}''_{\mathrm{rad}}$, for which the evaporation rate of a liquid droplet in a 90% RH environment is higher than the evaporation rate of a similar droplet immersed in a dry air environment, thus, making the effect of infrared radiation on evaporation more important than relative humidity.

4.2 Time for complete evaporation

Figure 4.15 shows a summary of the simulation results obtained in this section and represented by Figures 4.2 - 4.9. The total predicted evaporation time was calculated for several values of incident radiation at a constant relative humidity. Four different relative humidity cases (0%, 30%, 60%, and 90%) were studied. The time for complete evaporation was calculated numerically by intersecting the fitted curves obtained in Figures 4.3, 4.5, 4.7 and 4.9 with the horizontal axis. The results shown below are only predictive since the numerical model loses accuracy when the droplet diameter is below 10 μm, however, it is assumed that most of the evaporation time is spent where the droplet diameter is between 50 μm and 10 μm.

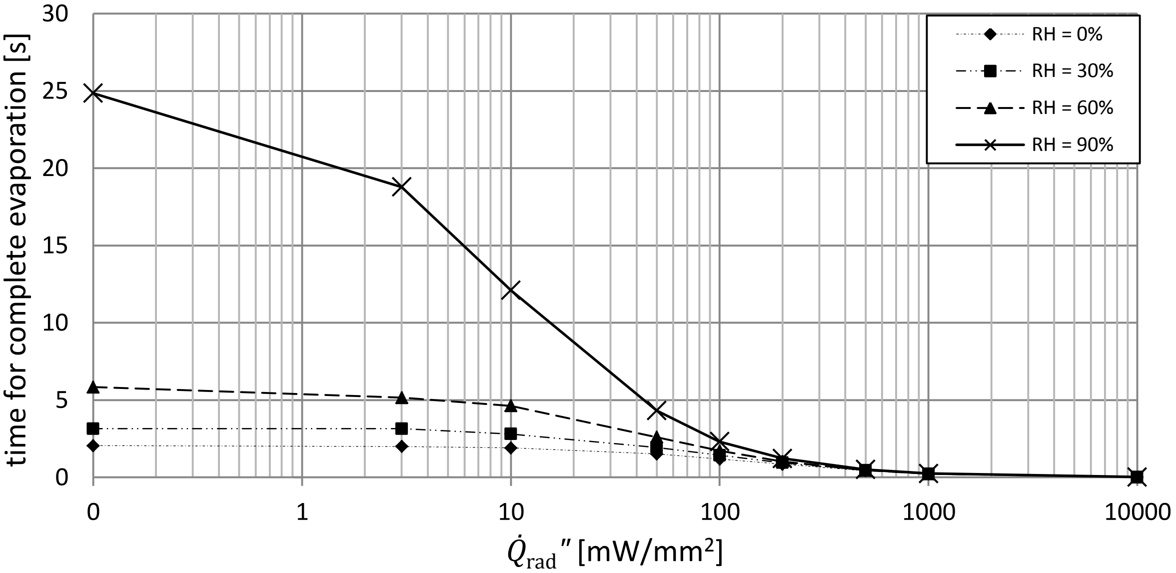

Figure 4.15: Variation of the total predicted time of evaporation with respect to the infrared heat per unit area for pure water droplets with varying conditions of RH (0%, 30%, 60% and 90%), T_∞= 20 °C, and initial diameter of 50 μm.

From the figure it can be observed that the difference of the evaporation times between the four RH scenarios decreases with increasing radiation, $\dot{Q}''_{\mathrm{rad}}$, and the evaporation times tend to converge into a single curve. Another remark can be made at low incident radiation values (*i.e.*, between 0 and 10 $\frac{\mathrm{mW}}{\mathrm{mm}^2}$), in which the evaporation time is observed to increase exponentially with linearly increasing relative humidity, which may differ from intuition. This can be observed in Figure 4.16, which shows the variation of the total evaporation time with respect to increasing relative humidity for the case of water droplets with low incident radiation intensities (*i.e.*, 0, 3, and 10 $\frac{\mathrm{mW}}{\mathrm{mm}^2}$).

However, this phenomenon is observed to be attenuated by an increasing amount of incident radiation into the droplets, and it is practically negligible for cases where $\dot{Q}''_{\mathrm{rad}} \geq 100\,\frac{\mathrm{mW}}{\mathrm{mm}^2}$. Although the results presented in this chapter are merely predictive, they offer a clear description of the effects of relative humidity and infrared radiation on the evaporation of isolated water droplets in the micrometers range, and are not very far from the expectations of the investigation. However, a series of experiments were conducted in order to validate the predicted results of the numerical model for the different IR cases already shown. A single radiation power case will be shown due to limitations of the laser used and the rest of the validation is left for future investigations.

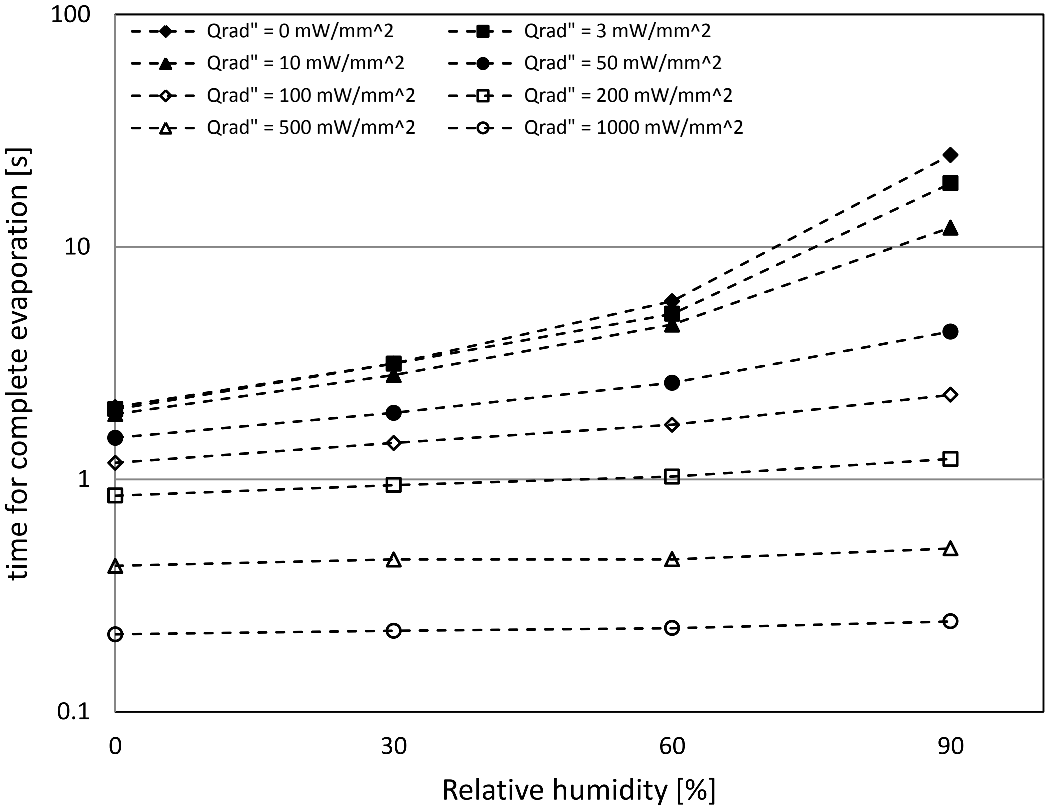

Figure 4.16: Variation of the total predicted time of evaporation with respect to the relative humidity for pure water droplets with T_∞= 20 °C, initial diameter of 50 µm and various radiation intensities.

Chapter 5

Results – Experimental

An analysis of the experimental data obtained is presented in this chapter. All the experiments were conducted using the vertical flow tube assembly described in section 3.1 of Chapter 3. Four different relative humidity (RH) scenarios (0%, 30%, 60% and 90%) were tested for water droplets evaporating with and without incident radiation at room temperatures (19 – 24 °C). An additional scenario for water droplets evaporating at low RH (0%) and air temperature of 60°C is also shown in order to study the effects of ambient temperature on the evaporation rate. Acetone (99% purity) was also used as a test fluid at room temperature (19.5 °C) and dry conditions with zero incident radiation to prove the validity of the numerical model with a substance other than water. A comparison between the experiments and the numerical predicted results is given for all the scenarios. The standard error of estimate, S_{xy}, between the model results and the experimental data points was calculated for all the cases using the following expression:

$$S_{xy} = \sqrt{\frac{\sum_i^n (y_i - {y_i}')^2}{n}} \tag{5.1}$$

where y_i and ${y_i}'$ are the experimental and model data points, respectively, and n is the number of data pairs to be compared. The standard error of estimate is shown in the figures for every case and it represents how well the experimental data fits the model (*i.e.*, how many micrometers is the experimental data away from the model data, on average). A minimum value of $S_{xy} = 0$ means that the model results and the experimental data points are coincident. An additional comparison between the experiments and numerical results obtained by other investigators is also given.

Droplets were produced by the generator's nozzle at a constant frequency of 1 Hz for every scenario discussed in this chapter. The parameters T and RH of air were measured using a type-K thermocouple (± 1.5 °C uncertainty) and a digital hygrometer (± 2% uncertainty), respectively. Air temperature was not subject to strict control, except for the case of T = 60 °C, in which a combination of a heater and a temperature controller was used. Relative humidity was controlled manually by adjusting two needle valves (Model B-1KS4, Swagelok Inc.) that regulated the flow from the dry air source through the humidifier and a dry air bypass, maintaining the same gas flow rate.

In the figures shown below, the vertical axes represent the size of the droplets, in micrometers. The horizontal axes represent the net time (in seconds) with respect to the first measured droplet (*i.e.*, a time of approximately 0.02 seconds after the droplet exits the nozzle, which was constant for all the experiments). This delay was used because droplets with only a vertical motion, at terminal velocity, and in temperature equilibrium were desired in order to adhere to the assumptions of the model. A time of approximately 0.02 seconds was determined experimentally as the time that takes to the droplets to reach a completely vertical motion in the droplet chain. Additionally, at a time of 0.02 seconds, it was estimated (Fuchs, 1959) that the contribution of the transient effects only represent a 5% of the total evaporation rate, thus the droplet can be assumed to be in thermal equilibrium. Finally, at standard conditions, the terminal velocity of droplets with a diameter of approximately 50 µm is reached approximately at 0.02 seconds. Each figure below shows a data point located at a time equals zero that represents the first measured droplet.

In the figures, the symbols are used to represent the experimental data, and the continuous lines are used to represent the results predicted by the numerical model. An initial diameter equal to the value of the first experimental data point (*i.e.*, at $t = 0$ seconds) was selected as the initial value of the droplet diameter in the numerical model in order to compare the numerical and experimental results. Two additional dotted lines above and below the continuous line are used to represent the uncertainty of the model results. The superior and inferior dotted lines were plotted by adding and subtracting a total of $2\sigma_d$ (where σ_d is the standard deviation of the first droplet diameter measured experimentally) to the numerical results for each time step, respectively, hence creating a “confidence band” above and below the numerical results with a confidence of 95%. Additionally, the uncertainties of the experimental data points were calculated using the procedure shown in section 3.3.1 and are not shown in the figures below since the symbols are larger (or about the same size, in the worst case scenario) than the length of the error bars.

5.1 Evaporation of pure water droplets without infrared radiation

5.1.1 Influence of the relative humidity

Figure 5.1 shows the effect of decreasing the environmental relative humidity on the evaporation rate of water droplets with similar conditions of air temperature (approximately 24 °C) and no incident IR radiation. The total time of evaporation was limited to 0.5 seconds due to the length (100 mm) of the optical window; thus, it was not possible to visualize the complete evaporation of the droplets. Figure 5.1(a) shows a comparison between the numerical model and the experimental results for a high RH case (*i.e.,* 90%) in which the evaporation rate is expected to be low and thus the effect of the variation of the initial droplet size can be better appreciated.

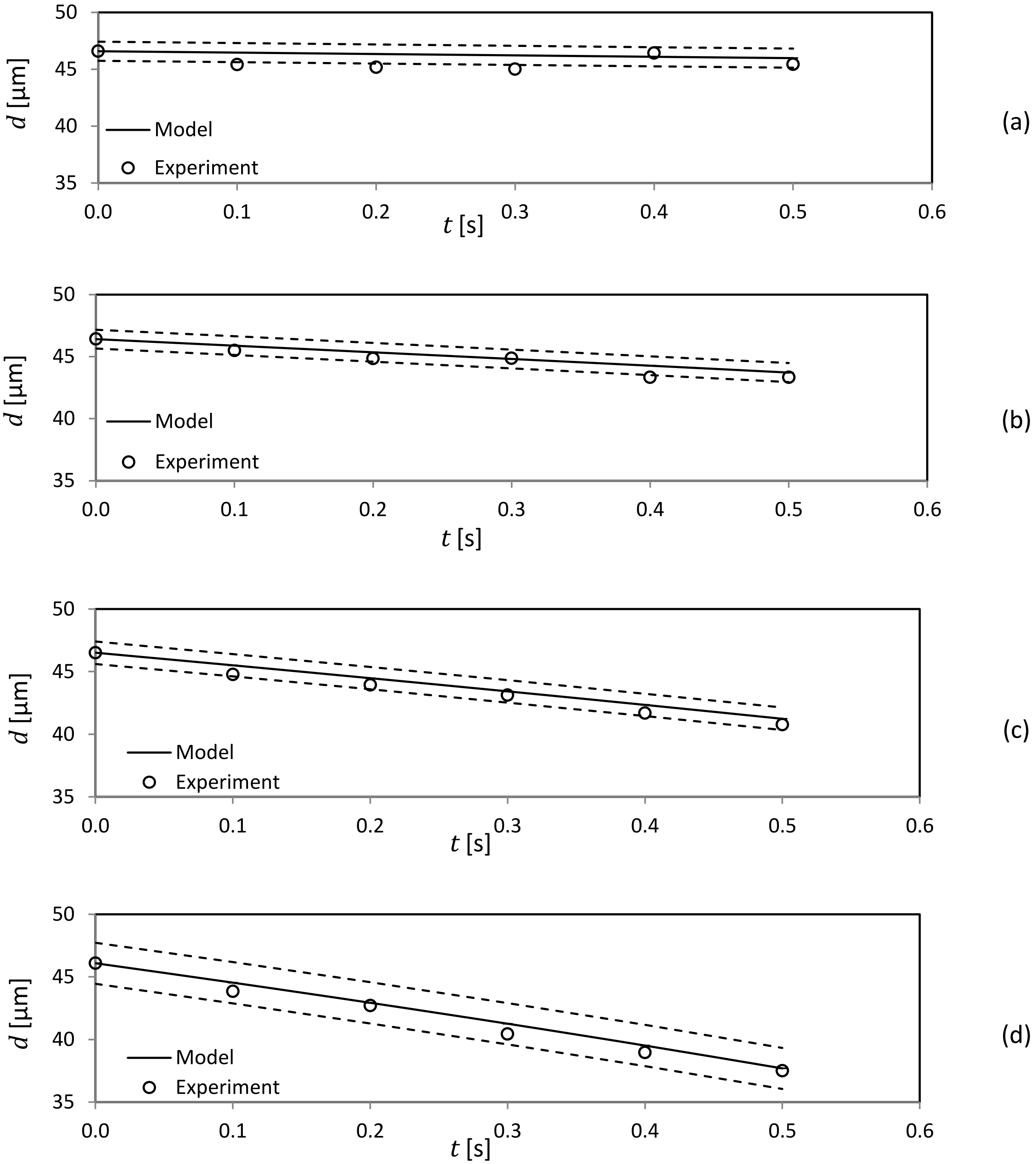

Figure 5.1: Comparison between the experimental and numerical model results for different conditions of relative humidity: (a) T_∞ = 24.8 °C and RH = 90% (S_{xy} = 0.85 µm); (b) T_∞ = 24.3 °C and RH = 60% (S_{xy} = 0.49 µm); (c) T_∞ = 24.5 °C and RH = 30% (S_{xy} = 0.50 µm); (d) T_∞ = 24.0 °C and RH = 0% (S_{xy} = 0.52 µm).

It can be observed in Figure 5.1(a) that the experimental and numerical results do not show a significant decrease in droplet size. For this case, the diameters measured experimentally at times $t = 0$s and $t = 0.5$s are $d = 46.6$ µm and $d = 45.4$ µm, respectively. This change in droplet size is approximately 1.2 µm, which is approximately equal to the value of the 95% confidence band, $2\sigma_d \cong$ 1.2 µm (see Appendix D for results). Thus, the total change in size in the complete observation period is of the same magnitude of the uncertainty in the initial droplet size. This is an inherent characteristic of the selected droplet generation system and is not dependent on the selected measuring technique. A higher rate of evaporation can be observed in Figures 5.1(b) and 5.1(c) for the cases of water droplets evaporating in air with relative humidity values of 60% and 30%, respectively. By comparing the reduction in droplet size shown in Figure 5.1(b) with the reduction in size shown in Figure 5.1(c) for the same time period, it can be observed that a reduction in the evaporation rate occurs when the relative humidity of the environmental air is increased, as expected.

Figure 5.1(d) shows the evolution in the droplet size with respect to time for the low RH case (0%). In this case, the increased rate of evaporation with respect to the high humidity case (90% RH) is higher than in the 30% and 60% RH cases, as expected. Additionally, if only the percentage of variation in diameter is considered, it can be observed that the difference in diameter variation between the 30% and 0% RH cases is higher than the difference in diameter variation between the 60% and 30% RH cases, which shows the effect of the relative humidity on the evaporation rate is not linear. In other words, assuming that two droplets with the same initial diameter were allowed to evaporate for the same time in two different RH environments, if the RH value of one of the environments is doubled with respect to the other, the percentage of change in the size of the droplet with the higher RH environment will be less than half of the of the percentage change in size of the droplet with the lower RH environment. This same effect was shown in Figure 4.9, in which the total evaporation time of droplets subjected to low amounts of infrared radiation were observed to increase exponentially with increasing values of relative humidity.

5.1.2 Influence of the air temperature

Two different experiments were performed to study the evolution of the size of pure water droplets in dry air. Figure 5.2 shows the evolution of droplet diameter with respect to time for two different dry air temperatures of 19.8 °C and 60 °C.

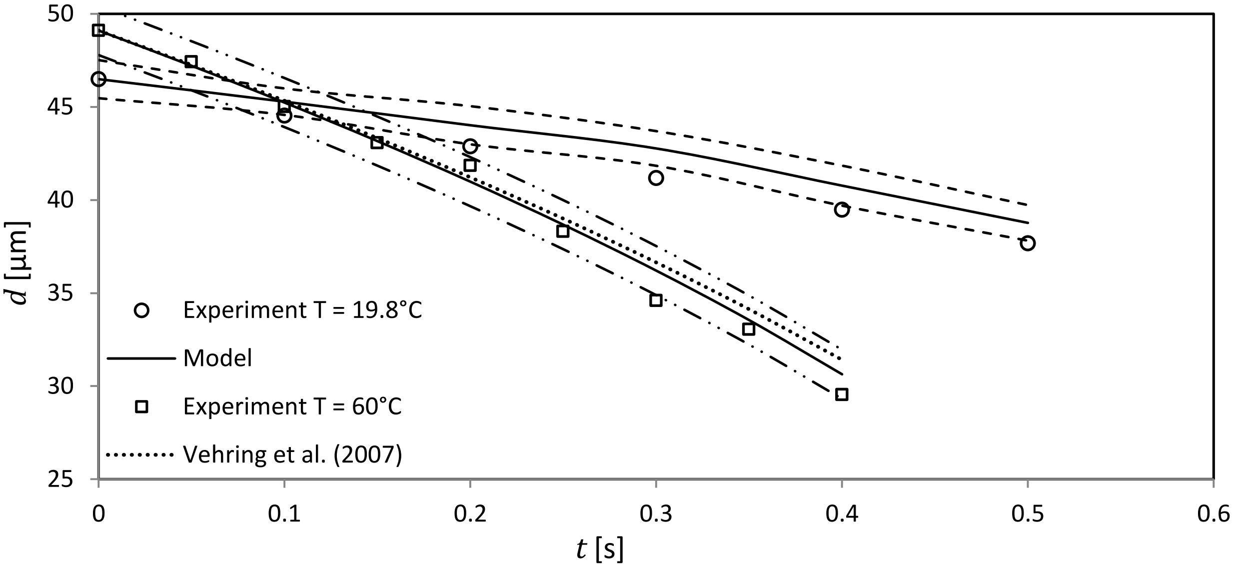

Figure 5.2: Comparison between the experimental and numerical model results for different conditions of air temperature (T = 19.8°C with S_{xy} = 1.11 µm, and T = 60°C with S_{xy} = 0.75 µm) and 0% relative humidity.

It can be observed in Figure 5.2, in the case of the low temperature experimental data, a reduction in the average diameter from 46.49 µm to 37.67 µm in a total time of 0.5 seconds. This represents a reduction in diameter, surface area and volume of approximately 19%, 34%, and 47%, respectively, with respect to the initial values. In the figure, the experimental data points are generally lower than the model, although most points are within the 95% confidence band of the initial droplet size.

A more substantial change in droplet size can be observed when the temperature of the surrounding air is higher (*i.e.*, $T_\infty = 60$ °C). There is an observed variation of droplet diameter from 49.09 µm to 29.53 µm in 0.5 seconds (experimental data). This change in size represents a reduction of the diameter, surface area and volume of approximately 40%, 64% and 78%, respectively. This is due to the effect of the increased heat transfer from the gas/water vapor phase to the liquid phase of the droplet, in which a higher surface temperature of the liquid surface will be achieved, and thus a higher vapor concentration gradient is created. Unlike the low temperature case, it can be observed that the experimental data points in the high temperature case are more sparsely distributed in the confidence band, with the majority of the data points located inside the band. Thus, it can be concluded that the experimental data and the predicted results have good agreement.

Figure 5.2 also shows the comparison between the experiment results obtained in this study and the analytical results obtained by Vehring *et al*. (2007) for the case of the steady-state evaporation of pure water droplets in dry air and environmental temperatures of 20 °C and 60 °C, respectively. The analytical model proposed by these investigators was based in the steady-state evaporation equation developed by Fuchs (1959), which included the effects of Stefan flow and assumed that the evaporation was driven merely by a concentration gradient. Other assumptions that were included in the current investigation, such as the gas phase behaving as an ideal gas, the radial symmetry of the control volume, and the material properties evaluated at a reference temperature and vapor mass fraction (*1/3 rule*) were also accounted by Vehring *et al*. (2007). In the figure, the results obtained by Vehring *et al.*(2007) are shown for both low and high temperature cases, however, a small difference between these results and the numerical model predictions obtained in the current study can be observed only in the high temperature case (*i.e.*, $T_\infty = 60$ °C). A good agreement can be observed between the experimental and model results, which validates the numerical model developed in the present investigation for the case of droplet evaporation under the steady state assumptions, without the effects of Stefan flow and without incident radiation.

5.2 Evaporation of pure acetone droplets without infrared radiation

The numerical model allows the modification of the material properties in order to simulate the evaporation of single-component liquids different than water. Alcohols and ketones (*e.g.*, ethanol, acetone) are good substitutes for water due to their similar properties of viscosity and surface tension, thus, they are suitable substances for the droplet generator system used in the experiments. An advantage of using these substances to validate the model is that their high volatility under standard conditions of temperature and pressure results in an increase in the evaporation rate compared to pure water. It is assumed the air does not initially have any acetone vapor content, hence, it can be assumed that an RH = 0% case is present. Figure 5.3 shows a comparison between the numerical model predictions and experiments regarding the evolution of the size of pure acetone droplets with respect to time.

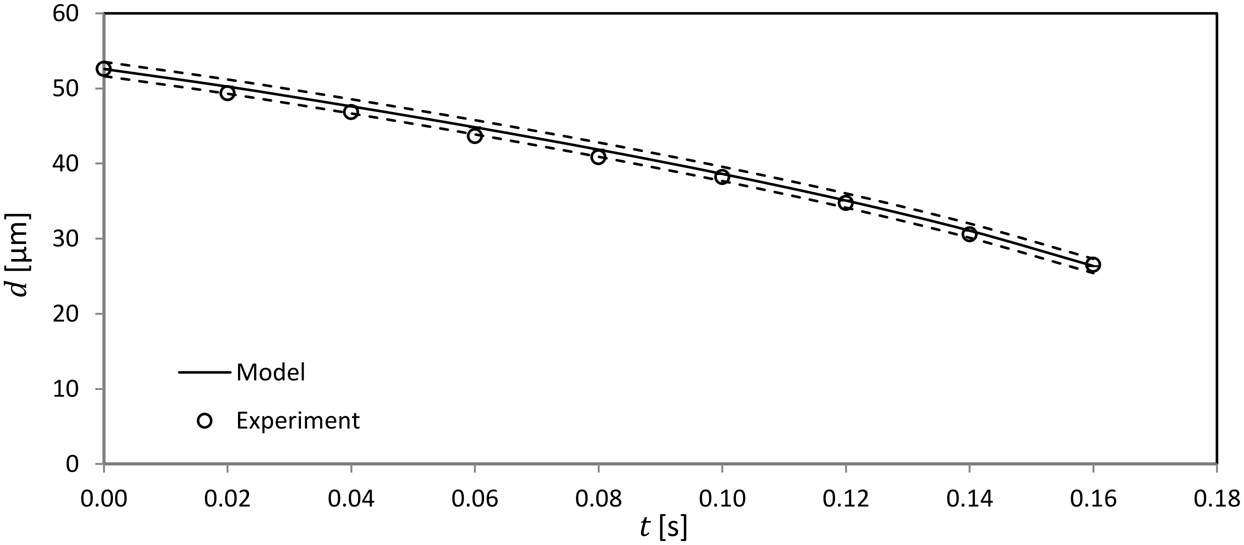

Figure 5.3: Comparison between the experimental and numerical model results for acetone droplets, with an air temperature of 19.5 °C and 0% relative humidity (S_{xy} = 0.69 µm).

Due to the difference in the surface tension and viscosity of acetone compared to pure water, the initial droplets are produced at a larger diameter. It can be observed from Figure 5.3 that the first measured droplet (*i.e.*, the droplet image recorded at a delay time equal to 0.02 seconds after the generator’s pulse occurred) has a diameter of 52.6 µm, which is approximately 7 µm larger than the average initial size of the initial diameter for the cases of pure water. From the results it can be observed that the evaporation rate of acetone droplets is significantly greater than the evaporation rate of pure water droplets in the same conditions of relative humidity, as is expected. More importantly, since a good agreement exists between the experiments and the predicted results, it can be concluded that the numerical model is suitable for pure liquid substances different than water.

5.3 Evaporation of pure water droplets subjected to infrared radiation

Predicted results show that the evaporation rate of liquid droplets increases (with respect to the case of no added radiation) when an external energy source, such as infrared radiation, is added to the energy balance in the liquid phase of the droplet, as it was shown in Chapter 4. Increasing amounts of radiation heat intensity (in units of power per unit area) are expected to increase the evaporation rate; however, the selected infrared laser is only capable of producing a single power output at the desired wavelength of 2.8 µm. Thus experiments are performed at only one laser power.

5.3.1 Influence of laser intensity on the evaporation of water droplets

Figure 5.4 shows the comparison between the experimental results (symbols) and the numerical model predictions (continuous lines) for the size evolution of water droplets subjected to an infrared radiation laser beam with a total measured power of 2.45 Watts and environmental conditions of 0% relative humidity, and 24.0 °C air temperature. In this case and the other cases shown by Figure 5.5, the total integrated power of the laser beam was measured by a power meter (Model FieldMaxII-P, Coherent Inc.) before the beam was reflected upwards to the flow tube by the gold-coated mirror (Model NB1-L01, Thorlabs Inc.). Since the mirror had a total reflectivity of approximately 95% at a wavelength of 2.8 µm, a factor of 0.95

was multiplied by the measured value of the power in every case, thus, the total power reported in Figure 5.4 is 2.33 Watts.

A limitation of this experiment is created by the Gaussian profile of the laser beam, in which the intensity distribution is not constant across the cross-sectional area of the beam. Since there is not an accurate mechanism to know the exact position of the droplets across the cross-sectional area of the laser beam, the total incoming radiation power into the droplets is unknown. In the results shown below, two different simulations were made in the numerical model to show the evolution of the droplet diameter with respect to time with two different radiation intensities: 100%, and 0% of the peak laser intensity. These values were selected to coincide with the magnitudes of the radiation intensities of the laser beam at its peak (approximately 368 mW/mm^2 for a beam with a total integrated power of 2.33 Watts, as it is shown in Appendix E) and for the case of no incident radiation, respectively. Therefore, the experimental data points are expected to be between these intensity limits. Additionally, a third simulation case, where the total intensity was 55% of the laser peak power (approximately 200 mW/mm^2 for a beam with a total integrated power of 2.33 Watts), was included in the 0% RH case shown in Figure 5.4. This radiation intensity provided the best fit between the numerical model and the experimental results.

For the numerical simulations shown in Figures 5.5(a), 5.5(b), 5.5(c) and 5.5(d), the numerical results that correspond to 0% and 100% of the peak intensity of the laser were not included, however, for every case, the numerical model results were calculated with a percentage of the peak intensity of the laser beam of 55%, which showed a good agreement between the model and the experiments. Each simulation curve shown in the figures below was generated using the same procedure of the cases without IR radiation, including the 95% confidence band of the initial droplet size (dotted and dashed lines) above and below the continuous line.

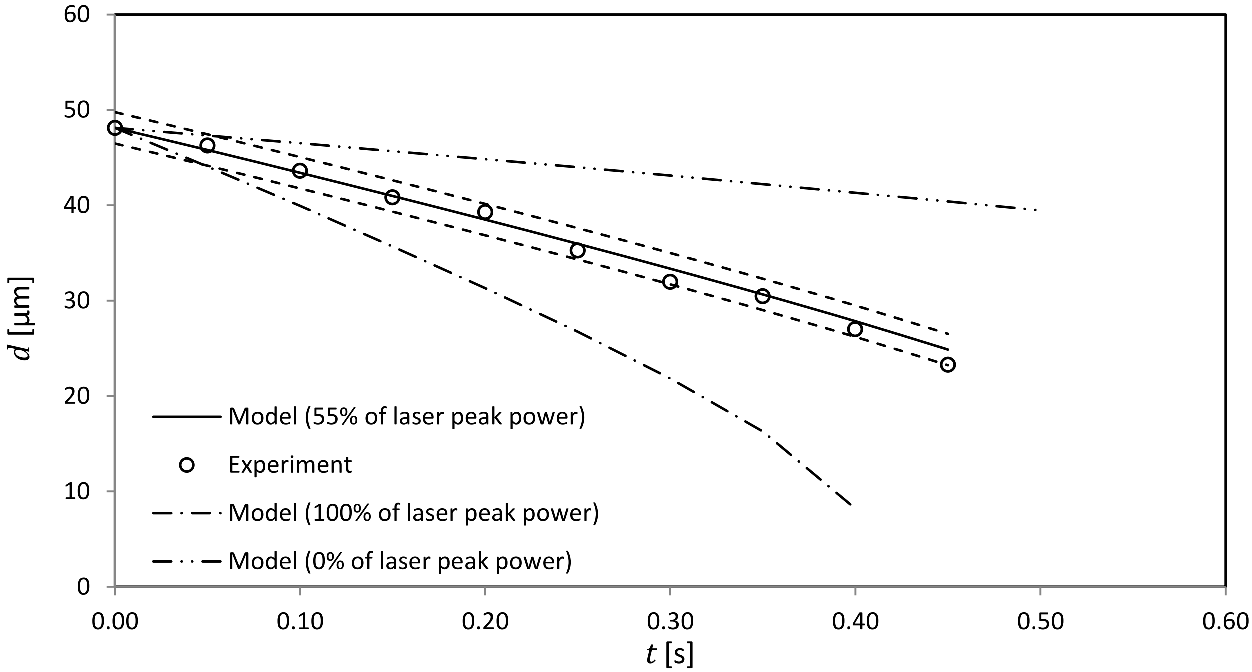

Figure 5.4: Comparison between the experimental and numerical model results for water droplets subject to infrared radiation with an air temperature of 24.0 °C, 0% relative humidity and 2.33 Watts of total IR laser beam power (S_{xy} = 0.81 µm).

The initial and final diameters measured experimentally are 48.12 µm and 23.27 µm, respectively. This observed reduction in droplet diameter represents a percentage of change in diameter, surface area and volume of 52%, 77%, and 89%, respectively. When these results are compared with the results shown in Figure 5.1(d) for the case of water droplets evaporating in air at room temperature, 0% RH and no incident radiation (*i.e.,* a percentage of change in diameter, surface area and volume of 19%, 34%, and 47%, respectively), it is evident that the incoming radiation increased the evaporation rate substantially. It can be observed that the experimental points are located in the area that is formed between the 0% and 100% peak power cases, which is consistent with the fact that the droplets are being hit by the laser beam. Since the experimental data points are located closer to the model curve case with incoming radiation intensity equal to 55%, two possible explanations may arise: (a) the droplet chain was not located in the middle of the cross-sectional area of the laser beam (assuming both were vertically aligned and parallel to each other) during the experiment but closer to the edge, specifically closer to a zone where the power intensity is equal to approximately half of the peak power, as it can be observed in Figure 3.6; or (b) the laser beam was not aligned and thus the droplets only traversed part of the profile. To achieve a perfect alignment between the vertical droplet chain and the laser beam is a rather difficult task, and thus it is difficult to obtain results closer to the 100% peak power model curve, nevertheless, the results show that the change in size, surface area and volume of the droplets is more than twice than the case without incident radiation.

5.3.2 Influence of infrared radiation on the evaporation of water droplets in a high relative humidity environment

Figure 5.5 shows the comparison between the experimental and model results for the cases of environmental conditions of relative humidity equal to 0%, 30%, 60% and 90%. Air temperatures of 24.0 °C, 24.6 °C, 23.7 °C and 24.3 °C, respectively, were recorded for each experiment and the droplets were illuminated by the infrared laser beam with a total integrated power in the range between 1.91 and 2.37 Watts. Since a constant value of the laser power could not be obtained, the numerical model curves were normalized with respect to the total power measured by the power meter in each experiment. The beam power distribution curve shown in Appendix E was used as a reference to obtain the adequate value of the intensity for each experiment based on a constant beam peak percentage of 55%.

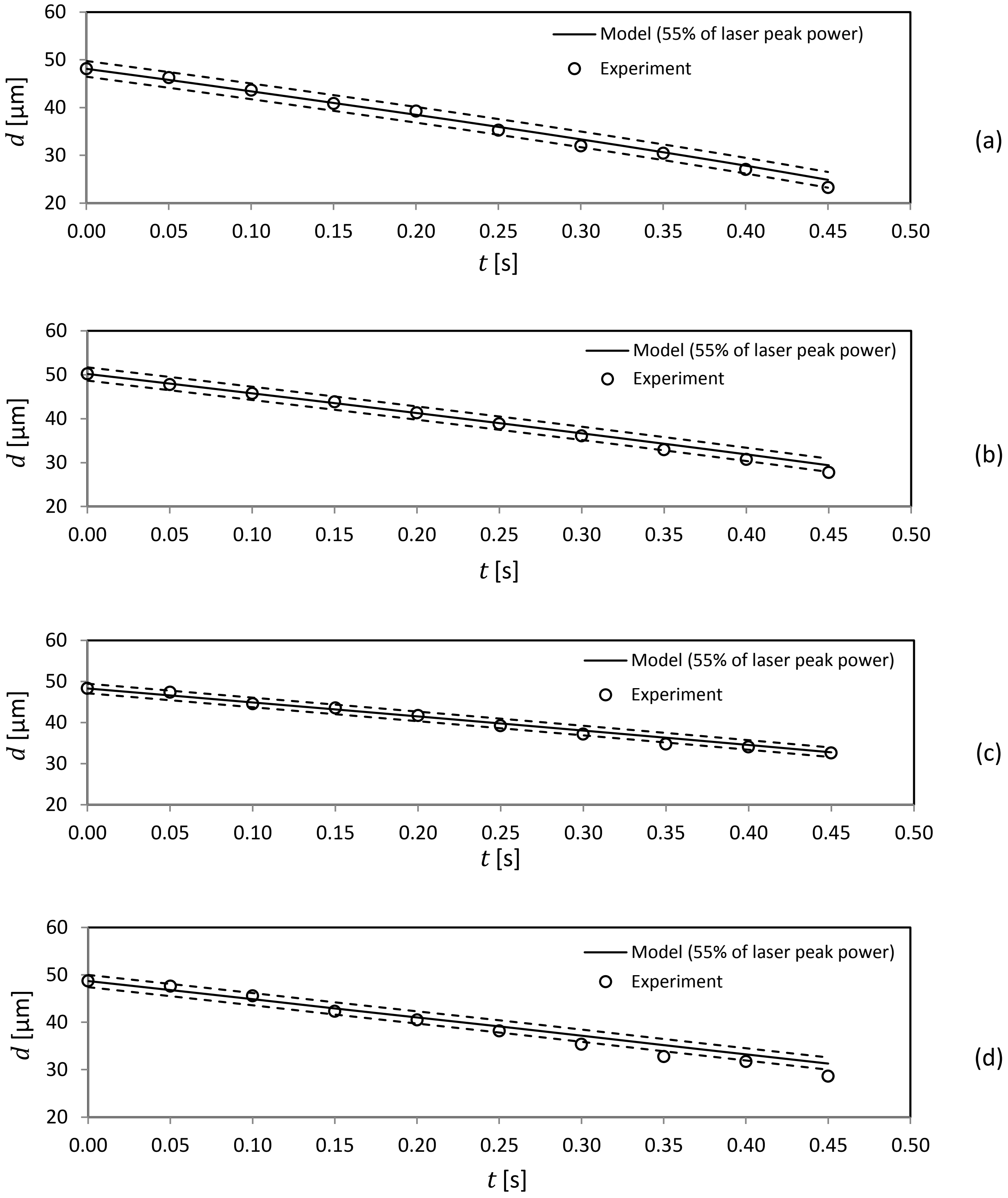

Figure 5.5: Comparison between the experimental and numerical model results for water droplets subject to infrared radiation and different conditions of relative humidity: (a) T_∞ = 24.0 °C, RH = 0%, Power = 2.33 W, S_{xy} = 0.81 µm; (b) T_∞ = 24.6 °C, RH = 30%, Power = 2.33 W, S_{xy} = 0.81 µm; (c) T_∞ = 23.7 °C, RH = 60%, Power = 1.91 W, S_{xy} = 0.67 µm; (d) T_∞ = 24.3 °C, RH = 90%, Power = 2.37 W, S_{xy} = 0.65 µm.

In the 30% and 60% cases, a similar behavior to the one shown by Figure 5.5(a) can be observed between the experimental and numerical results, as it is shown by Figures 5.5(b) and 5.5(c) respectively. However, a decrease in the size change percentage for the same period of time can be observed with increasing relative humidity. In section 4.1.4 of Chapter 4 it was shown that the influence of the relative humidity upon the droplet evaporation rate is diminished with the presence of high amounts of infrared radiation, thus it is expected that the change percentages of the droplet diameter for the different cases of RH do not have a difference of more than 10% between them. Finally, the comparison between the numerical model results and the experimental results for the case of high relative humidity (*i.e.*, RH = 90%) and incident infrared radiation are shown in Figure 5.5(d). A close agreement between the experiment and the numerical model curve with a laser power density of 55% of the peak power can be observed. The difference between the first (48.7 μm) and the last (28.6 μm) droplet diameter recorded with a period of 0.45 seconds represents a decrease in size of 41.3%. By comparing this result with the decrease in size for the cases with 0% RH and 30% RH, for whom the size changes were 52% and 44.8%, respectively (for similar conditions of temperature and radiation power), it can be concluded that in the presence of infrared radiation the relative humidity of the air still influences the evaporation rate of the droplets (i.e., the evaporation rate decreases with increasing RH) but to a significantly lesser extent than the case without radiation.

Chapter 6

Conclusions and Future work

This work investigated the effects of infrared radiation, temperature and relative humidity on the evaporation rate of isolated, quiescent, single-component liquid droplets in the range between 10 µm and 50 µm immersed in air. To predict the size evolution of the droplets under different humidities and different radiation intensities, a computationally inexpensive numerical model was developed, including some physical considerations (*i.e.*, modelling assumptions) such as steady-state diffusive evaporation, spherical symmetry, no internal circulation inside the liquid phase, no temperature gradients inside the liquid phase, no pressure gradients in the gas phase, constant radiation intensity and no Stefan flow effects, among others.

To validate the numerical model, a series of experiments were performed in an opto-mechanical rig that consisted of a vertical glass flow tube fed by an air stream (with various conditions of relative humidity, temperature and velocity) and a piezo-electric microdroplet generator capable of producing a chain of droplets with an approximate initial diameter of 50 µm and various frequencies. An infrared laser beam with a total integrated power of approximately 2.5 Watts at a wavelength of 2.8 µm was used to illuminate the vertical droplet chain from the bottom of the flow tube in order to increase the evaporation rate of the droplets under different conditions of relative humidity (spanning 0% to 90%). The droplet size was recorded at different positions across the optical window of the flow tube using a high magnification camera system and the shadowgraphy technique.

The experimental and numerical results showed a good correspondence in all cases, which validates the applicability of the model and the assumptions. Moreover, the selected measurement technique showed to be accurate and reliable for the studied size range (*i.e.*, the systematic error in using shadowgraphy becomes large for diameters below 10 µm). To summarize, individual conclusions will be presented and discussed below:

- In the studied cases without incident radiation, the evaporation rate of the water droplets decreased with increasing values of relative humidity of the surrounding air in a non-linear fashion. An increased relative humidity of the environment resulted in a lower difference between the vapor mass concentrations of the droplet surface and the far field (infinity), which is the driving force for evaporation.

- Experiments were performed to study the size evolution of water droplets on a dry environment (*i.e.*, 0% RH) and two different surrounding gas temperatures (*i.e.*, 20°C and 60 °C) and the results were compared with experimental data from the literature, showing good agreement. An increase of the temperature of the surrounding air was observed to increase the rate of evaporation. The increased temperature of the droplet’s surface due to the heat conducted from the gas phase to the liquid phase results in an increase of the vapor pressure at the surface, hence, the vapor mass concentration is increased and the driving force for evaporation is higher than the lower far-field temperature cases.

- Infrared radiation was observed to increase the evaporation rate for all the different relative humidity cases studied. For radiation intensities larger than 100 $\frac{\mathrm{mW}}{\mathrm{mm}^2}$, the effect of relative humidity on the evaporation rate is difficult to observe since the surface temperature of the droplets is increased significantly and the vapor mass concentration differences does not drop because droplet’s temperature is sustained by the incoming radiation. The experiments showed no significant difference between the evaporation rates of droplets in 0%, 30%, 60% and 90% relative humidity air conditions for an incident laser radiation intensity of approximately 200 $\frac{\mathrm{mW}}{\mathrm{mm}^2}$. Additionally, the droplets subjected to an incident laser radiation intensity of approximately 200 $\frac{\mathrm{mW}}{\mathrm{mm}^2}$ and room temperature (independently of the RH) were observed to evaporate with an evaporation rate that is similar to the evaporation rate of water droplets in dry air and $T_\infty = 60$ °C.

- The initial modeling assumptions appear to have captured the necessary physics to correctly predict the studied size range of the droplets. It is of particular interest that the assumption of neglecting the Stefan flow effects did not affect the validity of the model under the studied conditions. However, the validity of this model remains untested for a size range different than 10 µm - 50 µm.

Therefore, it can be concluded that the numerical model developed in this work offers a simple and computationally low-cost alternative to existing models for predicting the size evolution of single-component liquid droplets with a good accuracy under the studied conditions; however, some limitations may arise. A series of recommendations are listed below for future investigation:

- Experiments were performed for pure substances other than water (*e.g.*, acetone) and the model showed to be valid with the only requirement of estimating correctly the material properties (density, thermal conductivity, diffusivity, latent heat of vaporization, and specific heats) with respect to temperature and the spectral properties (absorptivity, reflectivity, and transmissivity) as a function of wavelength. However, the effects of temperature and radiation on the evaporation rate of acetone droplets were not tested experimentally. It is proposed that these effects are investigated for this and other substances, such as alcohols and fuels.

- In gas flaring devices, a common substance that is present in the gas stream in the form of microdroplets is salt water (NaCl + H_2O). Although the numerical model was developed for pure substances in air, a modification of the species conservation equation to allow the existence of 3 species (*i.e.*, water, salt and methane) would result in a model suitable to study the size evolution of these particles with respect to time for different conditions of relative humidity and radiation. However, new modelling considerations should also be included to study the last phase of the droplet life, where the water is completely evaporated and salt crystallization occurs.

- Some limitations were present in the experiments due to the characteristics of the instruments and rig used. Among these limitations were: (a) the uncertainty of the initial droplet diameter, (b) the limited length of the visualization window, and (c) the uncertainty of the droplet location in the laser beam profile. It is recommended for future works that: (a) two imaging systems (*i.e.*, sensor, lens and light source) are installed and operated simultaneously in order to record the images of the same falling droplet at the top (fixed) and the bottom (variable positions) of the flow tube and thus decrease the uncertainty of each measurement; (b) the length of the optical window must be increased in order to observe a larger variation in the droplet diameter, especially at high relative humidities and no radiation intensities; (c) a rigorous method to ensure the correct alignment between the laser beam and the vertical droplet chain is applied, such that droplets are located in the center of the beam profile.

- The numerical model is believed to be invalid for droplet sizes below 10 micrometers due to different effects, such as the Kelvin effect, and the light scattering effects described by Mie theory for particles with a size parameter close to 1. It is recommended that these effects are considered in the model if a size range below 10 μm is investigated.

References

Abramzon, B., Sirignano, W.A. (1989). Droplet vaporization model for spray combustion calculations. *International Journal of Heat and Mass Transfer, 32*(9), 1605-18.

Argos Laser technical information. (n.d.). Retrieved February 2014, from http://www.lockheedmartin.com/us/products/aculight/argos.html

Baldelli, A., Boraey, M. A., Nobes, D. S., Olfert, J. S., & Vehring, R. (2014). Theoretical model validation of a solution droplet evaporation process, from the generation, through the shell formation to the collection of the dried particle. *Not published yet*.

Beckwith, T. G., Maragoni, R. D., & Lienhard, J. H. (2007). *Mechanical measurements* (Vol. Sixth Edition). Pearson Education.

Cengel, Y., & Ghajar, A. (1998). *Heat and Mass Transfer, fundamentals and applications* (4th ed.).

Cunningham, E. (1911). On the velocity of steady fall of spherical particles through fluid medium. *Proc. Roy. Soc. A*, 83-357.

Dukowicz, J. K. (1980). A particle-fluid numerical model for liquid sprays. *Journal of Computational Physics, 35*(2), 229-253.

Ermachenko, V. M., & Rubezhnyi, Y. G. (1976). Droplet evaporation under radiation II. *Zh. tekk. Fiz., 46*, 31 – 36.

Faghri, A., & Zhang, Y. (2006). *Transport Phenomena in Multiphase Systems.* Burlington, MA.: Elsevier.

Faghri, A., Zhang, Y., & Howell, J. R. (2010). *Advanced Heat and Mass Transfer.* Columbia, MO.: Global Digital Press.

Feingold, A. (1978). A new look at radiation configuration factors between disks. *J. Heat Transfer, 100*, 742-744.

Finlay, W. H. (2001). *The Mechanics of Inhaled Pharmaceutical Aerosols.* Edmonton, Canada.

Foss, W. R., & Davis, E. J. (1996). Transient laser heating of single solid microspheres. *Chemical Engineering Communications*, 152-153:1, 113-138.

Frackowiak, B. (2010). Numerical analysis of the interactions between evaporating droplets in a monodisperse stream. *International journal of heat and mass transfer, 53*(7), 1392-1401.

Fuchs, N. A. (1959). *Evaporation and droplet groth in gaseous media.* Pergamon Press Ltd.

Gaydon, A. G. (1974). *The spectroscopy of Flames.*

Ghaemi, S., Rahimi, P., & Nobes, D. S. (2008). Effect of gas-liquid ratio on droplets centricity and velocity of an effervescent atomizer. *American Society of Mechanical Engineering Fluid Engineering Conf.* Jacksonville.

Ghaemi, S., Rahimi, P., & Nobes, D. S. (2008). Measurement of droplet centricity and velocity in the spray field of an effervescent atomizer. *14th Int. Symp. On Application of Laser Techniques to Fluid Mechanics.* Lisbon.

Ghaemi, S., Rahimi, P., & Nobes, D. S. (2010). Effect of bubble generation characteristics on effervescent atomization at low gas-liquid ratio operation. *Atomization and Sprays, 20*(3), 211–225.

Gomez, J., Fleck, B., Olfert, J., & McMillan, J. (2011). Influence of two-phase feed bubble size on effervescent atomization in a horizontal nozzle assembly. *Atomization and Sprays, 21*(3), 249-261.

Hale, G. M., & Querry, M. R. (1973). Optical constants of water in the 200nm to 200µm wavelength region. *Applied Optics, 12*, 555-563.

Harpole, G. M. (1980). Radiative absorption by evaporating droplets. *Int. Journal of Heat and Mass Transfer, 23*(1), 17 – 26.

Hinds, W. C. (1998). *Aerosol Technology: Properties, Behaviour and Measurement of Airborne Particles* (2nd ed.). John Wiley & Sons, Inc.

Hubbard, G. L., Denny, V. E., & Mills, A. F. (1975). Droplet evaporation: Effects of transients and variable properties. *International Journal of Heat and Mass Transfer, 18*, 1003-1008.

Incropera, F. P., & DeWitt, D. P. (1996). *Introduction to Heat Transfer* (3rd ed.).

Ivanov, E. V., & Korovin, V. Y. (1978). Water droplet evaporation in the field of continuous CO2 laser radiation. *Journal of Engineering Physics, 34*, 807 – 812.

Jennings, S. G. (1988). The Mean Free Path in Air. *Journal of Aerosol Sciences, 19*(2), 159 – 166.

Kashdan, J. T., Shrimpton, J. S., & Whybrew, A. (2007). A digital image analysis technique for quantitative characterization of high speed sprays. *Opt. Lasers Eng., 45*, 106-115.

Kashdan, J., Shimpton, J., & Whybrew, A. (2007). A digital image analysis technique for quantitative characterisation of high speed sprays. *Optics and Lasers in Engineering, 45*, 106-115.

Kee, R. J., Coltrin, M. E., & Glarborg, P. (2003). *Chemically Reacting Flow* (1st ed.).

Keene, H. B. (1913). Calculation of the energy exchange between two fully radiative coaxial circular apertures at different temperatures. *Proc. Roy. Soc.*, *LXXXVIII-A*, pp. 59-60.

Kim, J., & Lee, S. (2001). Dependence of spraying performance on the internal flow pattern in effervescent. *Atomization and Sprays, 11*, 735-756.

Kincaid, D., & Longley, T. (1989). A water droplet evaporation and temperature model. *Transaction of the ASAE, 32*(2), 457-463.

Kostiuk, L. W., Wilson, D., Ackerman, M., Checkel, D., & Dale, D. (2004). *Flare Research Project Final Report.* University of Alberta, Edmonton, Canada.

Lorenzini, G., & Saro, O. (2013). Thermal fluid dynamic modelling of a water droplet evaporating in air. *International Journal of Heat and Mass Transfer, 62*, 323-335.

Maqua, C. (2008). Monodisperse droplet heating and evaporation: Experimental study and modelling. *International journal of heat and mass transfer, 51*(15), 3932-3945.

Marrero, T. R., & Mason, E. A. (1972). Gaseous diffusion coefficients. *Journal of Physical and Chemical Reference Data, 1*, 3-118.

Maxwell, J. C. (1877). Diffusion. *Encyclopedia Britanica, VII*(9th), 214-221.

Miller, R., Harstad, K., & Bellan, J. (1998). Evaluation of equilibrium and non-equilibrium evaporation models for many-droplet gas-liquid flow simulations. *International Journal of Multiphase Flow, 24*(6), 1025-1055.

Miliauskas, G., & Sabanas, V. (2006). Interaction of transfer processes during unsteady evaporation of water droplets. *International Journal of Heat and Mass Transfer, 49*, 1790-1803.

Modest, M. (2003). *Radiative Heat Transfer* (2nd ed.).

Monazam, E. R., & Maloney, D. J. (1992). Temperature transients associated with pulsed heating of single particles. *Journal of Applied Physics, 71*, 2552.

Mulholland, J., Srivastava, R., & Wendt, J. (1988). Influence of droplet spacing on drag coefficient in nonevaporating, monodisperse streams. *AIAA journal, 26*(10), 1231-1237.

Oberdier, L. (1984). Instrumentation system to automate the analysis of fuel-spray images using computer vision. *ASTM Special Technical Publication*, 123-136.

Penzias, G. J. (1968). Spectral radiation measurements on P.F. flames at I.F.R.F. *IJ Muiden Private communication.*

Plyler, E. K., & Humphreys, C. J. (1948). Infrared Emission Spectra of Flames. *Journal of Research of the National Bureau of Standards, 40*.

Podczeck, F., Rahman, S., & Newton, J. (1999). Evaluation of a standardised procedure to assess the shape of pellets using image analysis. *Int J of Pharmaceutics, 192*, 123-138.

Pustovalov, V. K. (1977). The effect of optical constants on the process of diffusional evaporation of a droplet exposed to radiation. *Izv. Akad. Nauk SSSR, Fiz. Atm. Okeana, 13*, 1311 – 1314.

Pustovalov, V. K., & Romanov, G. (1977). Diffusional evaporation of a droplet on exposure to monochromatic radiation. *Kvant. Elektr., 4*, 84 -94.

Pustovalov, V. K., & Romanov, G. (1983). The theory of heating and evaporation and evaporation of a spherical particle exposed to optical radiation. *Int. Journal of Heat and Mass Transfer, 23*, 17 – 26.

Ranz, W. E., & Marshall, W. R. (1952). Evaporation from Drops. *Chem. Eng. Prog., 48*, 141-173.

Romanov, G., & Pustovalov, V. K. (1973). Heating and evaporation of a spherical particle on exposure to monochromatic radiation. *Zk. tekh. Fir, 43*, 2163 – 2168.

Rosell-Llompart, J., & Fernandez de La Mora, J. (1994). Generation of monodisperse droplets 0.3 to 4 μm in diameter from electrified cone-jets of highly conducting and viscous liquids. *Journal of Aerosol Science, 25*(6), 1093-1119.

Sazhin, S. (2005). New approaches to numerical modelling of droplet transient heating and evaporation. *International journal of heat and mass transfer, 48*(19), 4215-4228.

Sazhin, S. S. (2006). Advanced model of fuel droplet heating and evaporation. *Progress in Energy Combustion Sciences, 32*, 162-214.

Segelstein, D. (1981). *The Complex Refractive Index of Water.* M.Sc. Thesis, University of Missouri, Kansas City.

Shekunov, B. (2007). Particle size analysis in pharmaceutics: principles, methods and applications. *Pharmaceutical research, 24*(2), 203-227.

Simmons, H. (1977). The correlation of drop size distribution in fuel nozzle sprays part I: the dropsize/volume-fraction distribution. *Trans. ASME J. Engineering for Power, 99*, 309-314.

Simmons, H. C. (1977). The correlation of drop size distribution in fuel nozzle sprays, Part I: The drop-size/volume-fraction distribution. *Trans ASME J. Eng. Power, 99*, 309-314.

Simmons, H. C. (1980). The prediction of Sauter mean diameter for gas turbine fuel nozzles of different types. *Trans ASME J. Eng. Power, 102*, 452-646.

Sirignano, W. A. (1983). Fuel droplet vaporization and spray combustion theory. *Prog. in Energy Combustion Sciences, 9*, 291-322.

Sirignano, W. A. (1999). *Fluid dynamics and transport of droplets and sprays*. Cambridge: Cambridge University Press.

Spjut, R. E., Sarofim, A. F., & Longwell, J. P. (1985). Laser heating and particle temperature measurement in an electrodynamic balance. *Langmuir, 1*, 355.

Strelkov, G. M. (1974). Diffusional evaporation of a water droplet in radiation field. *Kvant. Elektr., 2*, 459 -463.

Tritton, D. J. (1959). Experiments on the flow past a circular cylinder at low Reynolds numbers. *Journal of Fluid Mechanics, 6*(04), 547-567.

Tourin, R. H. (1966). Spectroscopic Gas Temperature Measurement. *Fuel and Energy Science Monograph, Elsevier*.

Tseng, C. C., & Viskanta, R. (2006). Enhancement of water droplet evaporation by radiation absorption. *Fire safety journal, 41*, 236-247.

Vdovin, Y., Ermachenko, V. M., & Rubezhnyi, Y. G. (1975). Droplet evaporation under radiation. *Zh. tekk. Fiz., 45*, 630 – 636.

Vehring, R. (2007). *Pharmaceutical Particle Engineering via Spray Drying.* Expert Review in Pharmaceutical Research.

Vehring, R., Foss, W., & Lechuga-Ballesteros, D. (2007). Particle formation in spray drying. *Journal of Aerosol Science, 38*, 728-749.

Vesala, T., Kukkonen, J., & Kulmala, M. (1989). *A model for evaporation of freely falling droplets.* Technical Report, NASA STI/Recon.

View factor of parallel disks. (n.d.). Retrieved July 2013, from http://www.engr.uky.edu/rtl/Catalog/sectionc/C-41.html

Viskanta, R., & Tseng, C. C. (2007). Spectral radiation characteristics of water sprays. *Combustion Theory and Modelling, 11*(1), 113-125.

Weeks, D. J. & Saunders, O. A. (1958). *J. Inst. Fuel, 31*, 247.

Weiss, B., Derov, P., DeBiase, D., & Simmons, H. (1984). Fluid particle sizing using a fully automated optical imaging system. *Optical Engineering, 23*, 561-566.

Widmann, J. F., & Davis, E. J. (1998). Pulsed electromagnetic heating of microparticles. *Int. Journal of Heat and Mass Transfer, 41*, 4195-4204.

Yalamov, Y. N., Shchukin, E. P., Kutukov, V. B., & Malyshev, V. A. (1977). Concerning the diffusional evaporation of droplets in the electromagnetic radiation field at arbitrary temperature differences. *Teplofiz. Vysok. Temp., 15*, 434 – 436.

Young, K., & Tomlinson, E. (1993). Microphysical effects of irradiating a fog with a 10.6-um CO2 laser. *Journal of the Atmospheric Sciences, 50*(7), 941-950.

Appendix A

Initial assumptions

A detailed explanation of the initial assumptions introduced in Chapter 2 is presented in this section:

1. Quasi-steady-state assumption

The use of the term “quasi-steady” in the present work means that a steady-state approach will be taken in order to describe the physics of a non-steady phenomenon. Without the addition of any external work (such as radiation) to the energy balance of the liquid droplet, the diffusion of vapor away from the droplet due to a difference in vapor mass concentration between the surface and the far-field environment can be considered constant for most of the droplet’s lifetime. In the initial stage of the droplet life, under standard conditions of temperature and pressure, a transient temperature change is expected to occur in order to reach the equilibrium evaporating temperature. For the case of a water droplet immersed in a dry air environment (*i.e.,* 0% relative humidity) and room temperature, the bulk temperature of the droplet will decrease to an equilibrium value that is analogous to the wet-bulb temperature of air at 0% relative humidity and atmospheric pressure. After the thermal equilibrium is reached, the value of the equilibrium temperature remains constant until the droplet evaporates completely. Since the temperature of the droplet affects directly the value of the vapor concentration in the surface, and thus the difference in vapor concentration, after reaching thermal equilibrium the evaporation rate can be considered constant. The amount of time required for this transient period is estimated to be low compared with the time required for complete evaporation;

therefore the transient analysis can be ignored. With the introduction of an external radiation term, the droplet will not reach a constant equilibrium temperature due to the constant addition of energy into the liquid bulk, thus, the evaporation cannot be considered constant. In the present model, a system of two second-order ordinary differential equations (*i.e.*, the conservation of energy and conservation of species equations) will be solved numerically in order to obtain a unique solution of temperature and mass flow rate in which the droplet can exist for given conditions of environmental temperature, relative humidity and incident radiation intensity. Subsequently, the droplet will be allowed to evaporate at the mass flow rate value obtained in the solution during a short period time (time step), and the process will be repeated until the size of the droplet is out of the interest range of the investigation.

2. Constant addition of radiative heat flux (mW/mm^2) into the liquid droplet (*i.e.*, the gas phase does not absorb radiation)

The estimation of the radiative heat transfer between two bodies introduces the following challenges: (a) The geometries of the bodies and their relative position with respect to each other must be known in order to apply the simple geometric models given by the view factor formulas, and (b) the spectral properties (*e.g.*, absorptivity, reflectivity, transmisivity) are dependent on the wavelength of the energy and average values cannot be used regularly.

In the numerical model, and later in the validation experiments, the assumption of a collimated energy beam with a single wavelength hitting the projected surface area of the droplet can overcome the two limitations introduced above. A wavelength of 2.8 μm in the infrared spectrum was determined to be the wavelength for the maximum absorption of liquid water. Similarly, at this wavelength the absorption of air and water vapor are assumed to be negligible.

3. Spherical coordinates, radial symmetry: Rate of changes and transport phenomena only in the radial direction (*i.e.*, Concentration of water vapor and Temperature of the gas are functions only of the coordinate "r" and do not depend on coordinates "θ" and "φ")

The effects of the internal circulation and the non-sphericity of the liquid droplets are not considered in this research. This was established to maintain a low level of computational effort in the model when solving the system of ordinary differential equations numerically. Thus, the droplet is assumed to be 100% spherical and the diffusion of vapor is assumed to be normal to its surface in every point.

4. There is no relative velocity between the droplet and the surrounding gas

This assumption states that the spherical droplet is either immersed in a complete stagnant fluid, motionless, or that the droplet is being carried by a flowing gas without any relative motion between their boundaries and the carrying fluid. A symmetrical vapor concentration gradient is created by assuming a motionless evaporating droplet with respect to the surrounding gas. In a more strict sense none of these statements are true; the spherical droplets have an absolute velocity that is equal to the sum of the gas velocity plus the settling velocity. The settling velocity of the droplets is the absolute velocity relative to an observer that moves with the carrying fluid.

The stagnant flow assumption can still be applied regardless of the relative motion between the gas and the droplets. In order to do this, the Sherwood number must be calculated. The Sherwood number (Sh) is defined as the ratio of convective mass transport over diffusive mass transport and is considered to be the mass transport analog dimensionless number of the Nusselt number (Nu). The Sherwood number of an evaporating solid or liquid particle surrounded by a fluid is defined as:

$$Sh = \frac{KLc}{D} \tag{A.1}$$

Where Lc is the characteristic length of the particle, D is the diffusivity and K is the mass transfer coefficient. Similarly to its thermal analog, Nu, some difficulty arises when estimating the value of Sh due to the uncertainty of the value of K. A good approach is to calculate the Sherwood number with empirical correlations based on well-known dimensionless numbers. A general correlation was developed by Ranz & Marshall (1952) for spheres:

$$Sh = A + B(Re)^n \,(Sc)^m \tag{A.2}$$

where Re and Sc are the Reynolds and Schmidt numbers, respectively, and:

$$A = 2$$

$$B = 0.6$$

$$n = 0.5$$

$$m = 0.333$$

The correlation shown in Eq. A.2 is the mass transfer analog correlation developed by Ranz and Marshall (1952) to estimate the value of the Nusselt number in terms of the Reynolds and Prandtl numbers that is shown in Eq. A.6. For spheres immersed in a stagnant flow, *i.e.,* $Re = 0$, the Sherwood number must be equal to 2.

5. The material properties: λ, c_p and D are assumed to be constant and evaluated at the droplet surface conditions

A review of the variation of the material properties of water vapor λ, c_p and D with respect to temperature (shown in Appendix B) can show that there are no significant changes in the temperature range of interest (298 K to 373 K). A rule of thumb introduced by Hubbard *et al.*, (1975) and later implemented by Vehring *et al.*, (2007) proposes the use of material properties that are evaluated at a temperature equal to one third of the difference between the surface and the infinite conditions. The “1/3 rule” was applied in all the numerical calculations of the present model and a good agreement between the numerical and experimental results was obtained.

6. There is no pressure gradient in the gas phase

The gas (air) inside the flow tube is maintained at a constant atmospheric pressure. It is assumed that there are no changes in total pressure in neither the radial direction nor the vertical direction inside the experimental flow tube. One advantage of neglecting any pressure gradient is the simplification of the ODE system due to the suppression of the momentum conservation equation.

7. There is no temperature gradient inside the droplet (*i.e.*, Bi << 1):

The model that was applied to verify this assumption was the lumped capacitance model for calculating the steady state temperature and time of a heating or cooling spherical droplet in ambient air. In order to apply this model, the Biot number must be much less than the unity. A good estimate (*i.e.,* error less than 10%) occurs when Bi < 0.1 (Incropera & DeWitt, 1996). The Biot number is a dimensionless number that states the ratio of heat transfer inside a bulk of material with respect to the heat transfer at its surface. A smaller Biot number means that the temperature of a material that is subject to heating or cooling will be uniformly distributed in a shorter period of time. The Biot number can be defined as:

$$Bi = \frac{hL_{\mathrm{c}}}{\lambda_{\mathrm{liquid}}} \tag{A.3}$$

where h represents the heat coefficient due to convection, λ is the thermal conductivity of the liquid and L_{c} is a characteristic length. The characteristic length is usually defined as the ratio between volume and surface area of the material experiencing the transient heating or cooling, thus:

$$L_{\mathrm{c}} = \frac{V}{A_{\mathrm{s}}} \tag{A.4}$$

where V is the total volume of the material and A_{s} is the surface area exposed to the heat transfer. Following this model, the characteristic length for spheres is the radius divided by 3, or $\frac{r}{3}$. Incropera (1985) recommends using the radius of the sphere as the characteristic length for a more conservative approach. The value of the convective heat coefficient can be calculated from the definition of the Nusselt number (Nu):

$$Nu = \frac{2\,h\,r}{\lambda_{\mathrm{vapor}}} \tag{A.5}$$

A good correlation for the estimation of the Nusselt number for spheres in cold flow was developed by Ranz and Marshall (1952):

$$Nu = A + B(Re)^n \, (Pr)^m \tag{A.6}$$

where Re and Pr are the Reynolds and Prandlt numbers, respectively, and:

$$A = 2$$

$$B = 0.6$$

$$n = 0.5$$

$$m = 0.333$$

Following assumption 4, if there is no relative motion between the surrounding gas and the droplet, then $Re = 0$ and $Nu = 2$. The value of the convective heat coefficient can be calculated from Eq. A.3:

$$h = \frac{\lambda_{\text{vapor}}}{r} \tag{A.7}$$

The material properties λ_{vapor} and λ_{liquid} are nearly constant in the temperature region of interest and therefore a considerable change in temperature won't change the values of the conductivity. Assuming a 50 µm water droplet with an initial bulk temperature of 300 K (28 °C), motionless with respect to a surrounding air at 298.15 K (25 °C) and subject to heat conduction and different rates of radiation, the values of λ_{vapor} , λ_{liquid} and h are:

$$\lambda_{\text{vapor}} = 0.018539165\ \frac{\text{W}}{\text{m K}}$$

$$\lambda_{\text{liquid}} = 0.620224843\ \frac{\text{W}}{\text{m K}}$$

$$h = 463.4791\ \frac{\text{W}}{\text{m}^2\ \text{K}}$$

The Biot number can be calculated using Eq. A1:

$$Bi = \frac{463.4791\ \frac{\text{W}}{\text{m}^2\ \text{K}}\frac{40\text{x}10^{-6}\text{m}}{3}}{0.620224843\ \frac{\text{W}}{\text{m K}}}$$

$$Bi = 0.01$$

which is less than 0.1 and the lumped capacitance model can be safely applied. By being conservative and using the radius of the droplet as the characteristic length we have:

$$Bi = 0.0299\ \cong 0.03 < 0.1$$

8. Kelvin effect due to small droplet radius is negligible.

The change of vapor pressure due to a small radius of curvature of the water droplet is considerable for diameters smaller than 10 μm; however, the region of interest of the present work will consider only diameters between 50 µm and 10 µm due to the technical difficulties in measuring droplets smaller than 10 µm with the proposed optical technique.

9. The particle radius is much larger than the mean free path of the surrounding gas – continuum theory applies.

A calculation of the mean free path of air at standard conditions of 20 °C, 100% RH and 101325 Pascals was reported by Jennings (1988), with a value of 65.48 nm. In the case of lower conditions of relative humidity, such as 0%, the mean free path reported value was 65.43 nm. The initial diameter of the water droplets is approximately 50 µm, which is approximately 3 orders of magnitude higher, hence continuum theory can be applied.

Appendix B

Properties of water vapor, acetone and air

Table B.1: Properties of water in liquid and vapor phase. Data retrieved from: Çengel & Ghajar, *Heat and Mass Transfer*, Fourth Edition, Table A-9, page 878.

T [°C]	T [K]	ρ_{liq} [kg/m³]	ρ_{vap} [kg/m³]	L [J/kg]	$c_{p_{\text{vap}}}$ [J/kg.K]	$c_{p_{\text{liq}}}$ [J/kg.K]	λ_{vap} [W/m.K]	λ_{liq} [W/m.K]	μ_{liq} [kg/m.s]
0.01	273.16	999.8	0.0048	2501000	1854	4217	0.0171	0.561	1.79E-03
5	278.15	999.9	0.0068	2490000	1857	4205	0.0173	0.571	1.52E-03
10	283.15	999.7	0.0094	2478000	1862	4194	0.0176	0.58	1.31E-03
15	288.15	999.1	0.0128	2466000	1863	4185	0.0179	0.589	1.14E-03
20	293.15	998	0.0173	2454000	1867	4182	0.0182	0.598	1.00E-03
25	298.15	997	0.0231	2442000	1870	4180	0.0186	0.607	8.91E-04
30	303.15	996	0.0304	2431000	1875	4178	0.0189	0.615	7.98E-04
35	308.15	994	0.0397	2419000	1880	4178	0.0192	0.623	7.20E-04
40	313.15	992.1	0.0512	2407000	1885	4179	0.0196	0.631	6.53E-04
45	318.15	990.1	0.0655	2395000	1892	4180	0.02	0.637	5.96E-04
50	323.15	988.1	0.0831	2383000	1900	4181	0.0204	0.644	5.47E-04
55	328.15	985.2	0.1045	2371000	1908	4183	0.0208	0.649	5.04E-04
60	333.15	983.3	0.1304	2359000	1916	4185	0.0212	0.654	4.67E-04
65	338.15	980.4	0.1614	2346000	1926	4187	0.0216	0.659	4.33E-04
70	343.15	977.5	0.1983	2334000	1936	4190	0.0221	0.663	4.04E-04
75	348.15	974.7	0.2421	2321000	1948	4193	0.0225	0.667	3.78E-04
80	353.15	971.8	0.2935	2309000	1962	4197	0.023	0.67	3.55E-04
85	358.15	968.1	0.3536	2296000	1977	4201	0.0235	0.673	3.33E-04
90	363.15	965.3	0.4235	2283000	1993	4206	0.024	0.675	3.15E-04
95	368.15	961.5	0.5045	2270000	2010	4212	0.0246	0.677	2.97E-04
100	373.15	957.9	0.5978	2257000	2029	4217	0.0251	0.679	2.82E-04
110	383.15	950.6	0.8263	2230000	2071	4229	0.0262	0.682	2.55E-04
120	393.15	943.4	1.121	2203000	2120	4244	0.0275	0.683	2.32E-04
130	403.15	934.6	1.496	2174000	2177	4263	0.0288	0.684	2.13E-04
140	413.15	921.7	1.965	2145000	2244	4286	0.0301	0.683	1.97E-04
150	423.15	916.6	2.546	2114000	2314	4311	0.0316	0.682	1.83E-04
160	433.15	907.4	3.256	2083000	2420	4340	0.0331	0.68	1.70E-04
170	443.15	897.7	4.119	2050000	2490	4370	0.0347	0.677	1.60E-04
180	453.15	887.3	5.153	2015000	2590	4410	0.0364	0.673	1.50E-04
190	463.15	876.4	6.388	1979000	2710	4460	0.0382	0.669	1.42E-04
200	473.15	864.3	7.852	1941000	2840	4500	0.0401	0.663	1.34E-04
220	493.15	840.3	11.6	1859000	3110	4610	0.0442	0.65	1.22E-04
240	513.15	813.7	16.73	1767000	3520	4760	0.0487	0.632	1.11E-04
260	533.15	783.7	23.69	1663000	4070	4970	0.054	0.609	1.02E-04
280	553.15	750.8	33.15	1544000	4835	5280	0.0605	0.581	9.40E-05
300	573.15	713.8	46.15	1405000	5980	5750	0.0695	0.548	8.60E-05
320	593.15	667.1	64.57	1239000	7900	6540	0.0836	0.509	7.80E-05
340	613.15	610.5	92.62	1028000	11870	8240	0.11	0.469	7.00E-05

Table B.2: Properties of air. Data retrieved from: Çengel & Ghajar, *Heat and Mass Transfer*, Fourth Edition, Table A-15, page 884.

T [°C]	T [K]	ρ_{air} [kg/m^3]	λ_{air} [W/m.K]	$c_{p_{\mathrm{air}}}$ [J/kg.K]	μ_{air} [kg/m.s]
-150	123.15	2.866	0.01171	983	8.64E-06
-100	173.15	2.038	0.01582	966	0.00001189
-50	223.15	1.582	0.01979	999	0.00001474
-40	233.15	1.514	0.02057	1002	0.00001527
-30	243.15	1.451	0.02134	1004	0.00001579
-20	253.15	1.394	0.02211	1005	0.0000163
-10	263.15	1.341	0.02288	1006	0.0000168
0	273.15	1.292	0.02364	1006	0.00001729
5	278.15	1.269	0.02401	1006	0.00001754
10	283.15	1.246	0.02439	1006	0.00001778
15	288.15	1.225	0.02476	1007	0.00001802
20	293.15	1.204	0.02514	1007	0.00001825
25	298.15	1.184	0.02551	1007	0.00001849
30	303.15	1.164	0.02588	1007	0.00001872
35	308.15	1.145	0.02625	1007	0.00001895
40	313.15	1.127	0.02662	1007	0.00001918
45	318.15	1.109	0.02699	1007	0.00001941
50	323.15	1.092	0.02735	1007	0.00001963
60	333.15	1.059	0.02808	1007	0.00002008
70	343.15	1.028	0.02881	1007	0.00002052
80	353.15	0.9994	0.02953	1008	0.00002096
90	363.15	0.9718	0.03024	1008	0.00002139
100	373.15	0.9458	0.03095	1009	0.00002181
120	393.15	0.8977	0.03235	1011	0.00002264
140	413.15	0.8542	0.03374	1013	0.00002345
160	433.15	0.8148	0.03511	1016	0.0000242
180	453.15	0.7788	0.03646	1019	0.00002504
200	473.15	0.7459	0.03779	1023	0.00002577
250	523.15	0.6746	0.04104	1033	0.0000276
300	573.15	0.6158	0.04418	1044	0.00002934
350	623.15	0.5664	0.04721	1056	0.00003101
400	673.15	0.5243	0.05015	1069	0.00003261
450	723.15	0.488	0.05298	1081	0.00003415
500	773.15	0.4565	0.05572	1093	0.00003563
600	873.15	0.4042	0.06093	1115	0.00003846
700	973.15	0.3627	0.06581	1135	0.00004111
800	1073.15	0.3289	0.07037	1153	0.00004362
900	1173.15	0.3008	0.07465	1169	0.000046
1000	1273.15	0.2772	0.07868	1184	0.00004826
1500	1773.15	0.199	0.09599	1234	0.00005817
2000	2273.15	0.1553	0.11113	1264	0.0000663

Table B.3: Surface tension of liquid water. Data retrieved from: Çengel & Ghajar, *Heat and Mass Transfer*, Fourth Edition, Table 10-1, page 589.

T [°C]	**T [K]**	**γ [N/m]**
0	273.15	0.0757
20	293.15	0.0727
40	313.15	0.0696
60	333.15	0.0662
80	353.15	0.0627
100	373.15	0.0589
120	393.15	0.055
140	413.15	0.0509
160	433.15	0.0466

Table B.4: Properties of acetone. Data retrieved from: Faghri & Zhang (2006) and Faghri, Zhang & Howell (2010).

T [K]	**ρ_{liq} [kg/m^3]**	**ρ_{vap} [kg/m^3]**	**L [J/kg]**	**$c_{p_{vap}}$ [kJ/kg.K]**	**$c_{p_{liq}}$ [kJ/kg.K]**	**λ_{vap} [W/m.K]**	**λ_{liq} [W/m.K]**	**γ [N/m]**
233.15	860	0.03	660000	1.109	2.04	----	0.2	0.031
253.15	845	0.1	615600	1.16	2.07	0.0082	0.189	0.0276
273.15	812	0.26	564000	1.215	2.11	0.0096	0.183	0.0262
293.15	790	0.64	552000	1.271	2.16	0.011	0.181	0.0237
313.15	768	1.05	536000	1.328	2.22	0.0126	0.175	0.0212
333.15	744	2.37	517000	1.386	2.29	0.0143	0.168	0.0186
353.15	719	4.3	495000	1.444	2.39	0.0161	0.16	0.0162
373.15	689.6	6.94	472000	1.502	2.49	0.0178	0.148	0.0134
393.15	660.3	11.02	426100	1.56	2.61	0.0195	0.135	0.0107
413.15	631.8	18.61	394400	1.616	2.77	0.0215	0.126	0.0081

In the figures shown below, the data of the material properties (c_p, ρ, λ and h_{fg}) obtained from Tables B.1, B.2 and B.3 for water vapor and air are fitted into the different models that are presented in section 2.2.3. The equations and their respective coefficient of determination, R^2, are also shown in each figure. An additional set of models obtained from Table B.4 is shown in the present section and it was used in the numerical calculations to predict the evaporation of acetone droplets, however, these models are not shown in section 2.2.3.

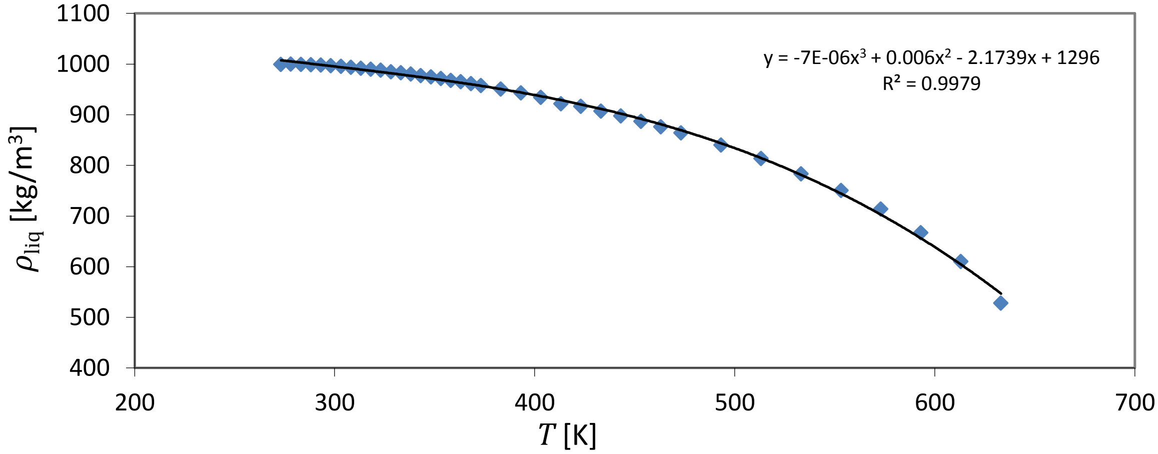

Figure B.1: Density of water (liquid phase) with respect to temperature

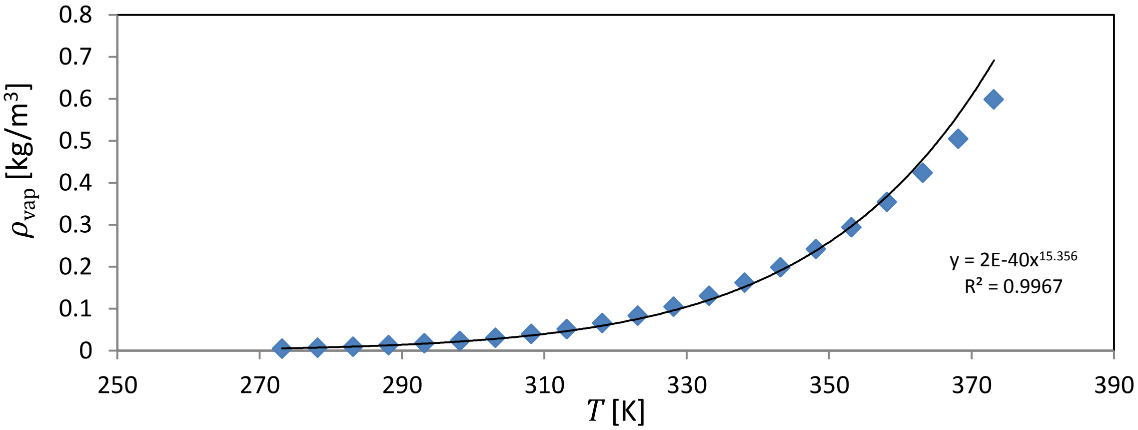

Figure B.2: Density of water (vapor phase) with respect to temperature

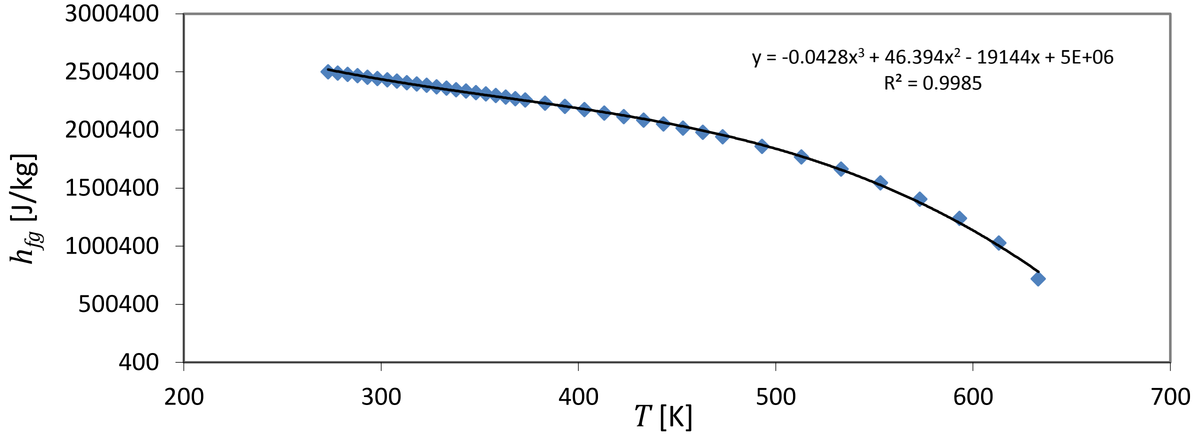

Figure B.3: Latent heat of vaporization of water vapor with respect to temperature

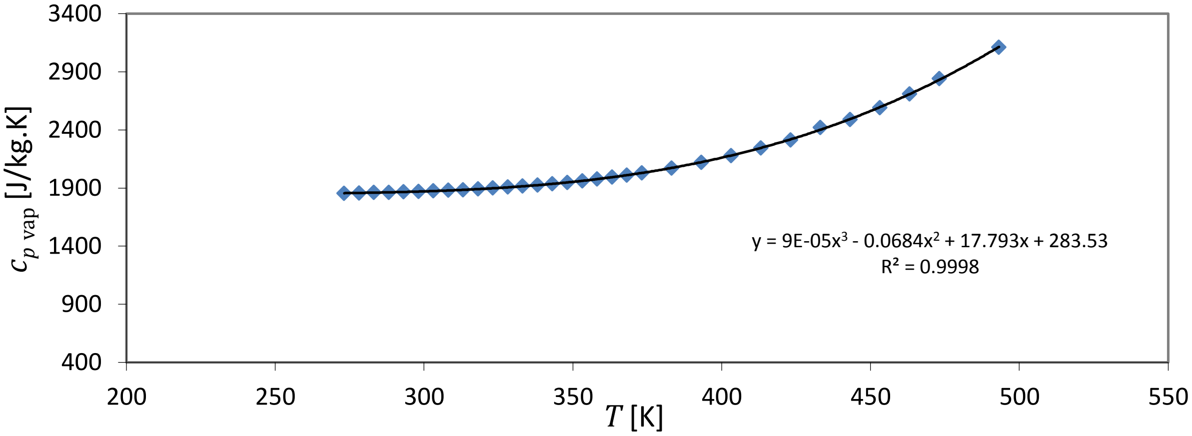

Figure B.4: Specific heat of water (vapor phase) with respect to temperature

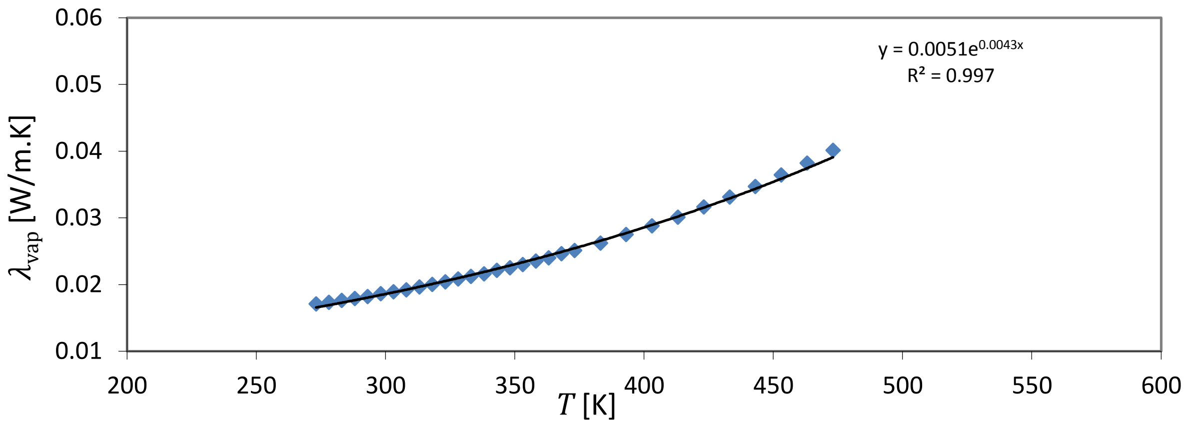

Figure B.5: Thermal conductivity of water (vapor phase) with respect to temperature

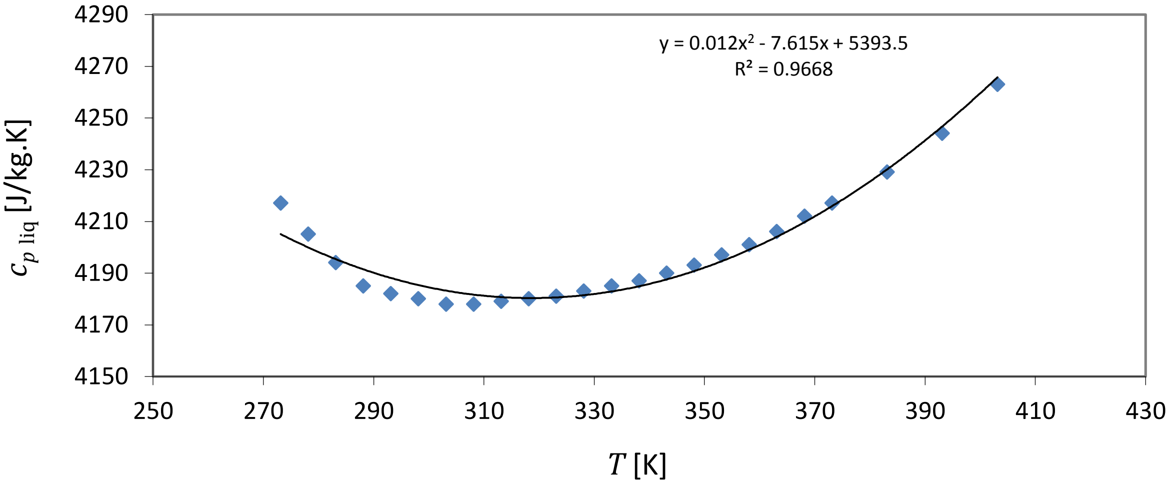

Figure B.6: Specific heat of water (liquid phase) with respect to temperature

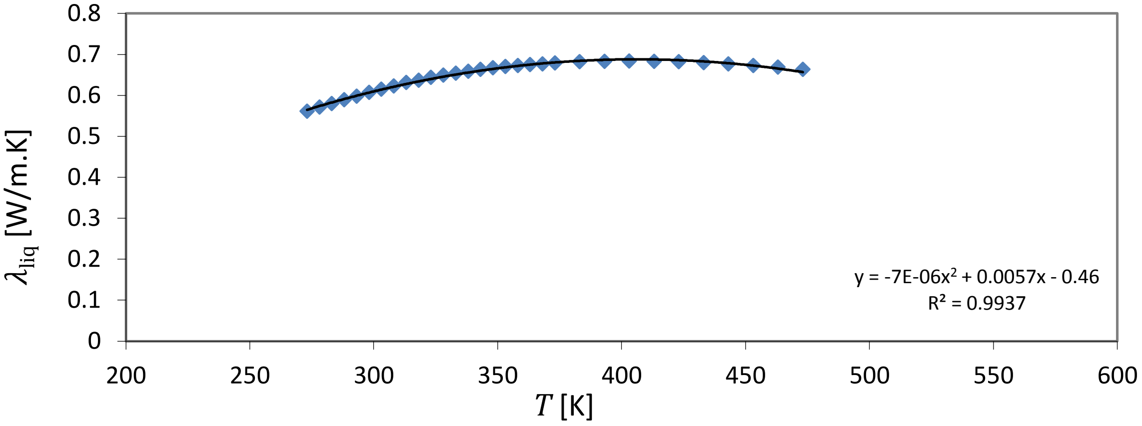

Figure B.7: Thermal conductivity of water (liquid phase) with respect to temperature

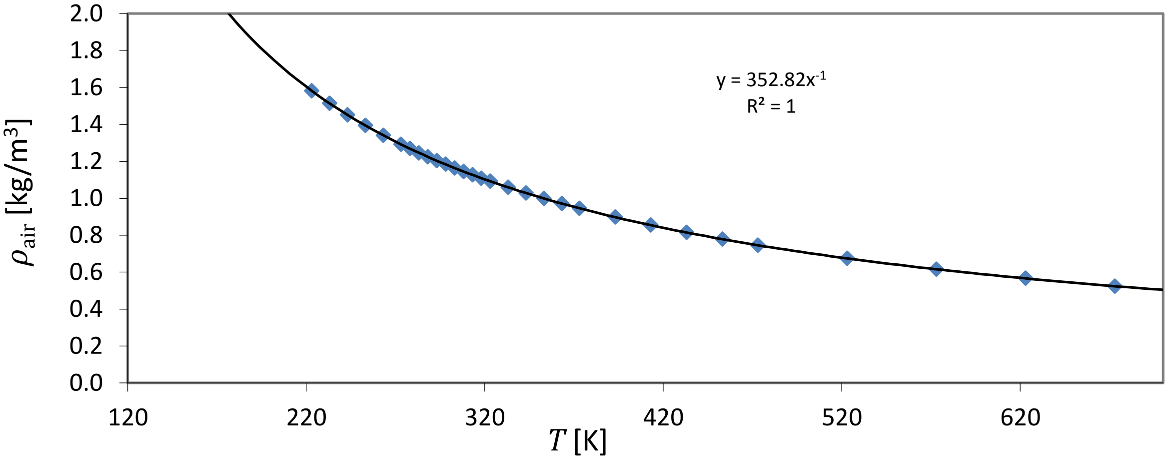

Figure B.8: Density of air with respect to temperature

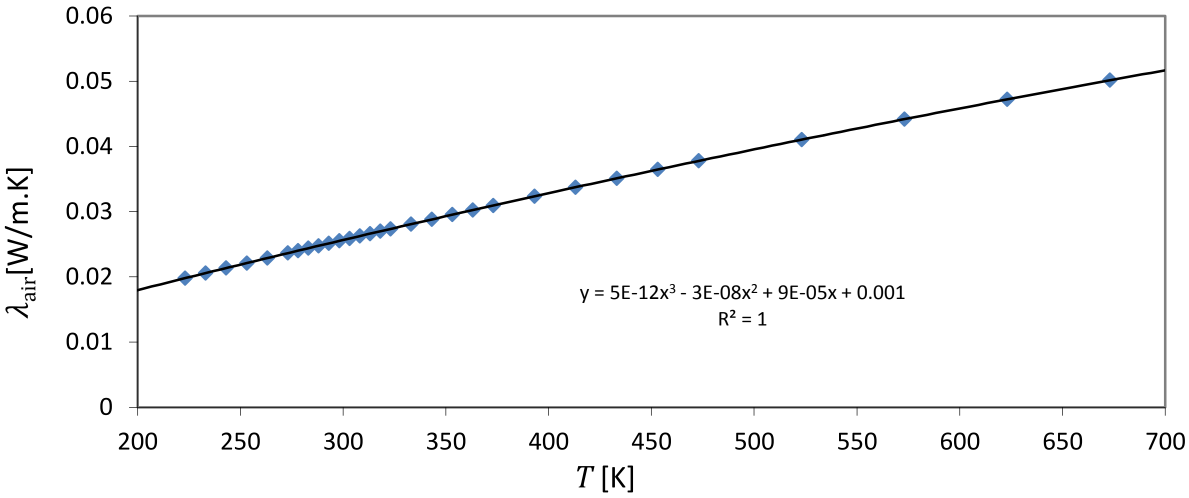

Figure B.9: Thermal conductivity of air with respect to temperature

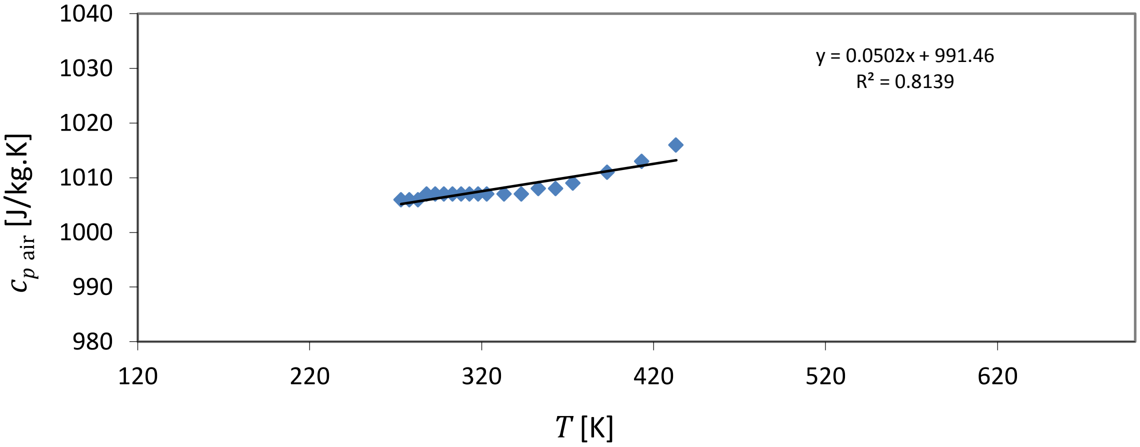

Figure B.10: Specific heat of air with respect to temperature

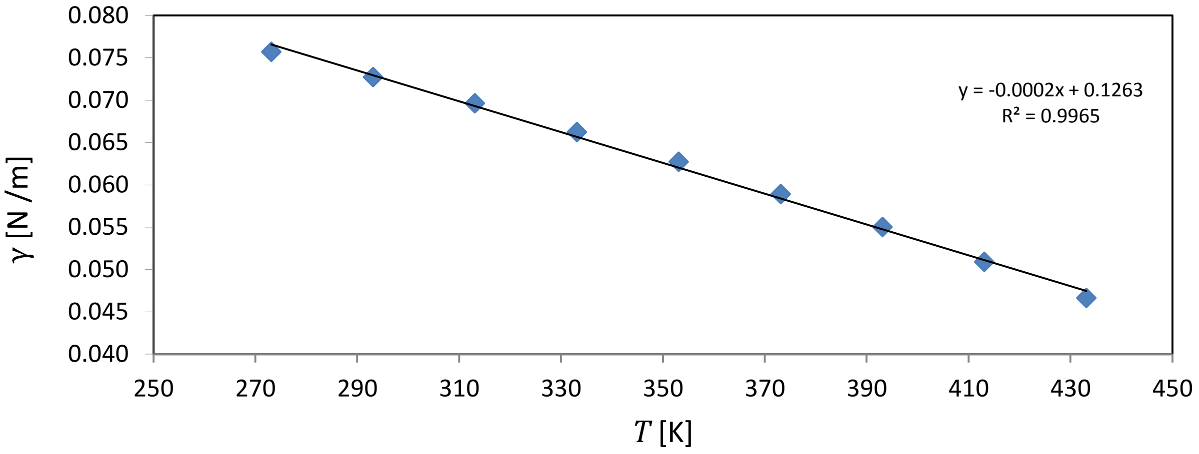

Figure B.11: Surface tension of water with respect to temperature

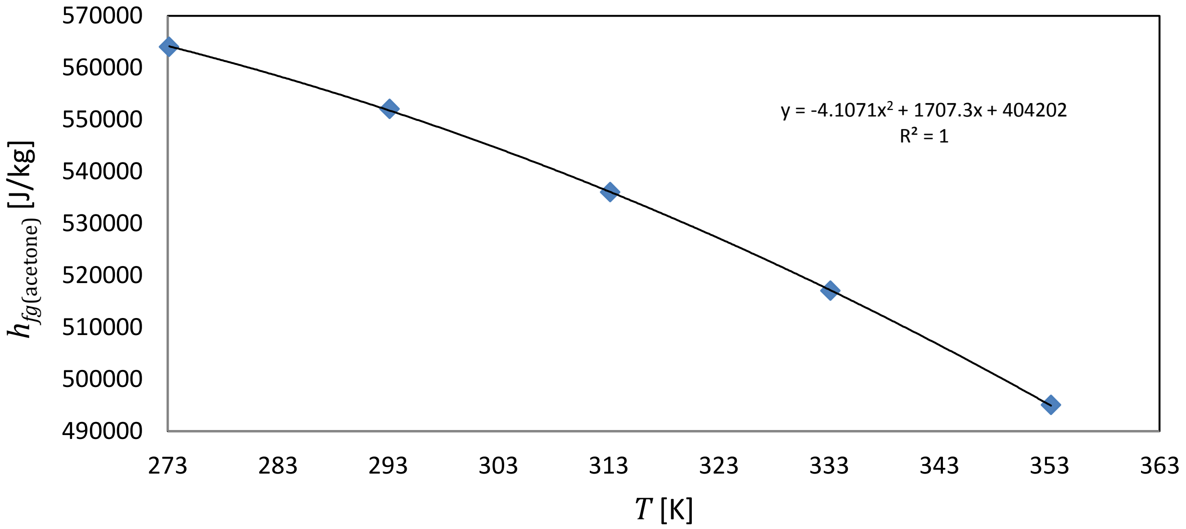

Figure B.12: Latent heat of vaporization of acetone with respect to temperature

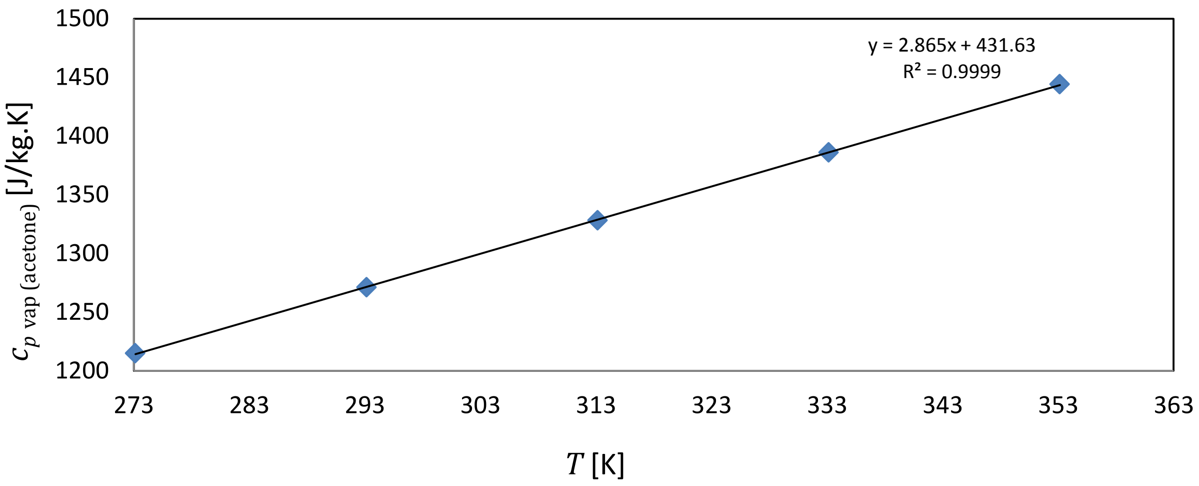

Figure B.13: Specific heat of acetone (vapor phase) with respect to temperature

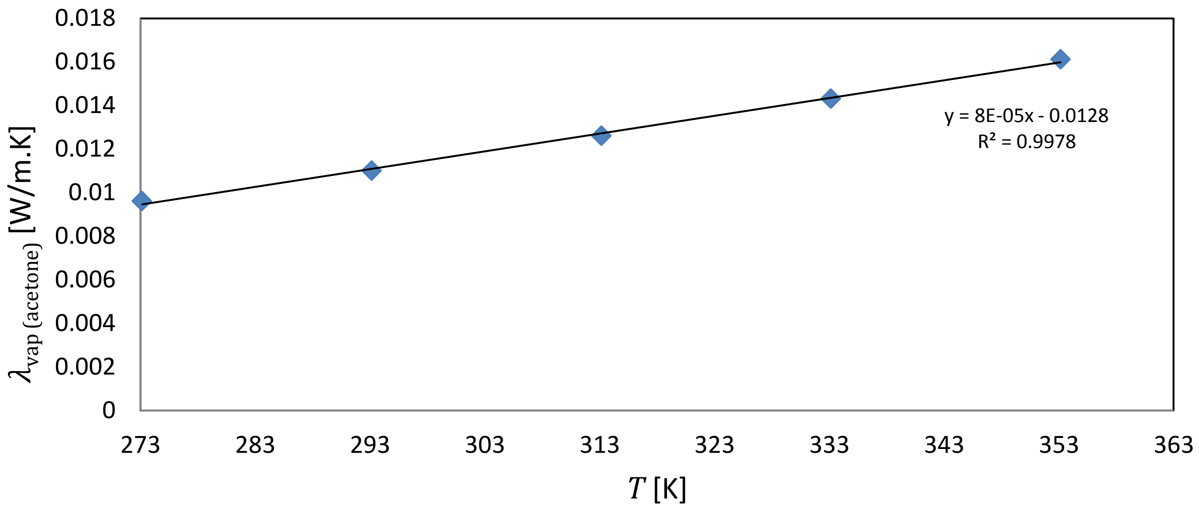

Figure B.14: Thermal conductivity of acetone (vapor phase) with respect to temperature

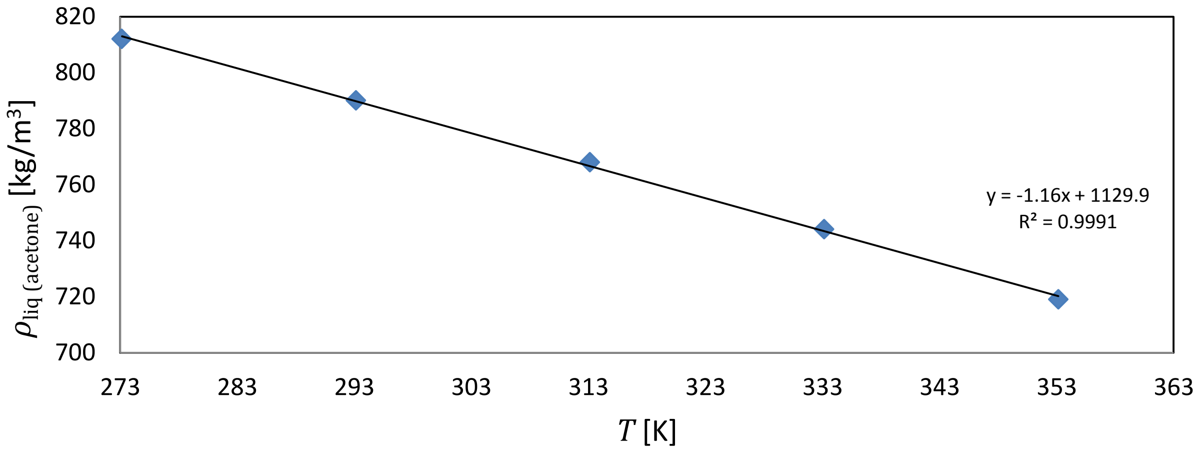

Figure B.15: Density of acetone (liquid phase) with respect to temperature

Appendix C

Commercial software codes

The computational codes shown in this appendix consist of two separate routines that calculates numerically the diameter with respect to time of water (section C.1) and acetone (section C.2) droplets for given conditions of initial size, air temperature, relative humidity, and radiation intensity. The two sub-routines shown in sections C.3 and C.4 are the definitions of the conservation of species ordinary differential equations for the water and acetone cases, respectively. The code was made using the commercial software Matlab®, version 8.0.0.783.

C.1 Droplet evaporation simulation code (pure water)

```
% Droplet evaporation with radiation V.2
% (c) 2014, Luis Ferraz
% function [ Result_Final] = energia(Tinf_INIT, Qdens, RH, rs,
r_inf, delta_t, est_time)
tic
%%% Set Initial parameters:
%%% Tinf_INIT = Temperature of environment at infinite position
or gas temperature [K]
%%% Qdens = Radiation energy density [W/m^2]
%%% RH = Fraction of Relative Humidity of Environment (0-1)
%%% rs = Initial radius of droplet [m]
%%% r_inf = distance of infinite conditions [m], recommendation:
use value
%%% of 0.1 (10 centimeters)
%%% delta_t= timestep [s];
%%% est_time = Estimated total time [s]
format long
```

```
global A B %Declare these variables as global to use them later
in the ODE solver function

%%% Set Initial parameters:
Tinf_INIT=”VALUE”; %% Temperature must be updated to this
current value in the odesystem_spec3(x,y) auxiliary function
Qdens=”VALUE”;
RH=”VALUE”;
rs=”VALUE”;
r_inf=”VALUE”;
delta_t=”VALUE”;
est_time=”VALUE”;

%%% Constants:
Wa=28.97; %Dry Air Molar mass [kg/mol]
Wv=18.015; %Water vapor Molar mass [kg/mol]
Ptot=101171.75; %Total atmospheric pressure [Pa]
Psat_inf=(10^(10.113-(1685.6/(Tinf_INIT-43.154)))); %Saturation
pressure far from the surface (Data from Vapor Pressure of pure
water tables found in the CRC Handbook of Chemistry and Physics,
2002. Antoine Equation)
Ru=8.3144621; %Universal gas constant
%Yinf=1/(1+((Wa/Wv)*((Ptot/(Psat_inf*RH))-1))); %Mass Fraction
of water vapor far from the surface
Yinf=0;
Result_Final=zeros((est_time/delta_t),3); %The Final result
matrix includes: [Column 1=timestep ; Column 2 = Temperature(K)
; Column 3 = Droplet Radius(m)]

for time=1:(est_time/delta_t)

As=4*pi*rs^2; %Surface area of the droplet
Af=pi*rs^2; %Surface area of the front face of the droplet
Qrad=Qdens*Af; %Total energy that hits the front face of droplet

Result_heat=zeros(10,4); %Create zeros vector to increase speed

%%% Mass flux due to the Energy Equation (Iteration process):
    for i=1:10;

        Result_heat(i,1)=280+(i*1);

        Psat_rs=(10^(10.113-(1685.6/(Result_heat(i,1)-
43.154)))); %Saturation pressure at the droplet surface
        Ys=1/(1+((Wa/Wv)*((Ptot/(Psat_rs))-1))); %Mass fraction
of water vapor at the droplet surface
```

```
        Tthird=Result_heat(i,1)+((1/3)*abs(Tinf_INIT-
Result_heat(i,1))); %% Applying the 1/3 rule to Temperature
        Ythird= Ys+((1/3)*(Yinf-Ys)); %% Applying the 1/3 rule
to Mass fraction

        %%% Note: All the correlations used to calculate the
properties:
        %%% Cp, lambda (thermal conductivity), Hfg and densities
of liquid water,
        %%% water vapor and dry air were obtainted by fitting
the data
        %%% found in the Tables A-9 and A-15 of "Heat and Mass
transfer",
        %%% Fourth Edition, Cengel & Ghajar, 2010.

        Cpv=(0.00009*(Tthird^3))-
0.0684*(Tthird^2)+17.793*Tthird+283.53; %Specific heat at
constant pressure (Cp) of vapor (evaluated at Tthird)
        Cpa=(0.0502*Tthird)+991.46; %Specific heat at constant
pressure (Cp) of air (evaluated at Tthird)
        Cp=(Cpv*Ythird)+(Cpa*(1-Ythird)); %Specific heat at
constant pressure (Cp) of air and vapor mixture (evaluated at
Ythird)
        Cpl=0.012*(Tthird^2)-7.615*Tthird+5393.5; %Specific heat
at constant pressure (Cp) of liquid water (evaluated at Tthird)

        lambdav=(0.0051*exp(0.0043*Tthird)); %Thermal
conductivity of vapor (evaluated at Tthird)
        lambdaa=((0.000000000005)*(Tthird^3)-
0.00000003*(Tthird^2)+(0.00009*Tthird)+0.001); %Thermal
conductivity of dry air (evaluated at Tthird)
        lambda=(lambdav*Ythird)+((1-Ythird)*lambdaa); %Thermal
conductivity of the vapor-air mixture (evaluated at Ythird)
        lambdal=-0.000007*(Tthird)^2+0.0057*(Tthird)-0.46;
%Thermal conductivity of liquid water (evaluated at Tthird)

        Hfg=(-0.0428*(Tthird^3))+46.394*(Tthird^2)-
19144*Tthird+5000000; %Latent heat of vaporization (evaluated at
Tthird)
        m=5.11661931467454e-12; %This is just a random number
(seed) to start the iteration and calculate the mass flux

        for j=1:1:10; % To increase precision add more zeros
(Computing time will increase)

            A=(m*Cp)/(4*pi*lambda); %Coefficient A: It will be
used later by the Species equation
```

```
           B=((Result_heat(i,1)-Tinf_INIT)*exp(A/rs))/(1-
exp(A/rs)); %Coefficient B: It will be used later by the Species
equation
           dTdr=A*B*exp(-A/rs)/(rs^2); % This is the analytic
solution of the Energy equation as seen in...

           m=(Qrad+(lambda*As*dTdr))/Hfg;

        end
           Result_heat(i,2)=m;
           Result_heat(i,3)=A;
           Result_heat(i,4)=B;

    end

Result_spec=zeros(10,2);
Rs=rs*1000000; % To convert metres to microns
R_inf=r_inf*1000000; % To convert metres to microns

%%% Mass flux due to the Species Equation (Iteration process):
    for k=1:10;
        Result_spec(k,1)=280+(k*1);


        Psat_rs=(10^(10.113-(1685.6/(Result_spec(k,1)-
43.154)))); %Saturation pressure at the droplet surface
        Ys=1/(1+((Wa/Wv)*((Ptot/(Psat_rs))-1))); %Mass fraction
of water vapor at the droplet surface

        Ythird= Ys+((1/3)*(Yinf-Ys)); %% Applying the 1/3 rule
to Mass fraction
        Tthird=Result_spec(k,1)+((1/3)*abs(Tinf_INIT-
Result_spec(k,1))); %% Applying the 1/3 rule to Temperature

        D=(0.000000000187)*((Tthird)^(2.072)); %Diffusivity
        Ys_air=1-Ys; %Mass fraction of dry air at the droplet
surface
        Wmix=((Ys*Wv)+(Ys_air*Wa))/1000; %Molar mass of the
Vapor-Air mixture
        dens_mix=(Ptot*Wmix)/(Ru*Tthird); %Density of the Vapor-
Air mixture

        dens_liq=(-0.000007)*(Tthird^3)+0.006*(Tthird^2)-
(2.1739*Tthird)+1296;

        A=Result_heat(k,3)*1000000;
        B=Result_heat(k,4);
```

```
        %for l=-0.00001:0.00000001:0.00001 %To increase
precision, just add more zeros to the steps (Computing time will
increase).
        for l=0:-0.000001:-0.5 %To increase precision, just add
more zeros to the steps (Computing time will increase).

            [X,Y] = ode45(@odesystem_spec3,[Rs R_inf],[Ys l]);
%Runge-Kutta method to solve the ODE (See also ODE23)

            Yinf_prueba=Y(end,1); %This command selects the last
value of the Mass fraction at the infinity condition in order to
perform a shooting method comparison to solve the ODE


            COND=((Yinf_prueba)-(Yinf)) %This compares the value
that we want to get (shooting target) with the result given by
the ODE45 algorythm

            if COND<=0.00000001 %Tolerance, to increase
precision add more zeros (computing time will increase).
            break

            end

        end
            dYdr=l;
            DYdr=dYdr*1000000;
            Result_spec(k,2)=-dens_mix*4*pi*(rs)^2*(D)*DYdr;
    end

    H=Result_heat;
    S=Result_spec;
    %figure
    %plot(Result_heat(:,1),Result_heat(:,2),'-
',Result_spec(:,1),Result_spec(:,2),'-.')

%%% Graphical determination of Unique Temperature and Mass flux
intersection
p=polyfit(S(:,1),S(:,2),3); % p is the vector of coefficients of
a 3rd order polynomial that fits to the data of the species
equation solution
q=polyfit(H(:,1),H(:,2),2); % q is the vector of coefficients of
a 2nd order polynomial that fits to the data of the heat
equation solution
```

```
r=[p(1,1) (p(1,2)-q(1,1)) (p(1,3)-q(1,2)) (p(1,4)-q(1,3))];
%After equating the polynomials p and q, one of the roots of the
polynomial r will give the solution of the Temperature
raices=roots(r);
temperature_solution=raices(1,1)+(1/3)*abs(Tinf_INIT-
raices(1,1));
massflux_solution=polyval(q,raices(1,1)); %Evaluate the
temperature solution into one of the fitted polynomials to get
the solution value of the mass flux


%%% Timestep application and determination of the new droplet
radius
Density=((-
0.000007)*(temperature_solution^3))+(0.006*(temperature_solution
^2))-(2.1739*temperature_solution) + 1296; %Density of the
liquid droplet at the solution temperature [kg/m^3]
Volume=(4/3)*pi*((rs)^3); %Volume of the droplet [m^3]
Mass=Density*Volume; %Total mass of the droplet [kg]
New_Mass=Mass-(massflux_solution*delta_t); %The new mass of the
droplet after applying the mass flux for a time equal to delta_t
(timestep) [kg]
New_Volume=New_Mass/Density; %The new volume of the droplet
after applying the mass flux for a time equal to delta_t
(timestep) [m^3]
rs=((3*New_Volume)/(4*pi))^(1/3); %The new radius of the droplet
after applying the mass flux for a time equal to delta_t
(timestep) [m]

if rs<=0
    break
end

Result_Final(time,1)=time*delta_t;
Result_Final(time,2)=temperature_solution;
Result_Final(time,3)=rs;
end
Result_Final;
figure
plot(Result_Final(:,1),Result_Final(:,3))
toc
% end
```

C.2 Droplet evaporation simulation code (acetone)

```
% Acetone Droplet evaporation with radiation V.2
% (c) 2014, Luis Ferraz
% function [ Result_Final] = energia(Tinf_INIT, Qdens, RH, rs,
r_inf, delta_t, est_time)
tic
%%% Set Initial parameters:
%%% Tinf_INIT = Temperature of environment at infinite position
[K]
%%% Qdens = Radiation energy density [W/m^2]
%%% RH = Fraction of Relative Humidity of Environment (0-1), In
the case of Acetone this value is Zero
%%% rs = Initial radius of droplet [m]
%%% r_inf = distance of infinite conditions [m], recommendation:
use value
%%% of 0.1 (10 centimeters)
%%% delta_t= timestep [s];
%%% est_time = Estimated total time [s]
format long
global A B %Declare these variables as global to use them later
in the ODE solver function

%%% Set Initial parameters:
Tinf_INIT=”VALUE”;
Qdens=”VALUE”;
RH=0; %The concept of RH does not apply to substances rather
than water
rs=”VALUE”;
r_inf=”VALUE”;
delta_t=”VALUE”;
est_time=”VALUE”;

%%% Constants:
Wa=28.97; %Dry Air Molar mass [kg/mol]
Wace=58.08; %Water vapor Molar mass [kg/mol]
Ptot=101171.75; %Total atmospheric pressure [Pa]
Psat_inf=133.3224*(10^(7.1327-(1219.97/((Tinf_INIT-
273.15)+230.653)))); %Acetone Saturation pressure far from the
surface (Fitted Antoine Equation, Data from:)[Pa]
Ru=8.3144621; %Universal gas constant
%Yinf=1/(1+((Wa/Wace)*((Ptot/(Psat_inf*RH))-1))); %Mass Fraction
of water vapor far from the surface
Yinf=0;
```

```
Result_Final=zeros((est_time/delta_t),3); %The Final result
matrix includes: [Column 1=timestep ; Column 2 = Temperature(K)
; Column 3 = Droplet Radius(m)]

for time=1:(est_time/delta_t)

As=4*pi*rs^2; %Surface area of the droplet
Af=pi*rs^2; %Surface area of the front face of the droplet
Qrad=Qdens*Af; %Total energy that hits the front face of droplet

Result_heat=zeros(10,4); %Create zeros vector to increase speed

%%% Mass flux due to the Energy Equation (Iteration process):
    for i=1:10;

        Result_heat(i,1)=240.15+(i*1);

        Psat_rs=133.3224*(10^(7.1327-
(1219.97/((Result_spec(k,1)-273.15)+230.653)))); %Saturation
pressure at the droplet surface
        Ys=1/(1+((Wa/Wace)*((Ptot/(Psat_rs))-1))); %Mass
fraction of acetone vapor at the droplet surface

        Tthird=Result_heat(i,1)+((1/3)*abs(Tinf_INIT-
Result_heat(i,1))); %% Applying the 1/3 rule to Temperature
        Ythird= Ys+((1/3)*(Yinf-Ys)); %% Applying the 1/3 rule
to Mass fraction

        Cpv=(2.865*(Tthird))+431.63; %Specific heat at constant
pressure (Cp) of vapor (evaluated at Tthird)
        Cpa=(0.0502*Tthird)+991.46; %Specific heat at constant
pressure (Cp) of air (evaluated at Tthird)
        Cp=(Cpv*Ythird)+(Cpa*(1-Ythird)); %Specific heat at
constant pressure (Cp) of air and vapor mixture (evaluated at
Ythird)

        lambdav=(0.00008*Tthird)-0.0128; %Thermal conductivity
        lambdaa=((0.000000000005)*(Tthird^3)-
0.00000003*(Tthird^2)+(0.00009*Tthird)+0.001); %Thermal
conductivity of dry air (evaluated at Tthird)
        lambda=(lambdav*Ythird)+((1-Ythird)*lambdaa); %Thermal
conductivity of the vapor-air mixture (evaluated at Ythird)

        Hfg=(-4.1071*(Tthird^2))+(1707.3*(Tthird))+404202;
%Latent heat of vaporization
```

```
        m=5.11661931467454e-12; %This is just a random number
(seed) to start the iteration and calculate the mass flux

        for j=1:1:10; % To increase precision add more zeros
(Computing time will increase)

           A=(m*Cp)/(4*pi*lambda); %Coefficient A: It will be
used later by the Species equation
           B=((Result_heat(i,1)-Tinf_INIT)*exp(A/rs))/(1-
exp(A/rs)); %Coefficient B: It will be used later by the Species
equation
           dTdr=A*B*exp(-A/rs)/(rs^2); % This is the analytic
solution of the Energy equation as seen in...

           m=(Qrad+(lambda*As*dTdr))/Hfg;

        end
           Result_heat(i,2)=m;
           Result_heat(i,3)=A;
           Result_heat(i,4)=B;

    end

Result_spec=zeros(10,2);
Rs=rs*1000000; % To convert metres to microns
R_inf=r_inf*1000000; % To convert metres to microns

%%% Mass flux due to the Species Equation (Iteration process):
    for k=1:10;
        Result_spec(k,1)=240.15+(k*1);

        Psat_rs=133.3224*(10^(7.1327-
(1219.97/((Result_spec(k,1)-273.15)+230.653)))); %Saturation
pressure at the droplet surface
        Ys=1/(1+((Wa/Wace)*((Ptot/(Psat_rs))-1))); %Mass
fraction of acetone vapor at the droplet surface

        Ythird= Ys+((1/3)*(Yinf-Ys)); %% Applying the 1/3 rule
to Mass fraction
        Tthird=Result_spec(k,1)+((1/3)*abs(Tinf_INIT-
Result_spec(k,1))); %% Applying the 1/3 rule to Temperature

        D=1.17e-05; %Diffusivity (could not find data, therefore
a constant value was used)
        Ys_air=1-Ys; %Mass fraction of dry air at the droplet
surface
```

```
        Wmix=((Ys*Wace)+(Ys_air*Wa))/1000; %Molar mass of the
Vapor-Air mixture
        dens_mix=(Ptot*Wmix)/(Ru*Tthird); %Density of the Vapor-
Air mixture


        A=Result_heat(k,3)*1000000;
        B=Result_heat(k,4);

        %for l=-0.00001:0.00000001:0.00001 %To increase
precision, just add more zeros to the steps (Computing time will
increase).
        for l=0:-0.000001:-0.5 %To increase precision, just add
more zeros to the steps (Computing time will increase).

            [X,Y] = ode45(@odesystem_spec3_acetone,[Rs
R_inf],[Ys l]); %Runge-Kutta method to solve the ODE (See also
ODE23)

            Yinf_prueba=Y(end,1); %This command selects the last
value of the Mass fraction at the infinity condition in order to
perform a shooting method comparison to solve the ODE


            COND=((Yinf_prueba)-(Yinf)) %This compares the value
that we want to get (shooting target) with the result given by
the ODE45 algorythm

            if COND<=0.00000001 %Tolerance, to increase
precision add more zeros (computing time will increase).
            break

            end

        end
            dYdr=l
            DYdr=dYdr*1000000;
            Result_spec(k,2)=-dens_mix*4*pi*(rs)^2*(D)*DYdr
    end

    H=Result_heat;
    S=Result_spec;
    %figure
    %plot(Result_heat(:,1),Result_heat(:,2),'-
',Result_spec(:,1),Result_spec(:,2),'-.')
```

```
%%% Graphical determination of Unique Temperature and Mass flux
intersection
p=polyfit(S(:,1),S(:,2),3); % p is the vector of coefficients of
a 3rd order polynomial that fits to the data of the species
equation solution
q=polyfit(H(:,1),H(:,2),2); % q is the vector of coefficients of
a 2nd order polynomial that fits to the data of the heat
equation solution
r=[p(1,1) (p(1,2)-q(1,1)) (p(1,3)-q(1,2)) (p(1,4)-q(1,3))];
%After equating the polynomials p and q, one of the roots of the
polynomial r will give the solution of the Temperature
raices=roots(r);
temperature_solution=raices(1,1)+(1/3)*abs(Tinf_INIT-
raices(1,1));
massflux_solution=polyval(q,raices(1,1)); %Evaluate the
temperature solution into one of the fitted polynomials to get
the solution value of the mass flux

%%% Timestep application and determination of the new droplet
radius
Density=((-1.16)*(temperature_solution))+ 1129.9; %Density of
the liquid droplet at the solution temperature [kg/m^3]
Volume=(4/3)*pi*((rs)^3); %Volume of the droplet [m^3]
Mass=Density*Volume; %Total mass of the droplet [kg]
New_Mass=Mass-(massflux_solution*delta_t); %The new mass of the
droplet after applying the mass flux for a time equal to delta_t
(timestep) [kg]
New_Volume=New_Mass/Density; %The new volume of the droplet
after applying the mass flux for a time equal to delta_t
(timestep) [m^3]
rs=((3*New_Volume)/(4*pi))^(1/3); %The new radius of the droplet
after applying the mass flux for a time equal to delta_t
(timestep) [m]

if rs<=0
    break
end

Result_Final(time,1)=time*delta_t;
Result_Final(time,2)=temperature_solution;
Result_Final(time,3)=rs;
end
Result_Final;
figure
plot(Result_Final(:,1),Result_Final(:,3))
toc
% end
```

C.3 Species conservation ODE function (pure water)

```
function dy = odesystem_spec3(x,y)    %The Species Equation
decoupled

global A B

Wa=28.97;
Wv=18.015;

dy = zeros(2,1);    % Preallocate zeros for speed

dy(1) = y(2);
dy(2) = (((A*B*exp(-A/x)/(x^2))/( ”T_INF_VALUE”+B*exp(-A/x)-B))-
((((Wv-Wa)*y(2)*x^2)+(2*(Wv-Wa)*x*y(1))+(2*Wa*x))/(((Wv-
Wa)*y(1)*x^2)+Wa*x^2)))*y(2);


end
```

C.4 Species conservation ODE function (acetone)

```
function dy = odesystem_spec3_acetone(x,y)    %The Species
Equation decoupled

global A B

Wa=28.97;
Wv=58.08;

dy = zeros(2,1);    % Preallocate zeros for speed

dy(1) = y(2);
dy(2) = (((A*B*exp(-A/x)/(x^2))/( ”T_INF_VALUE”+B*exp(-A/x)-B))-
((((Wv-Wa)*y(2)*x^2)+(2*(Wv-Wa)*x*y(1))+(2*Wa*x))/(((Wv-
Wa)*y(1)*x^2)+Wa*x^2)))*y(2);


end
```

Appendix D

Sensitivity of the measuring instruments and droplet generator

Experiments were conducted to investigate the sensitivity of the instruments used to measure the temperature and relative humidity of the air. Two different tests were performed in low and high relative humidity conditions (*i.e.,* 0% and 90%, respectively). The tests consisted in measuring the values of relative humidity and temperature of the flowing air inside the glass tube every 15 seconds. The total number of data points recorded for each case was approximately 575, which results in a total time of approximately 2.4 hours. Air at standard laboratory conditions was selected as the starting condition in order to determine the minimum time for the stabilization of the measured values. Figures D.1, D.2, D.4 and D.5 show the variation of relative humidity and temperature with respect to time for low and high RH air environments, respectively.

A third experiment was conducted to study the sensitivity of the droplet generator. The experiment was performed in parallel to the relative humidity and temperature sensitivity measurements. The camera was located in a position near the nozzle exit in order to record the first droplet that exits the generator. The droplets were produced at a frequency of 1 Hz and recorded every 12 seconds. A total of 700 images were obtained, which results in an approximate time of 2.3 hours. The droplet diameter was calculated using the same calibration parameters and following the same procedure as shown in the general results. Figures D.3 and D.6 show the variation of the initial droplet diameter with respect to time for low and high relative humidity conditions, *i.e.*, 0% and 90%, respectively.

From the figures it can be observed that a minimum waiting time of 0.5 hours must be accounted for after setting the relative humidity in every experiment in order to reach the stabilization of the system. Furthermore, it can be observed that after reaching the desired value, the variation of RH with respect to time can be considered negligible. Given the characteristics of the experimental setup and the instruments used, a relative humidity of 0% could not be reached in any of the experiments performed and reported in Chapter 5; therefore, an approximate value of 1% was used in all the experiment and model calculations

D.1 Low relative humidity results

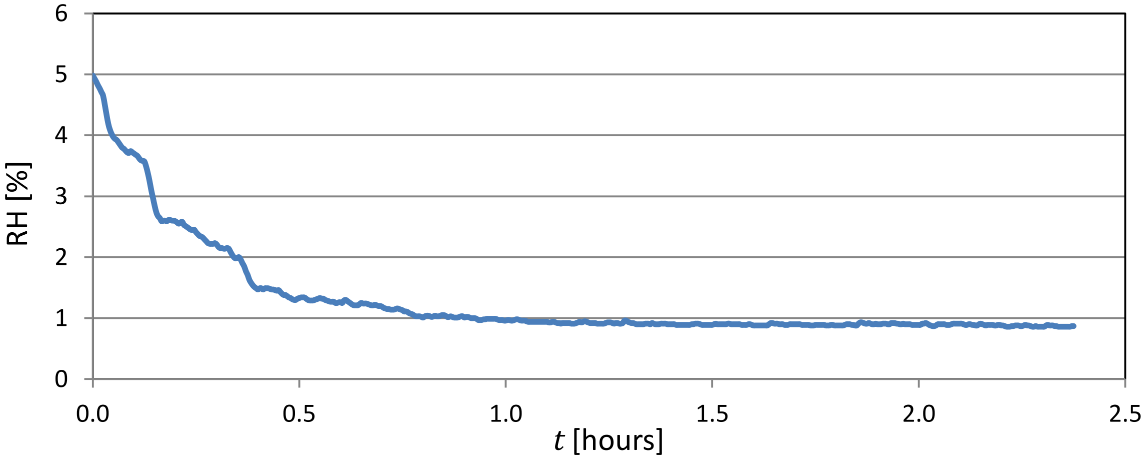

Figure D.1: Stability of the measured relative humidity with respect to time in a low RH environment

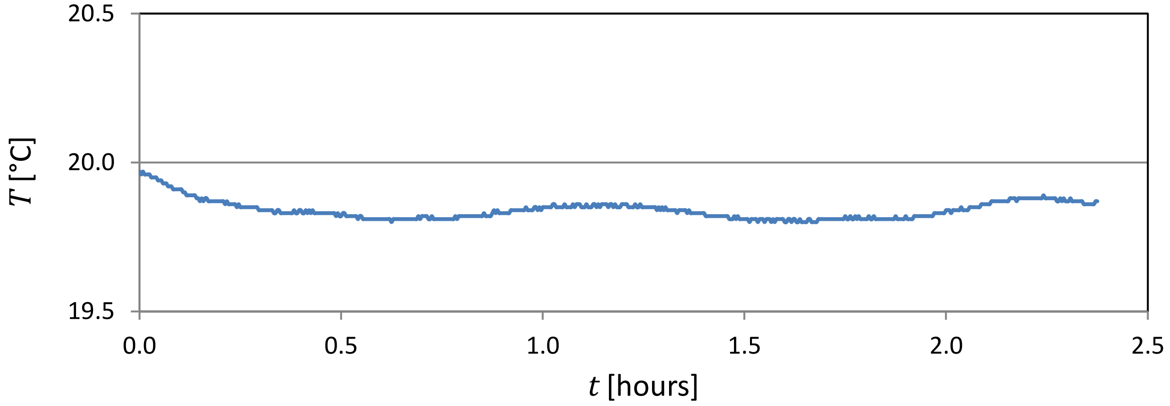

Figure D.2: Stability of the measured temperature with respect to time in a low RH environment

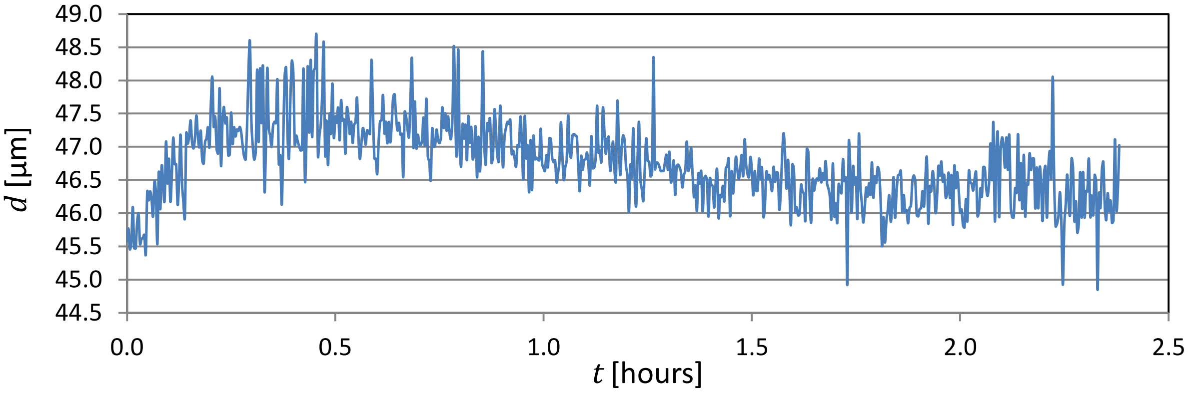

Figure D.3: Variation of the initial droplet diameter with respect to time in a low RH environment

D.2 High relative humidity results

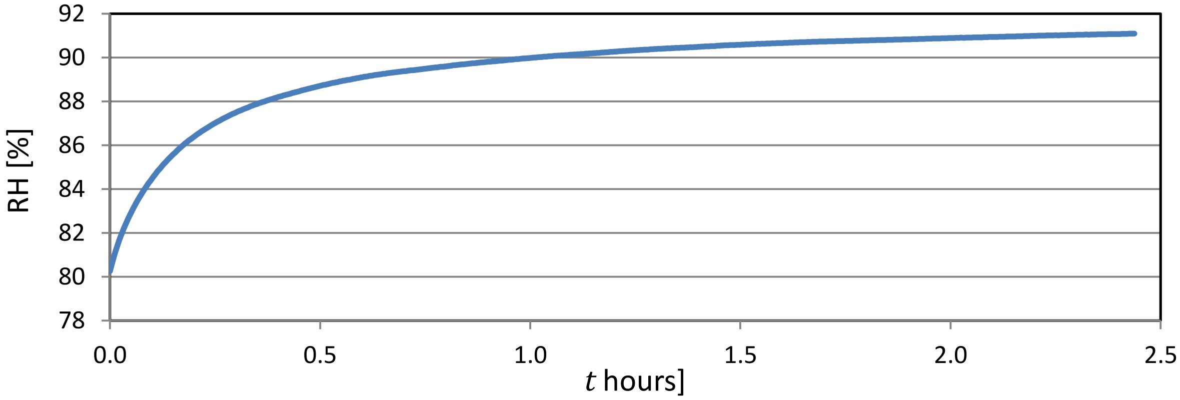

Figure D.4: Stability of the measured relative humidity with respect to time in a high RH environment

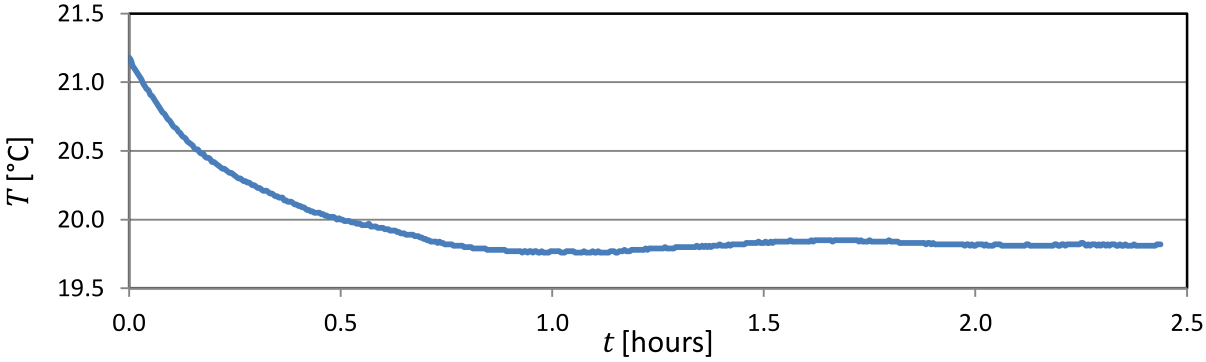

Figure D.5: Stability of the measured temperature with respect to time in a high RH environment

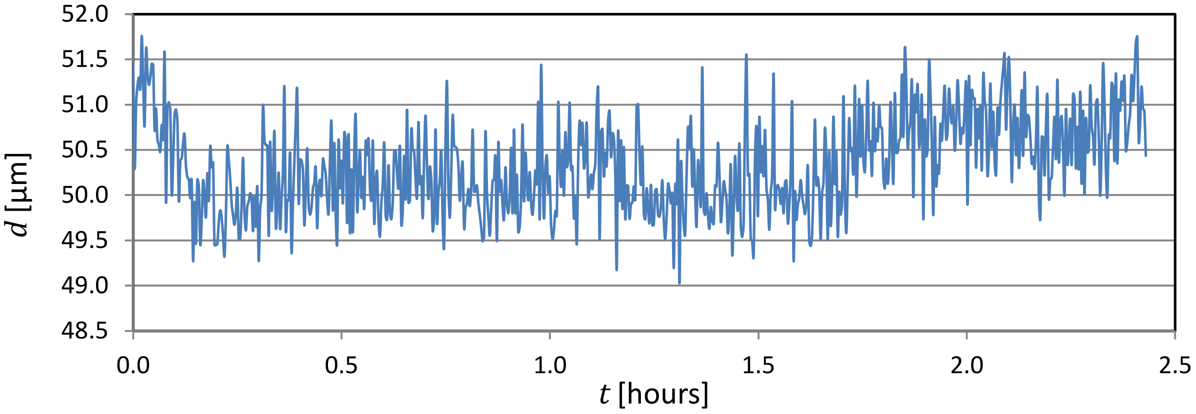

Figure D.6: Variation of the initial droplet diameter with respect to time in a high RH environment

Appendix E

Determination of the laser beam intensity distribution

A detailed explanation of the experiment used to determine the beam diameter or “width” is given in this section. The laser beam was emitted at full power (with a measured value of 2.525 Watts at a wavelength of 2.8 µm) and aligned horizontally with respect to a random observer in the laboratory using gold-coated mirrors. The measuring setup consisted of a laser energy meter (Model FieldMaxII-P, Coherent Inc.) placed perpendicularly to the horizontal beam, allowing all the energy to be absorbed by the meter’s measuring window. A 150 µm-diameter precision pinhole (Model P150S, Thorlabs Inc.) was placed between the laser beam and the power meter perpendicularly to the beam’s axis and attached to a motorized traverse (Model BiSlide, Velmex Inc.) which allowed the movement of the pinhole in the horizontal and vertical directions with respect to the laser beam axis. The objective of the setup was to let a small amount of energy from the incoming beam to pass through the pinhole and be measured by the power meter at different positions in the horizontal and vertical directions, thus, creating a 3-dimensional profile of the power distribution.

The vertical scanning was achieved by moving the motorized traverse a total distance of 900 steps (0.00025 inches per step) with increments of 50 steps. The horizontal scanning was achieved by moving a manual stage connected to a linear displacement dial indicator a total distance of 150 marks (0.001 inches per mark) with increments of 5 and 10 marks. The uncertainty of the measured distance in the vertical direction can be neglected due to the accuracy of the stepping motor; however, due to the nature of the dial indicator and human errors, the horizontal distance readings are estimated to have an uncertainty of ± 0.001 inches (1 mark).

The values of the laser power measured by the energy meter were converted from a range of 0-30 mW to an output signal (0-2 Volts range) and sent to a computer for processing. A minimum of 1000 voltage readings per position were recorded and averaged. After applying several digital filters to the data to remove the noise introduced by external factors, the data (in volts) was converted to energy density (in mW/mm^2) by converting the signal back from volts to mW and divide by the surface area of the pinhole orifice.

The resulting data was then plotted and is shown in Figures E.1(a) and E.1(b). It can be observed that the profile of the beam has a Gaussian distribution, which was expected based on the information given by the manufacturer (TEM$_{00}$ mode). A top view of the profile, as seen in Figure E.1(b) reveals that the profile is not perfectly circular but has an elliptical shape. The reason of this is still not clear, but it is believed that it is due to a combination of imperfections in the optics (gold coated mirrors) and errors in the measuring technique.

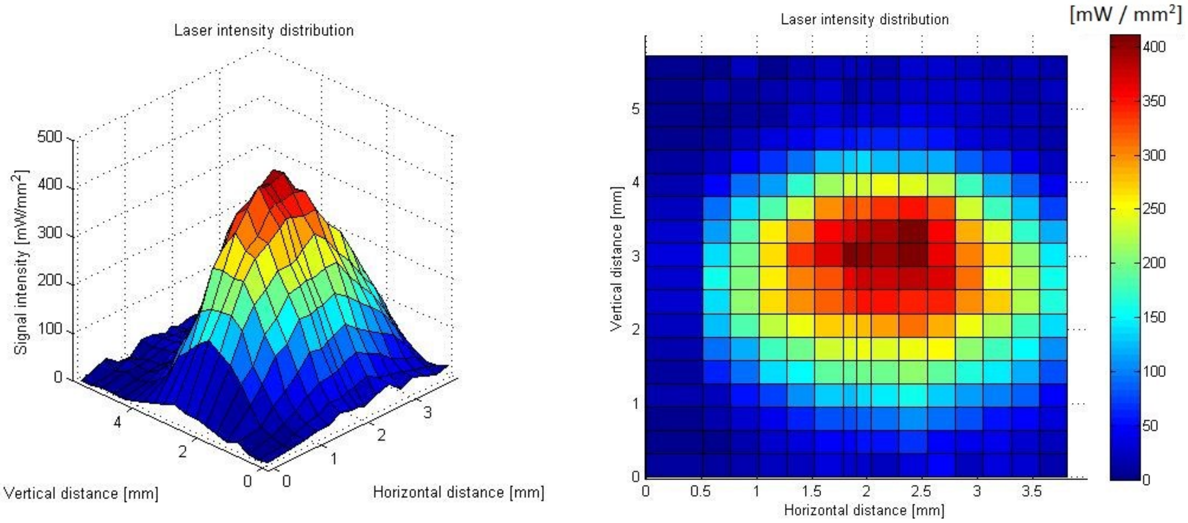

(a) (b)

Figure E.1: Laser beam 3-dimensional profile

A surface integration was done using commercial software (Matlab version 8.0.0.783, The MathWorks Inc.) to calculate the volume under the Gaussian surface. This corresponds to the total integrated power of the beam and the value obtained was 2.688 Watts. The result appears to be sufficiently close to the measured value of 2.525 Watts with a difference of 6%.

Additional 2-D views of Figure E.1 are shown in Figure E.2(a) and (b). It can be observed in Figure E.2(a) that there is no defined maximum or “peak”. This is not true in the case of Figure E.2(b), in which a noticeable and obvious peak can be observed.

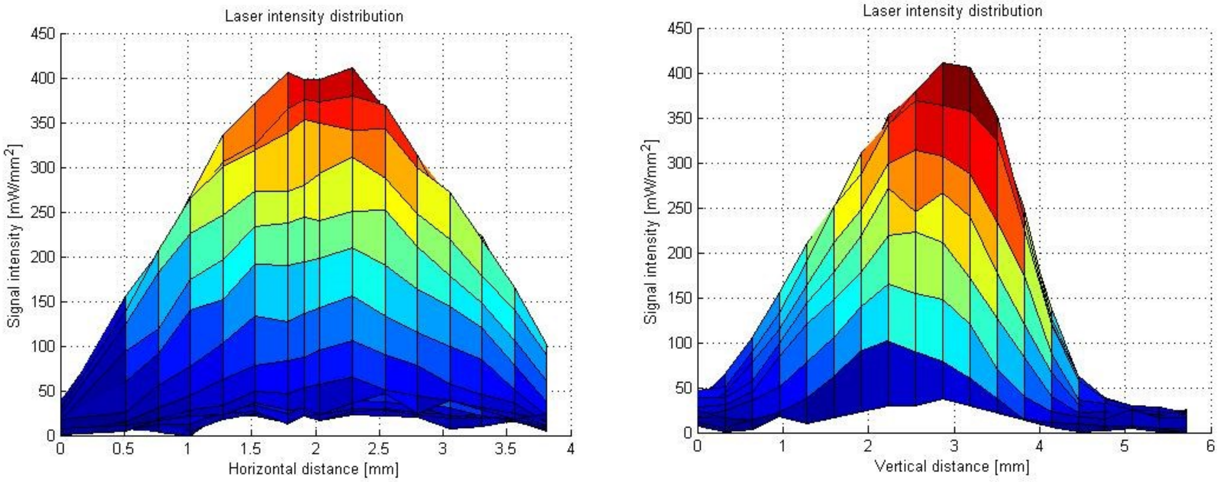

(a) (b)

Figure E.2: Laser intensity distribution in the horizontal (a) and vertical (b) directions

To determine the beam diameter, 4 different profiles in the horizontal direction (x) and 3 in the vertical direction (y) were plotted and averaged. Figures E.3(a) and E.3(b) show the beam intensity distribution versus the horizontal distance and the vertical distance (in millimeters), respectively, for different fixed positions in the x and y directions. The profiles were selected due to their proximity with the apparent maximums of the Gaussian surface rather than averaging all the available profiles (which would lead to a significant underestimation of the diameter); therefore the average curves will have a "smooth" shape and be more suitable for the diameter calculations.

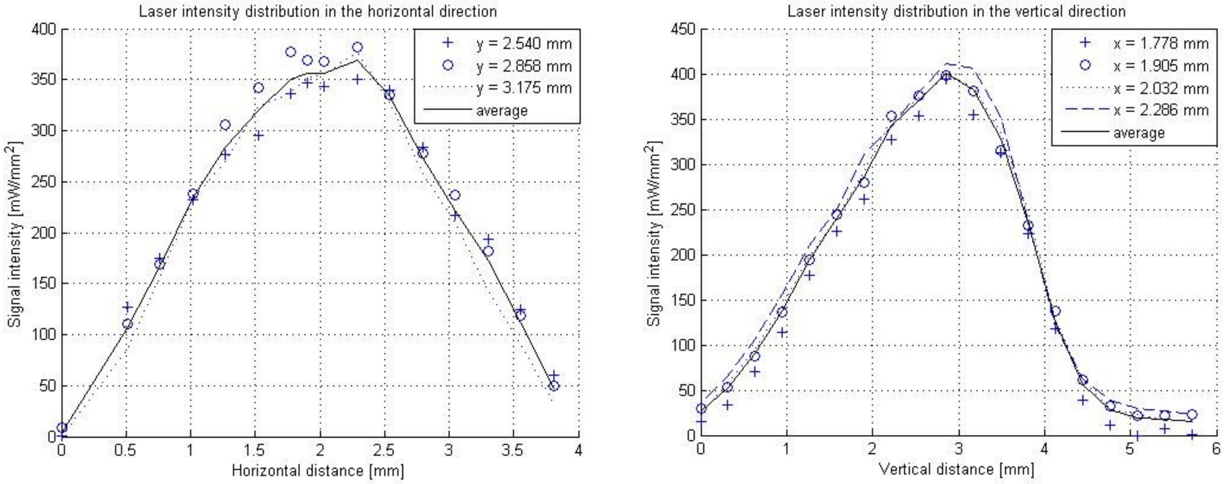

(a) (b)

Figure E.3: Laser intensity distribution in the horizontal (a) and vertical (b) directions for different fixed positions and average values

Several definitions of the diameter or "width" of a collimated electromagnetic light source exist in the literature. This is due to the fact that laser beams usually have intensity distributions as the one shown above rather than having a sharp, squared profile. The two most used definitions are the *Full width at half maximum* (FWHM), and the 1/e^2 width.

The FWHM width corresponds to the distance between two points of a Gaussian distribution where the intensity equals to ½ or 50% of the intensity at its peak. The 1/e^2 width follows the same principle of the FWHM width, but in this case the intensity at which the distance is measured equals 1/e^2 or 0.135 times the maximum intensity of the distribution.

After calculating and plotting the average Gaussian beam profiles that intersect the maximum value (shown as solid black lines in Figures E.3(a) and (b)), the values of the FWHM and $1/e^2$ diameters can be obtained for both the horizontal and vertical directions:

Table E.1: Calculated values of the laser beam diameter

Diameter definition	**Diameter in Horizontal direction [mm]**	**Diameter in Vertical direction [mm]**
FWHM	2.532	2.620
$1/e^2$	3.802	4.176